Integrated Optoelectronics Applications in Fiber Optic Receiver Packaging

by

J. Shawn Addington

Dissertation submitted to the Faculty of the
Virginia Polytechnic Institute and State University
in partial fulfillment of the requirements for the degree of

DOCTOR OF PHILOSOPHY
IN
ELECTRICAL ENGINEERING

APPROVED:

Aicha Elshabini-Riad
A. Elshabini-Riad, Chair

A. Safaai-Jazi

I. Jacobs

K. A. Murphy

W. E. Kohler

September 1995
Blacksburg, Virginia

Key words: optoelectronics, fiber optics, receiver, integration, waveguide, packaging

INTEGRATED OPTOELECTRONICS APPLICATIONS IN FIBER OPTIC RECEIVER PACKAGING

by

J. Shawn Addington

A. Elshabini-Riad, Chair

Bradley Department of Electrical Engineering

(ABSTRACT)

The objective of this research is the development and evaluation of a new style of integrated optoelectronics. The approach combines the selectivity of traditional hybrid integration with the "internal" interconnection capabilities of monolithic integration, through the use of low temperature cofireable ceramic (LTCC) tape systems. This new integration technique is applied to a fiber optic receiver system, and focuses on three main tasks. The first task involves the realization, and eventual hybridization, of the receiver electronics, including the photodetector and the associated amplifier circuitry. Second, materials and techniques for the processing of planar optical waveguides are investigated, in order to expand the potential applications of the technique. Finally, a new technique of integrating an optical fiber with the above components is introduced and evaluated.

Multichip module (MCM) technology has become the new standard in the field of electronic packaging. Much of the success of MCM packaging may be attributed to the development of LTCC systems. LTCC materials utilize their multilayer (3-dimensional) nature to achieve a higher level of electronic circuit density within a hermetic module. The goal of this research effort is to expand this capability to include optical components, in addition to the traditional electronics. The optical counterpart to the printed electrical wiring within an LTCC package is the planar waveguide. Much of this research is

therefore devoted to an investigation of materials and processing techniques used to develop planar optical waveguide structures. This research discusses the production and evaluation of both thin film and thick film structures based on germanium oxide (GeO_2) - a material with promising photosensitivity characteristics. As has been seen with optical fibers, the optimization of planar optical waveguides is also not a trivial task. Aside from the material and processing concerns, there is also the compatibility with cofireable ceramic materials that must be addressed.

Once these planar optical waveguides are able to be incorporated within the internal layers of the multichip module, there must be a means of accessing them from the outside of the package. Thus this research work also investigates the ability to integrate optical fibers within LTCC materials. Traditional optical fiber connectors are not suitable for this application, since the interface between fiber and waveguide will be inside a hermetic module. This research discusses the techniques used to achieve this novel integration capability. The planar optical waveguides developed in this work are not yet optimized for full integration within cofireable ceramic materials. Thus, the interface between fiber and waveguide is theoretically analyzed from the perspective of coupling efficiency. Nevertheless, the ability to integrate an optical fiber within an LTCC module is demonstrated through the development of a fiber optic receiver module. One of the benefits of the integration technique proposed in this research work is selectivity. This feature is demonstrated through the evaluation and selection of individual components of the receiver system. This work demonstrates that the selection of receiver components is not dictated by the integration technology, but is determined instead by individual performance characteristics.

Through the hybridization of the receiver circuitry and the successful integration of an optical fiber within the LTCC material, a functional integrated fiber optic receiver module has been completed. In addition, this research into the development of both thick and thin film planar optical waveguide materials is an important step toward the eventual integration of these devices.

Acknowledgements

This section is dedicated to all of the individuals who have assisted me in the completion of this dissertation. First, I would like to thank my committee members, Dr. K.A. Murphy, Dr. A. Safaai-Jazi, Dr. I. Jacobs, and Dr. W.E. Kohler for their constructive input and suggestions. I would also like to express my gratitude to Loretta Estes for all of her help. I would like to recognize the efforts of Bryan Dickerson, Tze-Chiun Chen, and Shatil Haque for their assistance with the ellipsometry and spectrophotometry measurements. I would also like to thank Jason Zeakes and the members of FEORC who contributed their time and facilities to assist me in the waveguide attenuation measurements. In addition, I would like to thank the many members of the Microelectronics and Time Domain Laboratories who have supported me with their thoughtful advice and assistance. I would like to thank my wife Adele for her caring companionship during my undergraduate and graduate work at Virginia Tech. Finally, special thanks go to my parents, Ronald J. and Betty R. Addington, for their loving support and encouragement throughout my education.

Table of Contents

List of Figures

List of Tables

Chapter 1
Introduction

The objective of this research is the development and evaluation of a new style of integrated optoelectronics. This approach combines the benefits of two well-established integration techniques while eliminating their individual disadvantages. The "hybrid" approach to optoelectronic integration allows each of the system components to be selected independently in order to maximize their individual performance. However, the need for external interconnections degrades the overall performance of the hybrid integration. The "monolithic" approach, on the other hand, eliminates the need for external interconnections. However, a compromise must be reached on the selection of the "base" material, as it will benefit some of the components more than others. This new integration technique will utilize low temperature cofireable ceramic (LTCC) materials in order to combine the selectivity of hybrid integration with the "internal" interconnection capabilities of monolithic integration.

The growing popularity of multichip module (MCM) technology has spurred an increased interest in the use of low temperature cofireable ceramics as potential electronic packaging materials. One of the reasons for this trend is the ability of LTCC materials to create modules in which all of the electrical interconnections are contained inside a three-dimensional ceramic package. Some additional advantages of LTCC materials are listed below:

- low dielectric constant (~ 7) and loss tangent (< 0.1) allow their use in high frequency applications
- fine line definition (on the order of 5 mil line width and spacing) allows for greater circuit density
- low temperature processing (850° C) allows the use of high conductivity

(precious) metals

- one-step firing profile and compatibility with well-established thick film processing techniques simplify adaptation to the technology and improve cost/performance features
- capacity to integrate passive components and interconnections internally allows for reduction in package size
- low coefficient of thermal expansion (CTE) (~ 3 x 10^{-6} / °C) reduces thermal strains on integrated chips (Si CTE ~ 3.35 x 10^{-6} / °C)
- inherent hermeticity extends their application to more harsh environments
- unlimited number of layers allows for a high package density

HTCC systems possess many of these same characteristics, however the higher processing temperature (1400 °C - 1600 °C) restricts them to the use of lower conductivity refractory metals.

The fiber optics community has also capitalized on the use of LTCC materials to package its electronic circuitry. However, the optical fiber has always been treated as an external component of the package, thus requiring additional connector structures and processing steps. The goal of this research is to develop a fiber optic receiver system in which both the electronic circuitry and the optical fiber are integrated within an LTCC package. To fully appreciate the importance of this achievement, one must understand the structure of MCMs that use LTCC technology (MCM-C, where the C refers to ceramic materials). MCM-C technology uses the multilayer nature of cofireable ceramic materials to create more compact packages. As mentioned earlier, the electrical "wiring", as well as most passive components, are confined within the thickness of the package. This reduces the dimensions of the package, as the top and bottom surface areas of the package must only be large enough to attach chips that cannot currently be integrated within the LTCC material. To further reduce the size of the package, these surface chips are often depressed into the package through the use of cavity structures. An encapsulant or cap

structure is often used to cover these surface components to maintain the hermeticity of the module. For fiber optic applications, one can see that the traditional fiber optic connectors are not suitable for MCM-C technology if one wishes to take full advantage of the size-reduction and hermetic capabilities of LTCC systems. For example, a fiber optic detector chip may be placed on the surface of an MCM-C receiver module, possibly within a cavity. The difficulty becomes how to interface an optical fiber to the detector chip without destroying the inherent self-containment features of the technology. Simple placement of a traditional fiber optic connector structure on the surface of the MCM-C module significantly increases the thickness of the overall package, and/or occupies surface area that may otherwise be used by electronic chips. Again, consider the MCM-C module, containing a detector chip within a cavity structure. The ideal situation is to interface the optical fiber with the detector internally, without the need to add external connector structures to the module. This technique, therefore, requires that the optical fiber be integrated between layers of the LTCC packaging material.

This integration technique may eventually be applied to the packaging of planar optical waveguide structures. Consider, for example, a fiber optic receiver that uses planar optical waveguides for demultiplexing purposes. These waveguide structures may be realized on LTCC material, and then integrated as an internal layer within the same MCM-C module that contains the receiver electronics. An incoming fiber couples with the planar waveguide structure on an internal layer of the module. Output fibers, containing the demultiplexed signals, exit the package and then reenter at a different level to couple to the detector chips within a surface cavity.

This research work will focus on three primary areas. First, the receiver, including the photodetector and its associated amplifier circuitry, will be investigated. Second, various materials and techniques for the processing of planar optical waveguides will be evaluated. Research into these devices will be important in developing future applications of this integration technique. Finally, the integration of the optical fiber within the LTCC

material is investigated, including the coupling of the fiber to electronic circuitry and planar optical waveguides.

This research is successful in demonstrating the use of a low temperature cofireable ceramic as an optoelectronic packaging material. The ability to integrate an optical fiber within the material, and interface it with a hybridized optical receiver circuit is illustrated. Research into the development and processing of planar optical waveguides enhances the integration capabilities of this technique.

The dissertation is organized into six chapters and an Appendix. Chapter 1 is a general introduction to the dissertation. Chapter 2 provides an overview of published work related to the three main areas of this research - the phototransistor, the planar optical waveguide, and optoelectronic integration techniques. Section 2.2 addresses concerns related to the selection of the photodetector used in this work. Material aspects and performance characteristics often determine the selection of one photodetector, in this case the phototransistor, over another. Section 2.3 discusses various materials and techniques used in the formation of planar optical waveguides. The attractive characteristics of germanium oxide (GeO_2) provide the opportunity for further research into alternative processing techniques. Finally, Section 2.4 reviews techniques used in the integration of optical and electronic components. An alternative optoelectronic integration technique is proposed in this work.

Chapter 3 discusses the fiber optic receiver. This chapter identifies the role of the receiver, and focuses on its two primary components - the photodetector and the amplifier. The purpose of each of these components is discussed, along with their various configurations, and general requirements for their use in a fiber optic communications system. A detailed discussion of the role of noise in a receiver system is also provided, including an analysis of the signal-to-noise ratio (SNR) for the receiver used in this work. Finally, the hybridization process is implemented, and experimental results are presented for breadboard, hybrid, and computer simulated versions of the receiver circuit.

Chapter 4 investigates the planar optical waveguide. This chapter discusses the operation, design, and analysis of planar waveguides, including some general performance requirements. However, the focus of Chapter 4 is on the materials and techniques used to process these waveguide structures. Experimental results are presented for the variety of materials and processing techniques investigated during the course of this study. In addition, two techniques for the fabrication of thick film planar optical waveguide structures are discussed and compared.

Chapter 5 discusses the integration of the electrical and optical components of the fiber optic receiver within a single LTCC package. The concept of coupling efficiency is addressed in detail. Experimental results are presented for several types of integration, including the development and evaluation of a complete integrated fiber optic receiver module. The incorporation of thick film planar optical waveguides with this integration technique is discussed. An analysis of the coupling between an optical fiber and a rectangular waveguide is presented in the Appendix.

Chapter 6 provides a general conclusion of the research, as well as some proposed future work.

Chapter 2
Literature Review

2.1 Introduction

The purpose of this chapter is to highlight other studies related to integrated optoelectronic applications in fiber optic receiver packaging. An integrated fiber optic receiver consists of several primary components. First, the incoming light signal must be detected and converted to an electrical signal. This is the role of the photodetector device. Depending on the complexity of the receiver, planar optical waveguides may be incorporated within the device to perform active and/or passive roles. For example, the planar optical waveguide may be used in switching or filtering operations, or it may simply assist in the coupling of the optical fiber to the electronic circuitry. Finally, the optical and electrical components are integrated within a single package to achieve better performance characteristics. Chapter 2 will therefore be divided into three main sections. Section 2.2 will cover the photodetector portion of the study, focusing on the phototransistor device. Section 2.3 will review some recent advances in the fabrication of planar optical waveguides, and Section 2.4 will discuss some of the techniques that have been used to integrate optical and electrical components.

2.2 Phototransistors

This section is dedicated to the photodetector portion of the receiver circuit. Most of the attention, however, will be directed toward the phototransistor, as this is the device that will ultimately be used in this research effort.

As the field of fiber optic communications has changed (to higher wavelengths, higher transmission rates), photodetector technology has changed accordingly. In the early days of 0.85 um transmission at relatively low speeds, Si (silicon) avalanche photodiodes (APDs) were sufficient photodetectors. As optical fiber technology matured, low-loss properties were identified at 1.3 um and 1.55 um wavelengths. However, due to

its relatively large energy band gap characteristic, Si is not "responsive" to these higher incident wavelengths. As discussed, analytically, in Chapter 3, the responsivity or quantum efficiency of a photodetector material is a measure of how well the incident optical energy is transformed to an electrical signal. Figure 2.1 illustrates this characteristic for three types of photodetector materials. Note the ineffectiveness of Si, and the better performance of Ge (germanium) and the III-V compound InGaAs (indium gallium arsenide), at these higher wavelengths of operation.

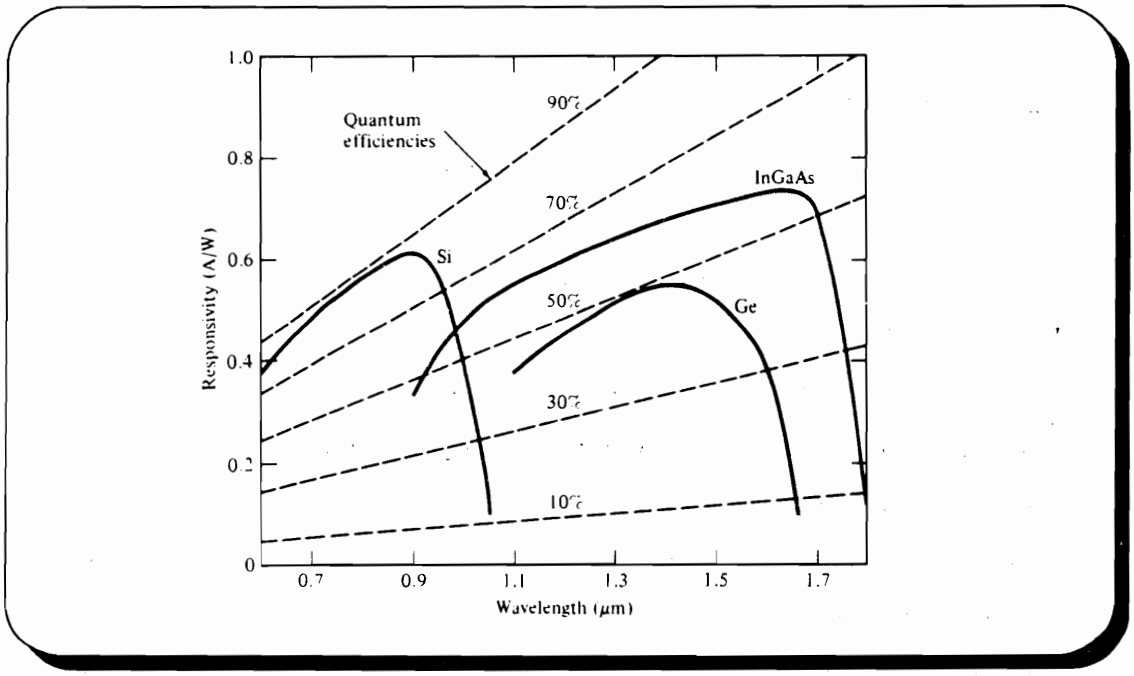

Figure 2.1 - Responsivity of Si, Ge, and InGaAs vs wavelength[1]

Ge and InGaAs were first limited to use in pin photodiodes, due to their poor performance characteristics in APD configuration. However, after additional research into more complicated designs (such as reach-through and heterojunction structures), these materials ultimately became used in high performance APDs, exhibiting high speeds and low noise characteristics. As an alternative to the gain mechanism provided by the APD, phototransistors were also considered as possible photodetectors. Early devices of this type, however, suffered from a trade-off between gain and response speed.[2]

Both new materials and new structures have been investigated in an attempt to find the optimum combination of response speed and gain. A group of researchers, for example, has been studying the use of amorphous Si-Ge thin film materials in a photodetector array.[3] This material offers a range of possible band gap energies, and is expected to produce detectors that may operate up to 10 MHz. In addition, the use of Si at 1.3 um (above its theoretical limit of ~ 1.1 um) has been realized in an avalanche photodiode by utilizing the band-gap narrowing (BGN) phenomenon resulting from high doping.[4] Another interesting new device is the 50 GHz InGaAs multimode waveguide photodetector (WGPD) that is side-illuminated. This feature provides better coupling efficiency to fibers, and allows the quantum efficiency and the bandwidth of the device to be considered separately, since the light and the photocarriers travel in different directions.[5]

However, as mentioned above, this section will be dedicated mainly to phototransistors. A phototransistor differs from a regular bipolar transistor in that the reverse biased collector-base junction is used as an "active" region, where light is absorbed. Photogenerated carriers created in this region are separated by the high electric field, and then traverse through the device in the same manner as in a regular bipolar junction transistor. These carriers constitute a photocurrent which undergoes the inherent current gain mechanism of the transistor. Thus, like the APD, the phototransistor provides some built-in amplification of the generated photocurrent. Since phototransistors possess this inherent internal gain mechanism, much of the recent work has focused on expanding the bandwidth of these devices, without compromising their gain.

Some early research investigates the use of a wide band gap emitter as part of a heterojunction structure.[6] This design has several advantages. First, it prevents the absorption of light in the emitter region. Second, it allows the base to be doped heavily compared to the emitter without degrading the injection efficiency. This results in a low base resistance (in addition to the low base-emitter depletion capacitance), and prevents modulation of the narrow base region required for high gain. A common collector

configuration with floating base is used in the analysis of this design. For small signal levels, the gain-bandwidth product is proportional to the average optical power, and variation of the base width has a negligible effect on the bandwidth. An external base bias may be used to limit this dependence on the power level. For large signal levels, a wider base region results in a higher bandwidth, but produces a lower gain. Unlike the avalanche photodiode (APD), no additional noise is introduced in the gain mechanism. Later work investigates the use of the base bias discussed above to create a high speed device.[7] By applying the proper bias, slow photocurrent components can be made to cancel themselves out. The work also addresses the sensitivity characteristics of a typical InP/InGaAs heterojunction phototransistor (HPT) device (Figure 2.2). Sensitivity is a term that is associated with the performance of digital receiver systems. A higher sensitivity indicates that a receiver may operate at a specified performance level with less incident optical power. For example, a phototransistor receiver is expected to exhibit a higher sensitivity than a pin receiver, due to the internal gain feature of the phototransistor.

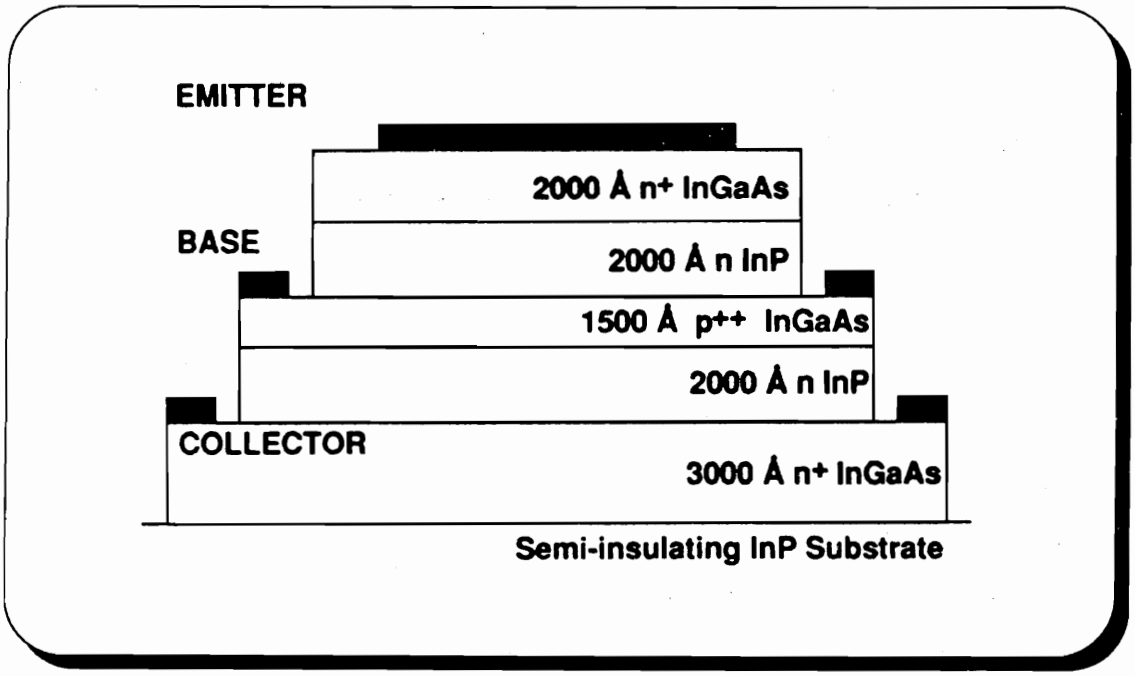

Figure 2.2 - InP/InGaAs heterojunction phototransistor[7]

Receiver sensitivity is a function of the desired bit-error rate (BER), bandwidth, responsivity, and noise characteristics. For the device shown in Figure 2.2, the InP emitter allows a higher sensitivity at the shorter wavelengths. The top InGaAs (electrical contact) layer may also be altered or removed to improve the sensitivity at shorter wavelengths. Sensitivity at longer wavelengths may be enhanced by increasing the base thickness. Note that this device utilizes a vertical structure in order to reduce carrier transit distances, and therefore increase response speed.

HPT research has recently progressed to the point where the bandwidth and sensitivity of monolithic HPT devices are comparable to that of the traditional monolithic pin/HBT combination.[8] In addition, other configurations have been investigated in an attempt to improve the performance of HPT devices.[9] The simple common emitter configuration suffers from poor bandwidth due to the large collector-base capacitance. The cascode (common emitter/common base) configuration extends the bandwidth of the device. However, a new design incorporating a cascode configuration, with reduced emitter areas, followed by a two-step emitter follower has demonstrated notable performance. The reduced emitter area characteristic lowers the base current and the associated input shot noise. Also, the reduction in capacitance allows a larger transimpedance to be utilized, thus improving the sensitivity without sacrificing bandwidth. Although thermal noise is also reduced by the higher transimpedance, the base shot noise remains as the primary factor in determining the sensitivity of the device.

2.3 Planar Optical Waveguides

The advancement of fiber optic communications has also created the need for high performance planar optical waveguides. Like the optical fiber, the planar optical waveguide has progressed from a simple, relatively high-loss, and primarily passive device, to a complicated, low-loss, and often active device within the optoelectronic package. In addition, the planar version of the optical fiber also uses the concept of total internal reflection (Chapter 4) to propagate the light. As discussed in Chapter 4, there exists a

variety of materials and techniques used in the fabrication of planar optical waveguides. This section will expand upon the processing of some recent waveguide structures.

One of the techniques that has gained attention in the formation of inorganic waveguides is chemical vapor deposition. One fabrication procedure, proposed by Swiss researchers in 1992,[10] uses plasma enhanced chemical vapor deposition (PECVD) to create a low loss silica waveguide on silicon. In chemical vapor deposition, the deposited film forms as a result of chemical reactions among gaseous components. The resulting waveguides possess propagation losses less than 0.1 dB/cm (after high temperature annealing), and refractive indices that can be varied by 5 x 10^{-3} to 0.5. Such a range allows the waveguides to match well with optical fibers (small index contrast ~ 5 x 10^{-3}) and semiconductor devices (large index contrast ~ 0.5). However, the use of silane makes this a hazardous technique.

Another use of chemical vapor deposition is in the formation of phosphorus-doped silica waveguides in silicon V-grooves.[11] The phosphorus-doped silica demonstrates less tensile stress and no defects, compared to pure silica. In addition, formation of the guide within the V-groove allows for quality alignment to optical fibers. Losses on the order of 0.1 dB/cm are reported at 633 nm.

Due to the photosensitive nature of some inorganics such as GeO_2,[12,13] refractive index gratings can be optically induced in the waveguide for filtering applications. The formation of gratings in an ion-exchanged glass waveguide, on the other hand, is a much more involved process that has only recently been developed.[14]

Polymer waveguide processing has also been an active area of research in recent years. One technique involves etching a groove in a substrate, and then back-filling the groove with a high index polymer to form the waveguide. Waveguides with losses of a few 0.1 dB/cm at 830 nm, 850 nm, and 1300 nm have been achieved.[15]

Another technique begins with a mixture of PMMA (polymethyl methacrylate) and a photoinitiator deposited on a substrate. The film is exposed to UV light through a mask. A photochemical reaction takes place in the exposed regions which increases the refractive

index in those regions. During annealment, this increase in refractive index is fixed, and the non-reacted photoinitiator in the unexposed regions (under the mask) evaporates out, leaving behind the PMMA and a lower refractive index in the unexposed regions. Since some material is lost in the unexposed regions, the exposed (waveguide) regions will be slightly higher than the surrounding regions. Refractive index changes between 0 and 3% are possible with this technique.[16] Such waveguides have been created with losses around 0.2 dB/cm at 633 nm.[15]

Another technique that has been studied recently is laser writing of acrylate polymer waveguides.[17] In this process, a mixture of monomers and photoinitiators is deposited on a substrate. This layer is photocrosslinked (monomers to polymers) through exposure to UV light. A second layer of monomers having a higher refractive index than the first layer is deposited. This layer is selectively exposed to UV light to form photocrosslinked waveguides. The unexposed material is removed with acetone. A top layer, having the same composition as the bottom layer, is deposited over the waveguides and exposed to UV light. This type of structure exhibits propagation losses of 0.01 dB/cm at 670 nm, and high thermal stability (0.6 hours at 250° C to increase loss to 1 dB/cm).

As mentioned in Chapter 4, lithium niobate ($LiNbO_3$) has been the most widely studied crystal used in the formation of planar optical waveguides. The two primary techniques used in fabricating waveguides in $LiNbO_3$ (titanium diffusion and proton exchange) are described below.

The titanium diffusion process begins with a clean, polished crystal upon which photoresist is deposited. The crystal is covered by a mask and exposed to UV light. After developing, a window corresponding to the waveguide pattern remains in the photoresist. Titanium is deposited on the crystal by sputtering or evaporation. The crystal is placed in a solvent to remove the remaining photoresist and unwanted titanium before undergoing the diffusion process. An alternative to this "lift-off" technique is the application of titanium over the entire surface, followed by selective removal of titanium outside of the desired waveguide regions. As has been seen for earlier diffusion processes, parameters

such as waveguide width and depth and index change are controlled by the fabrication procedure. The proton exchange technique is also quite simple. A metallic mask, with openings to define the waveguide, is placed on a clean $LiNbO_3$ substrate. The substrate is placed in a melt of boiling benzoic acid (200 - 249° C). The resulting waveguide is step-like, and exhibits a high index change as well as losses ~ 0.5 dB/cm in the visible range. However, the electrooptic efficiency of the waveguide is 2.7 times less than in Ti-diffused waveguides.[18] This problem is overcome, however, by using a benzoic acid diluted with lithium benzoate. For applications where a small index change is desired (i.e. waveguide to fiber coupling), a post-processing annealing results in a reduced index change and a more graded profile.

Semiconductor optical waveguides have been widely used in the monolithic production of integrated optoelectronic devices. Quaternary III-V compounds such as $Ga_xIn_{1-x}As_yP_{1-y}$ provide a great amount of flexibility in designing for a particular wavelength, while maintaining good lattice match with cladding compounds such as InP and InGaAs.[19] III-V compounds such as these are important in fiber optic applications in the 1.3 - 1.55 um range.

In recent years, the traditional thick film technology has also been implemented in the production of optical waveguides. This well-established technology offers a low-cost alternative to the procedures mentioned above. However, due to their larger size and relatively high losses, thick film optical waveguides have so far been limited to primarily passive multimode applications. Researchers have investigated a variety of dielectric and glassy materials to determine their indices of refraction. From these materials, waveguide structures are then produced to evaluate attenuation characteristics.[20] Post-processing techniques such as re-melting and laser machining have also been studied as means of improving optical performance and enhancing fiber to waveguide coupling.[21]

2.4 Optoelectronic Integration Techniques

This section covers some of the other techniques used to integrate optical and electronic components within an optoelectronic device. Low temperature cofireable ceramic (LTCC) materials have been used in the packaging of optoelectronic circuits, due primarily to the reduction in size that is possible with these materials. Examples of this utilization are shown by Shimada, et al[22] and Tanaka, et al[23]. These studies, however, require external connectors to interface the electronics with the optical fiber. Patents, such as the one obtained by Pavlath,[24] illustrate various mechanical structures that have been developed to couple an optical fiber to an optoelectronics chip.

Coupling from an optical fiber to a planar waveguide has also attracted the attention of researchers. Examples of this integration range from the simple butt-coupling of tapered waveguides with optical fibers[25] to the patented use of fine glass particles to physically fuse the fiber to the waveguide.[26]

2.5 Conclusions

This chapter has reviewed literature relevant to this research endeavor. Each of the three main areas of this project, the receiver, the planar optical waveguide, and the integration of electrical and optical components, has been considered in the review.

Chapter 2 has provided the foundation for this research work. Section 2.2 supports the selection of the phototransistor as the photodetector used in this study. For purposes of the integration techniques discussed in Chapter 5, the photodetector must operate at 840 nm, be side-illuminated, and be compatible with traditional microelectronic processing techniques. As long as these criteria are satisfied, any type of photodetector will suffice for this work. However, since one of the goals of this research is to develop a competitive optoelectronic package, high performance is a necessity. Thus, the phototransistor is the preferred device. Section 2.3 illustrates the variety of materials and techniques used in the formation of planar optical waveguides, as well as the opportunities for improvement. Again, for the proposed integration technique to be successful, there

must be room for flexibility. The photosensitive characteristic of germanium oxide (GeO_2) provides a wide array of potential applications. In addition, the processing must be compatible with the materials used in the integration technique. Although some thin film structures will be fabricated and evaluated, thick film planar optical waveguides may be more compatible with the proposed packaging technology. Section 2.4 outlines other techniques developed for the integration of optical and electronic components. Due to the increasing popularity of multichip module (MCM) technologies, maximum utilization of materials such as low temperature cofireable ceramics (LTCC) is of great importance. This research intends to take the use of LTCC materials, as optoelectronic packaging materials, to a level above what is described in Section 2.4.

Chapter 3 will discuss the first main area of this research - the fiber optic receiver. This chapter focuses on the selection of primary receiver components, based on their performance characteristics. The construction and evaluation of a hybridized fiber optic receiver module are also presented.

Chapter 3

Fiber Optic Receiver

3.1 Introduction

The primary objective of any fiber optic receiver is to convert optical signals into electrical signals, and amplify them for use in future processing. The two main components of the receiver system are the photodetector and the amplifier circuitry (Figure 3.1).

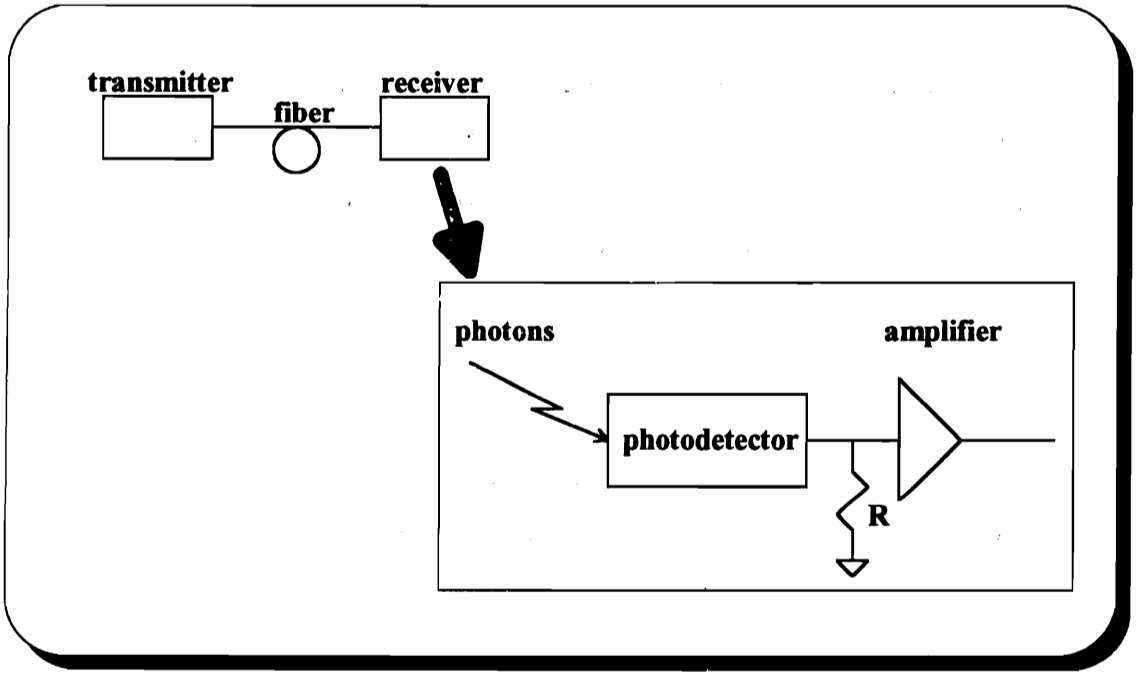

Figure 3.1 - Fiber optic receiver system[1]

The role of the photodetector is to convert the incoming optical energy into electrical energy. As discussed in this chapter, the type of photodetector (i.e. material composition and configuration) used in the receiver system is highly dependent on the characteristics of the incoming optical, as well as the desired level of receiver

performance. The electrical output signal from the photodetector, however, is typically too small for use in subsequent electronic applications. Thus an amplifier stage is implemented before any additional processing of the electrical signal takes place. Again, this chapter reveals how proper selection of the amplifier circuitry is crucial to the performance of the overall receiver system. The quality of a fiber optic receiver system is often measured in terms of the amount of noise it produces. The significance of the noise level relative to the signal level is discussed in this chapter. Chapter 3 will therefore review these three important topics - receiver noise, photodetectors, and amplifiers - as they relate to fiber optic communication systems. As discussed in Chapter 1, this proposed style of integrated optoelectronics will take advantage of the selectivity provided by traditional hybrid microelectronic techniques. This selectivity is applied to the components of the fiber optic receiver system. An evaluation of the above three topics is essential to the proper selection of receiver components in order to maximize the performance of the overall system. A fiber optic receiver circuit will then be developed, tested, and ultimately hybridized for use in the integration process of Chapter 5.

3.2 Background

3.2.1 Noise

Noise sets the fundamental lower limit on the signal level that may be processed by the receiver, and each component of the receiver system contributes to the noise. Some of the common noise types include quantum (shot) noise, thermal noise, surface leakage current noise, and avalanche multiplication noise. Quantum, or shot, noise originates from the statistical nature of the photodetection process. Both the arrival, as well as the detection of photons are random processes that have been modeled as Poisson functions and Gaussian approximations.[27] This introduction of uncertainties into the system constitutes a type of noise. Other types of quantum noise include background current noise and bulk dark current noise. Background current noise is due to light, external to the signal, striking the photodetector and creating an unwanted current. Bulk dark current

noise is caused by the thermal, rather than optical, excitation of mobile carriers (electrons and holes) within the semiconductor material of the photodetector. Thermal (or Johnson) noise is created within the system in the resistance associated with the photodetector bias and the amplifier. Surface leakage current noise is created by surface characteristics (such as defects and impurities) of the photodetector material. Finally, avalanche multiplication noise appears in the system if avalanche photodiodes (APDs) are used, due to the statistical nature of the multiplication process within avalanche photodiodes. These noise sources are often expressed in terms of mean square currents:[1]

Quantum (Shot) Noise: $$< i_s^2 >= 2q(I_P + I_B + I_D)B \quad (3.1)$$

Thermal Noise: $$< i_t^2 >= \frac{4kTB}{R} \quad (3.2)$$

Surface Leakage Current Noise: $$< i_L^2 >= 2qI_LB \quad (3.3)$$

Avalanche Multiplication Noise: $$< i_s^2 > \rightarrow < i_s^2 > M^2F(M) \quad (3.4)$$

$$F(M) \approx M^x; 0 \leq x \leq 1 \quad (3.5)$$

where: q = electric charge; I_P = primary photocurrent; I_B = background current; I_D = bulk dark current; B = bandwidth; k = Boltzmann's constant; T = temperature; M = multiplication gain of the APD

These equations may then be used to define the signal-to-noise ratio (SNR) for the receiver:

Signal: $$< i_P^2 >= \frac{1}{2}I_P^2M^2 \quad (3.6)$$

Noise: $$< i_N^2 >=< i_s^2 > +< i_t^2 > +< i_L^2 >$$ (3.7)

SNR: $$\frac{<i_P^2>}{<i_N^2>}$$ (3.8)

3.2.2 Photodetectors

The term photodetector refers to any semiconductor device that detects optical signals through electronic processes.[28] The mechanism of a general photodetector may be summarized in the following three processes:

1. carrier generation by incident light
2. carrier transport and/or multiplication
3. interaction of the resulting current with the external circuit to provide the output signal

Depending on the type of application, the photodetector must also meet certain performance requirements. For example, in fiber optic communications, the photodetector must satisfy three requirements:

1. low noise characteristics
- A photodetector that exhibits a high degree of noise will make the process of recovering the desired signal more difficult. Higher transmission powers and shorter transmission links (to reduce signal attenuation) are therefore necessary to overcome the additional noise caused by the photodetector.

2. high quantum efficiency (responsivity) at the operating wavelength
- Photodetector materials do not detect optical energy of all wavelengths with equal efficiency. Thus, it is important to match the operating wavelength with the photodetector material that behaves best at that wavelength.

3. fast response speed

- For high speed fiber optic communication applications, the photodetector must be able to respond to the rapid changes in the incoming optical signal. Photodetectors with a slow response speed (relative to the frequency of the incoming optical signal) will not be able to accurately reproduce the optical signal in electrical form.

Photodetectors exist in a wide variety of configurations. They range from the simple slab photoconductors, to complex phototransistor designs. Despite the difference in structure, photodetectors are all derived from the same material - semiconductors. The operating conditions of the photodetector determine the type of semiconductor material used in the fabrication, as well as the optimum configuration.

Selection of the appropriate semiconductor material is determined by the operating wavelength of interest. All semiconductor materials exhibit an energy band gap structure, in which a region of "forbidden" energy levels separates the "stable" (valence band) energy levels of an electron from the "excited" (conduction band) energy levels. Energy given to the semiconductor by the incident light may excite an electron from the valence band to the conduction band if that energy is greater than the energy band gap. These excited electrons (and the "holes" they leave behind in the valence band), in turn, contribute to an electrical current flow that is representative of the incident light. Thus, the energy band gap of a semiconductor material limits the wavelength range of light that may be detected by the device by the following relationship:

$$E_{ph} = \left(\frac{hc}{\lambda}\right) > E_g \qquad (3.9)$$

where: E_{ph} = incident photon (light) energy

E_g = energy band gap

h = Planck's constant

c = speed of light

λ = wavelength of light

The simplest example of a photodetector is called a photoconductor. The photoconductor is a slab of semiconductor material with metal contacts at both ends. However, in order to increase the number of electron-hole pairs available for creating the photocurrent, the photodiode is often implemented instead. A photodiode is a p-n junction formed from the bulk semiconductor by forcing one side of the semiconductor to have an excess of electrons (n-side), and forcing the other side to have an excess of holes (p-side). These excess concentrations are created by "doping" both sides of the semiconductor with small amounts of appropriate impurities. The region of the semiconductor near the junction is called the depletion (or space-charge) region, as some of the excess electrons on the n-side "recombine" with some of the excess holes on the p-side. The basic operation of the photodiode is as follows. A reverse bias (positive voltage on the n-side) is applied to the p-n junction. This widens the depletion region and strengthens the electric field which exists across this region. Light impinging on the depletion region creates electron-hole pairs that are rapidly separated by the strong electric field, thus minimizing their chances of recombining, and a photocurrent is created. As mentioned above, it is important to maximize the quantum efficiency (responsivity), and minimize the response time. Quantum efficiency is defined as follows:[1]

$$\eta = \text{quantum efficiency} = \frac{I_p/q}{P_{opt}/h\nu} = \frac{\#\text{ electron-hole pairs}}{\#\text{ incident photons}} \qquad (3.10)$$

where: I_p = photocurrent (electric current produced by the incident light)

q = electric charge

P_{opt} = incident optical power

h = Planck's constant

ν = frequency of the incident light

Quantum efficiency is also expressed in terms of the responsivity of the photodetector:

$\mathcal{R}$ = responsivity = $\frac{\eta q}{h\nu}$ (3.11)

Such that: $I_p = \mathcal{R}P_{opt}$ (3.12)

The response speed of a photodiode is determined by three main factors:[1]

1. transit time of the photocarriers (electron-hole pairs) in the depletion region (Equation 3.13)

$$t_d = \frac{w}{v_d} \quad (3.13)$$

where: w = width of depletion region

v_d = carrier drift velocity

2. diffusion time of the photocarriers generated outside the depletion region (Figure 3.2)

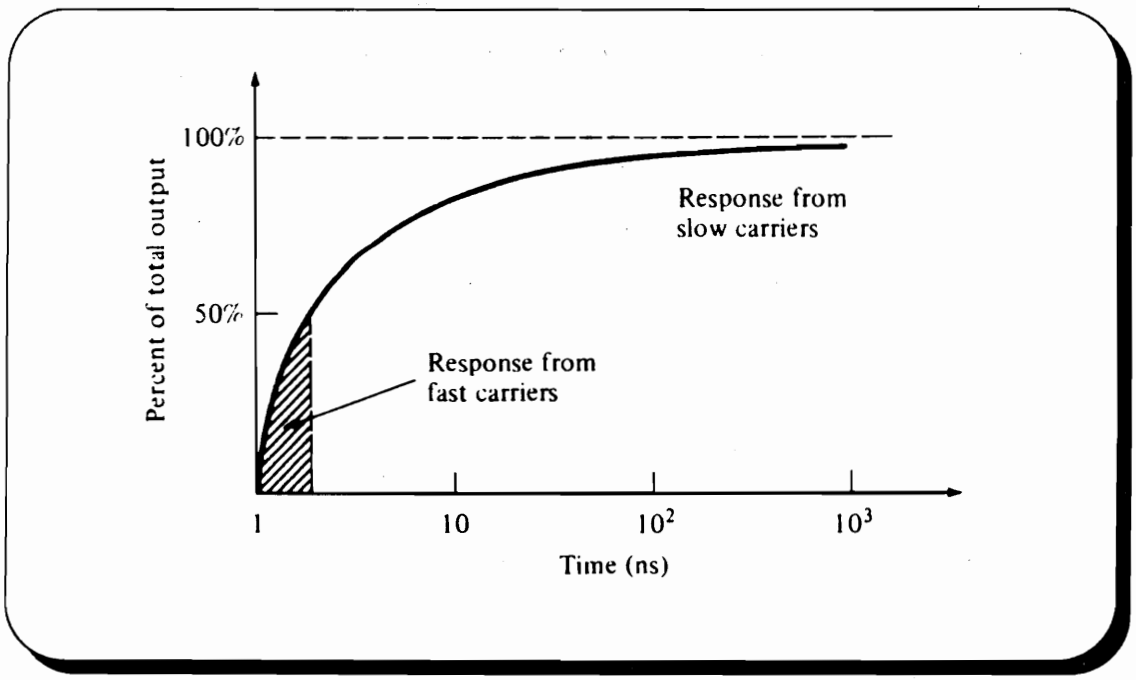

Figure 3.2 - Slow carrier response[1]

3. RC time constant of the photodetector and associated circuitry (Equation 3.14)

$$C_j = \frac{\varepsilon A}{w} \qquad (3.14)$$

where: ε = permittivity of the depletion region

A = cross-sectional area of the depletion region

w = width of the depletion region

Clearly, then, an increase in the depletion region width would increase the quantum efficiency by allowing more of the impinging light to be absorbed. This is the concept behind the most common photodiode - the pin photodiode. The "i" in pin represents a middle layer of "intrinsic" (undoped) semiconductor material between the p- and n-sides of the junction that acts in the same manner as the original depletion region (no excess electrons or holes). For a fast-response (high frequency) device, the RC time constant must be kept low. A larger depletion width reduces the junction capacitance of the photodiode (Equation 3.14). However, the thicker the depletion layer, the longer it takes for the generated electron-hole pairs to drift across the region in the presence of the electric field. This decreases the response speed of the photodiode. Therefore, a trade-off must be made between quantum efficiency and response speed.

Both p-n and pin structures have no internal gain mechanism (G=1). The bandwidth of a p-n diode is essentially determined by a combination of two factors - RC time constant and diffusion/drift time. The use of an intrinsic region in a pin diode decreases the RC time constant, and makes the diffusion/drift component the dominant factor. Attempts to use thin layers in order to reduce the diffusion/drift time often result in incomplete absorption and a lower gain (G<1). A Schottky diode is basically a one-sided p-n diode. This has its advantages and disadvantages as a photodetector. Again, the device exhibits no gain (G=1), and the quantum efficiency of the device is reduced due to the thinner absorption volume. On the other hand, the response time is shorter, resulting in a higher bandwidth.[29] Photoconductors, by comparison, exhibit a

trade-off between gain and bandwidth. Photoconductors can produce a significant gain that is proportional to the minority carrier lifetime. The bandwidth of the device, however, is inversely proportional to the minority carrier lifetime. Thus, an n-type material will exhibit a higher gain (and lower bandwidth) than a p-type material due to the lower mobility (longer lifetime) of holes compared to electrons.[29]

The question arises as to what happens if the reverse bias voltage is increased. Under such a condition, the electric field in the depletion region becomes extremely strong. Thus, when the electron-hole pairs are separated, they have so much energy that when they collide with bound electrons in the valence band, the bound electrons are ionized into the conduction band. This results in a type of carrier multiplication, known as impact ionization. The newly ionized carriers, in turn, gain enough energy from the electric field that they, too, excite other bound electrons to the conduction band, resulting in an avalanche effect. Devices which utilize this behavior are therefore called avalanche photodiodes (APDs). This multiplication characteristic of avalanche photodiodes represents an internal gain mechanism that increases the responsivity of the device (Equations 3.15, 3.16), but contributes to the overall noise of the system, as discussed earlier.

$$M = \text{multiplication} = (I_m/I_p) \tag{3.15}$$

$$\mathscr{R} \rightarrow M\mathscr{R}_o \tag{3.16}$$

where: I_m = average total multiplied output current

$\mathscr{R}_o$ = unity gain responsivity

APD devices exhibit a higher gain due to the avalanche process (G>1), and will maintain their bandwidth as long as the avalanche process is dominated by the carrier type with the higher ionization rate.[29]

Another device which exhibits an internal gain mechanism is the phototransistor. The phototransistor is a transistor that uses one of its two p-n junctions as the "active"

region where light will be absorbed. The intrinsic current gain characteristic of the transistor increases the responsivity of the device, as for the APD. However, the larger device area of a phototransistor tends to increase its response time. Thus, phototransistors have also traditionally exhibited a trade-off between gain and bandwidth. However, as discussed in Chapter 2, much recent work has been dedicated to improving the bandwidth capacity of the device without sacrificing its inherent gain quality.

3.2.3 Amplifiers

The role of the amplifier in the receiver circuit is to amplify the photocurrent produced by the photodetector, such that it may be used in future processing. Again, depending on the application, the amplifier must meet certain performance requirements. For example, in fiber optic communications, the following requirements are important:

1. low noise
   - As mentioned for the photodetector, additional noise due to the amplifier circuitry makes the separation of signal from noise more difficult. Amplifier noise is usually dominated by the thermal noise of the configuration.

2. good bandwidth
   - The bandwidth of the amplifier is inversely proportional to its RC time constant. If the bandwidth of the amplifier is considerably smaller than that of the incoming signal, then information will be lost.

As with the photodetectors, amplifiers exist in a variety of configurations. However, there are three main categories:

1. low impedance
2. high impedance

3. transimpedance

The low impedance amplifier (Figure 3.3) is identified by its low input impedance. This allows the device to have a wide bandwidth by reducing its RC time constant. However, the low resistance value results in a higher thermal noise, thus lowering the SNR of the receiver.

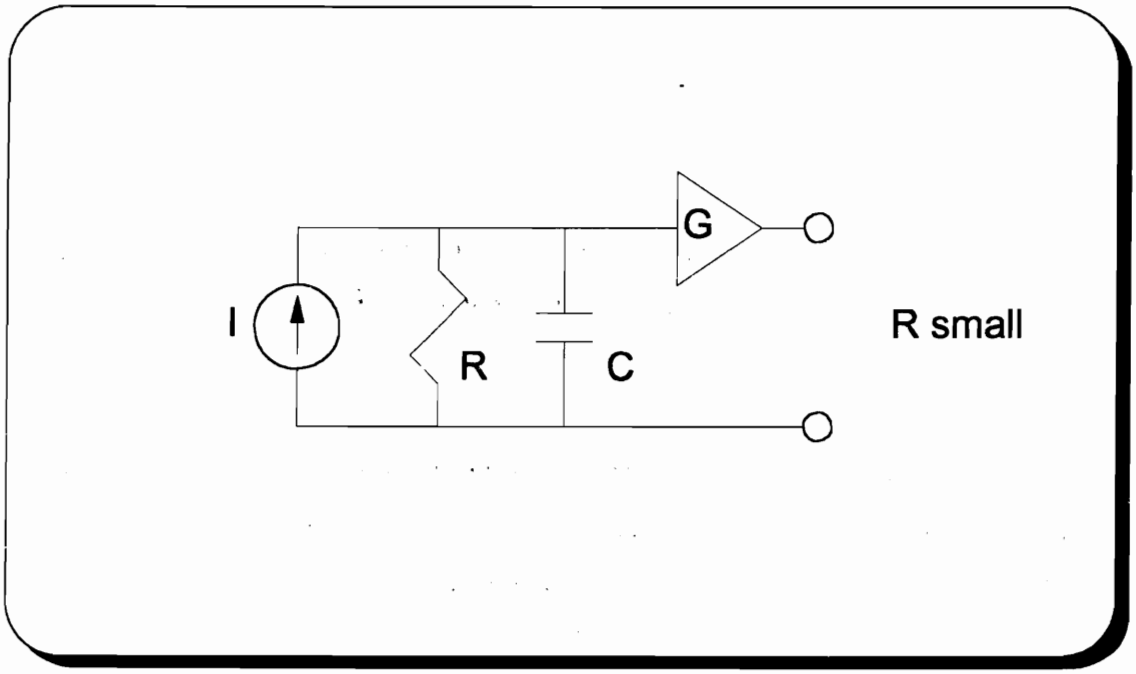

Figure 3.3 - Low impedance amplifier

The high impedance amplifier (Figure 3.4) is designed to minimize the amount of noise it introduces into the overall system. The use of a high input impedance does minimize the thermal noise of the amplifier. However, it also increases the RC time constant, which narrows the bandwidth of the device. To compensate for this, equalization techniques must be implemented into the system.

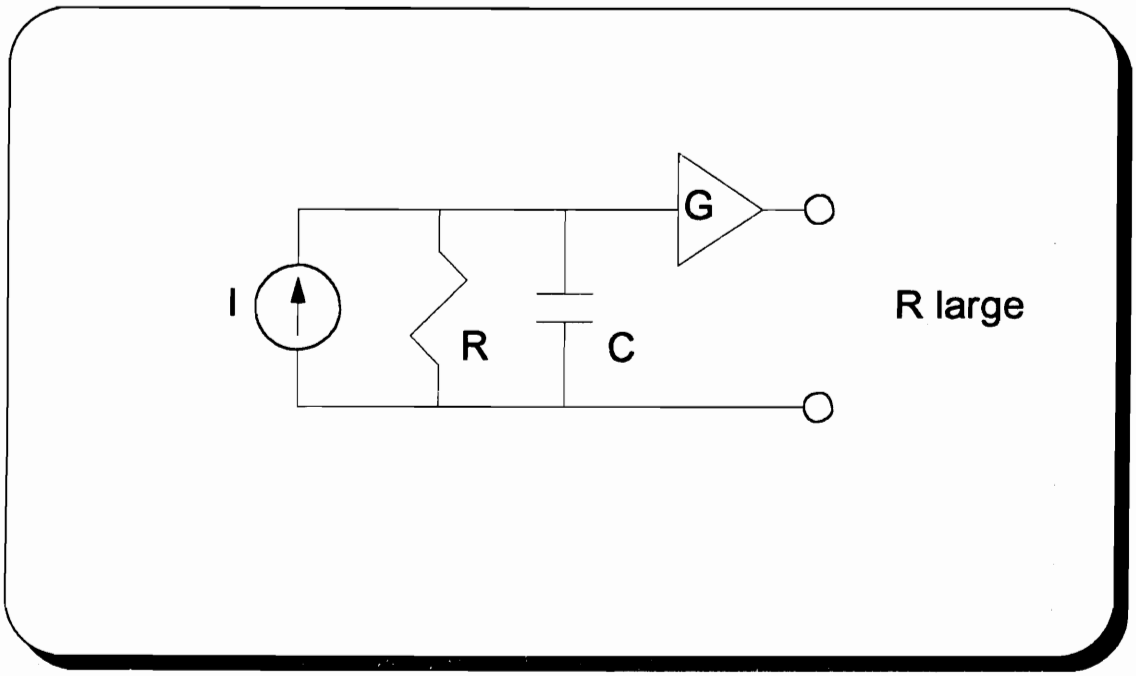

Figure 3.4 - High impedance amplifier

The transimpedance amplifier (Figure 3.5) combines the advantages of the low and high impedance amplifiers. This device utilizes a high input impedance amplifier with a negative feedback resistor. In this manner, the thermal noise is minimized by the high input impedance. However, the overall impedance of the device is reduced by the feedback resistor, thus lowering the effective RC time constant and widening the bandwidth.

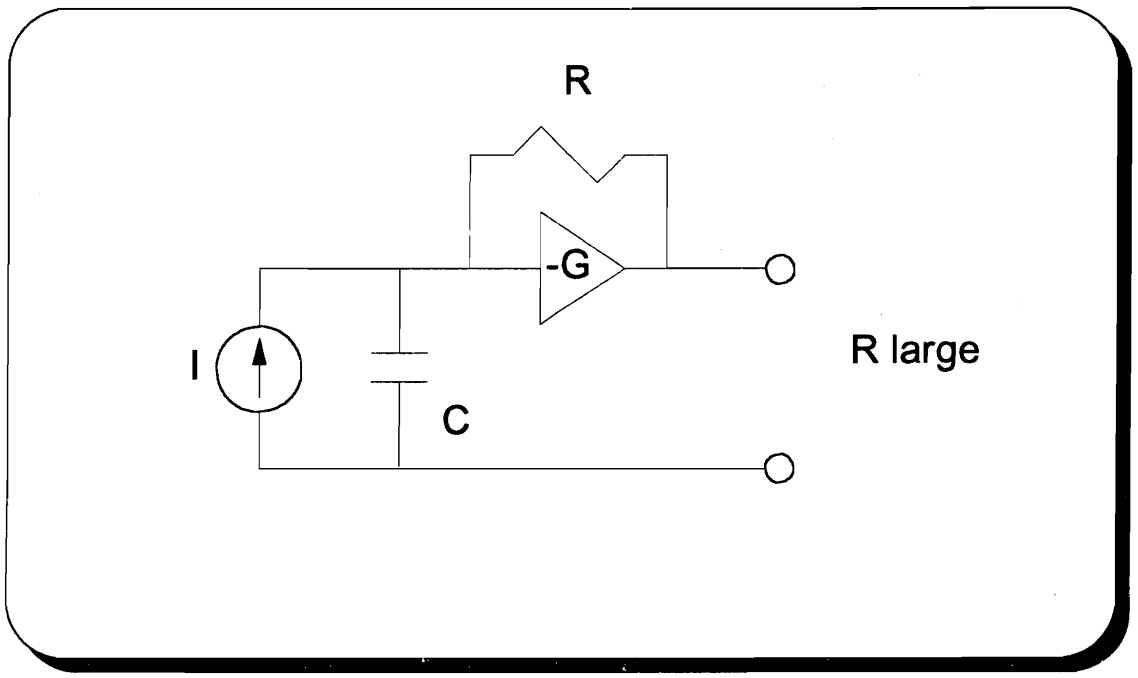

Figure 3.5 - Transimpedance amplifier

3.3 Experimental Procedures

3.3.1 Receiver Components

The first step in the construction of the fiber optic receiver is the determination of appropriate amplifier circuitry. A circuit based on the transimpedance configuration discussed earlier is identified from the literature.[30] This particular receiver is designed to operate at approximately 45 MHz. Thus, in order to perform some breadboard measurements (at 1 MHz), the filtering capacitors will be increased in value, accordingly.

An electrical-optical (E/O) converter, operating at 840 nm, and sinusoidally modulated at 1 MHz, will be used as the optical source for the receiver. The maximum input voltage level for the E/O converter is specified. A fiber optic tester is used to measure the power out of the E/O converter for various values of input modulation voltage. This will allow the determination of the optimum modulation voltage to use with the converter. These results will allow the maximum amount of light to be supplied to the receiver system. This is important, since some coupling losses are expected between the

converter pigtail and the optical fiber that is integrated within the receiver package (Figure 5.11). Figure 3.6 illustrates the results of the E/O converter test. Based on these results, the optimum modulation voltage is around 0.75 V_{p-p}. Note that an exact determination of the optical power input to the system is not possible, since it involves the measurement of the power out of an integrated (and therefore inaccessible) optical fiber. An alternative approach involves measuring the power out of the fiber prior to its integration. However, the process of inserting/removing the fiber tends to disrupt the pigtail-fiber alignment used in this test set-up.

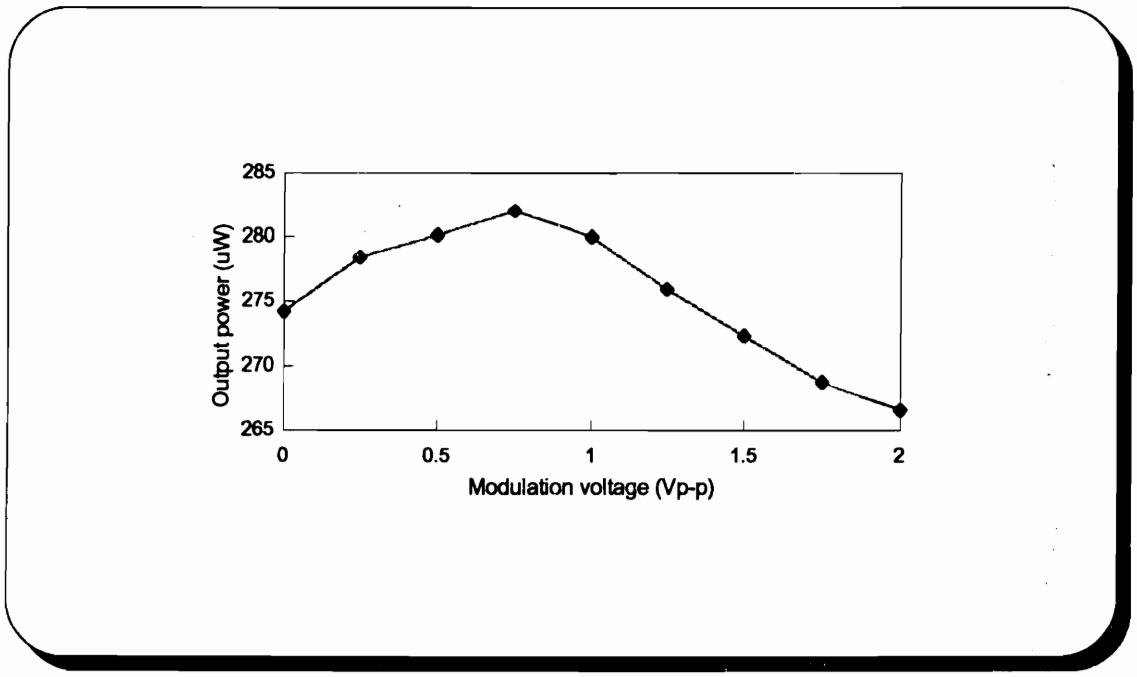

Figure 3.6 - E/O converter power output vs modulation voltage

A side-illuminated surface mount phototransistor (Si npn) is selected as the photodetector. As shown in Chapter 5, the side-illumination feature of the phototransistor is critical to the integrated package design, since the incoming fiber is parallel to the electronic components. A biasing scheme for the phototransistor is obtained from the literature.[31]

3.3.2 Breadboarding

A breadboarded version of the receiver circuit is constructed. Various tests are performed to optimize the system. For example, a modulation of 0.75 V_{p-p} input to the E/O converter produces noticeable distortion at the output of the receiver. Reduction of the modulation voltage to 0.3 V_{p-p} eliminates this distortion with little loss in the output power of the E/O converter (Figure 3.6). Based on data sheet information for the phototransistor, provided by the manufacturer, appropriate bias conditions are determined. An increase in V_{CE} results in an increase in the output photocurrent of the phototransistor. However, as V_{CE} increases, the dark current increases much more rapidly than the photocurrent, resulting in more noise. Therefore, V_{CE} must remain relatively low to minimize noise, and yet be large enough to produce significant photocurrent. Figure 3.7 illustrates the final receiver circuit, including the phototransistor and bias circuitry. The transimpedance portion of the amplifier system is comprised of transistors Q1 and Q2, and the feedback resistor (3.9 kΩ). The transistor Q3 provides additional gain.

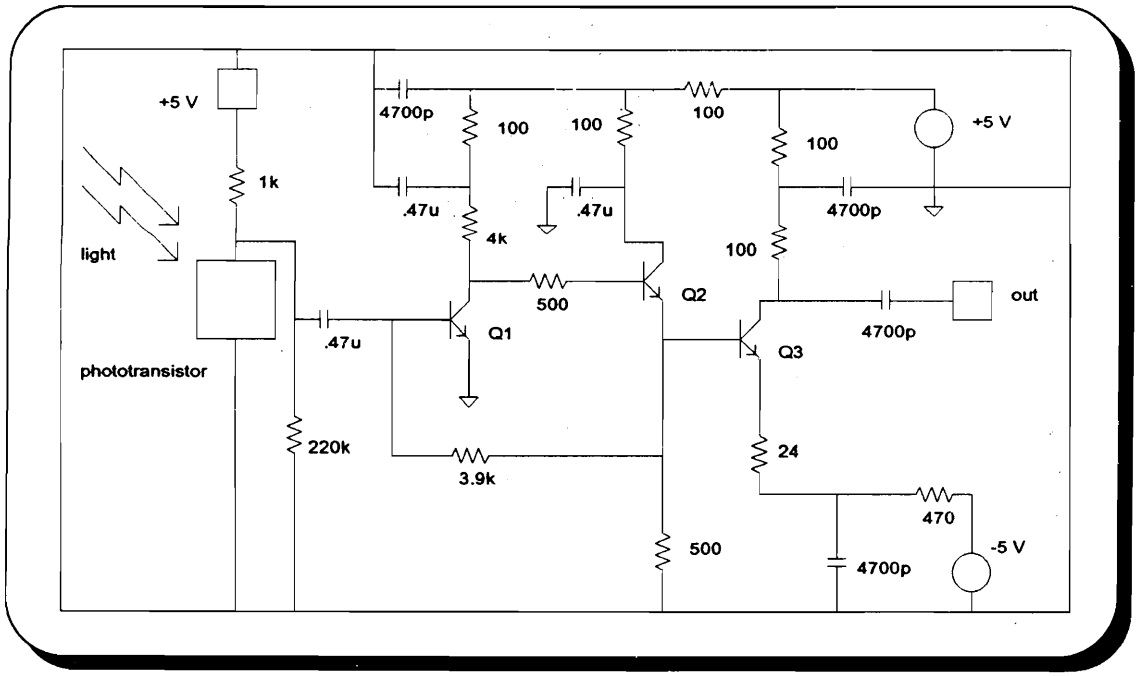

Figure 3.7 - Receiver circuit

3.3.3 Hybridization

The hybridization process begins with the design of the circuit layout. The circuit will be implemented with a low temperature cofireable ceramic (LTCC) material system. The DuPont Green Tape™ 851 tape system is used to conduct this research work. Note that the design must account for the approximately 12% shrinkage of the pattern that will occur with this material during processing. The circuit is drawn with AutoCAD® (Figure 3.8), and plotted on rubylith. The rubylith is peeled and a negative is made. A screen (325 mesh size, with 0.9 mil diameter wires intersected at a 90° angle) is emulsified with CDF-4 and allowed to dry. The negative is centered on the screen, and the screen is exposed to UV radiation to define the pattern. Several layers of Green Tape™ 851-AT are printed with the circuit pattern using DuPont 6142D paste and a de Haart printer. The printed layers are then dried at 120° C for 5 minutes, and are ready for future processing, as discussed in Chapter 5.

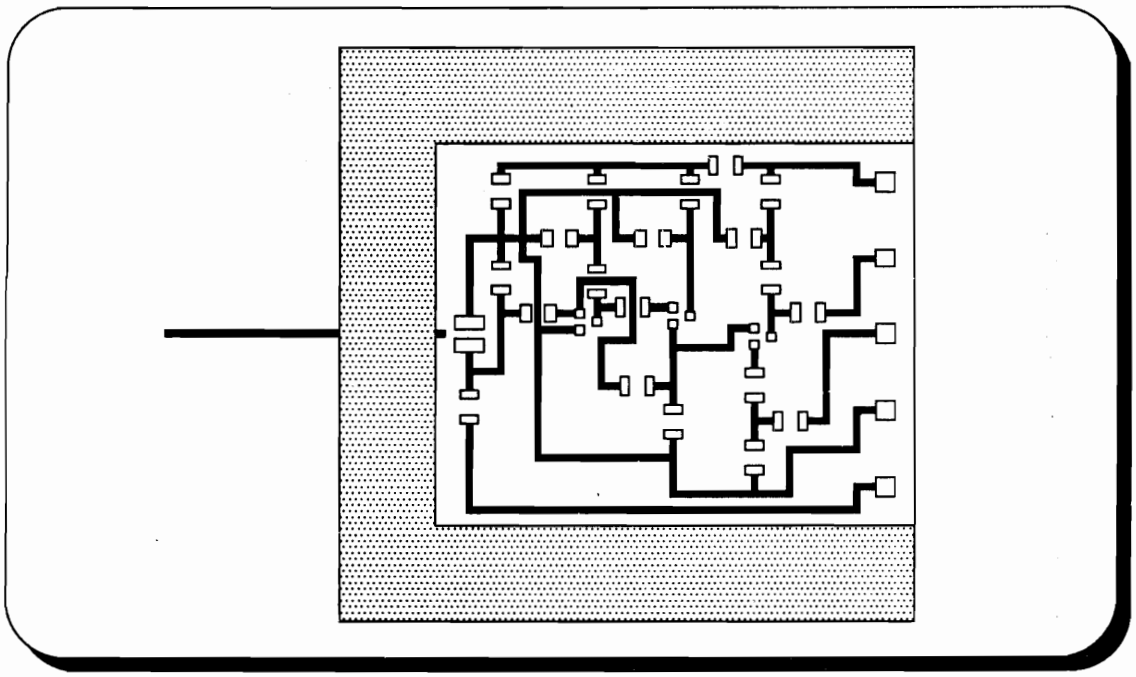

Figure 3.8 - Hybridized receiver circuit design

3.3.4 Testing

The overall development of the hybridized module begins with a computer simulation of the receiver circuitry, using PSpice® circuit simulation software. This provides a first check on the performance of the receiver circuit. A breadboarded version of the receiver circuit is then developed in order to test specific components, and investigate any discrepancies between the actual circuit behavior and the simulated responses. The practice of simulating and breadboarding the circuit is important so that time and materials are not wasted during the hybridization process. Both AC and DC measurements are made at several test points within the simulated, breadboarded, and hybridized receiver circuits. These results are shown in Table 3.1. Note that for simulation purposes, the phototransistor is modeled as a current source to represent the photocurrent input to the amplifier system.

Table 3.1 - Comparison of receiver tests

	breadboard		hybrid		simulated	
	AC	DC	AC	DC	AC	DC
base of Q1	10 mV_{p-p}	0.67 V	10 mV_{p-p}	0.67 V	7.4 mV_{p-p}	0.66 V
base of Q3	0.8 V_{p-p}	0.7 V	0.8 V_{p-p}	0.7 V	0.8 V_{p-p}	0.685 V
collector of Q3	2 V_{p-p}	2.95 V	2 V_{p-p}	2.90 V	2.05 V_{p-p}	3 V
phototransistor V_{CE}	3.35 V		3.45 V			

The transimpedance provided by the first stage (Q1 and Q2) of the amplifier system is approximately equal to the value of the feedback resistor (3.9 kΩ).[30] The simulation results indicate that the current input to this first stage is approximately 203 uA_{p-p}. Based on the value of the voltage at the output of the transimpedance stage (base of Q3), the simulated transimpedance is approximately 3.94 kΩ. The gain provided by the final stage (Q3) of the amplifier is designed to be 3.7.[30] The breadboard, hybrid, and simulated results of this final amplification stage all indicate a gain value of around 2.5. Some

discrepancy between the original circuit results and the current circuit results is expected due to different operation frequencies, and some uncertainty in the components used in the original reference. The discrepancy between the measured and simulated values of the AC voltage at the base of Q1 is likely due to error in reading from the oscilloscope, since this low signal level is significantly influenced by noise.

3.4 Signal-to-Noise Ratio Analysis

The original circuit of reference 30 used an APD as the photodetector. Since the APD has been replaced by a phototransistor, there is no avalanche noise and no need for a high voltage source to bias the APD. As discussed in the reference, there are four principal sources of noise in this receiver system:

1. thermal noise of the feedback resistor
2. shot noise of the base current of Q1
3. shot noise associated with the collector current of Q1
4. leakage currents in the photodetector

Of the above, the thermal noise of the feedback resistor and the shot noise of the base current of Q1 are identified as the dominant contributors.[30] Any contribution to the overall noise by the leakage and dark currents of the APD is also neglected. As shown by the manufacturer data sheets, the dark current of the phototransistor used in this work is approximately 0.2 - 0.3 nA. From simulation results, the average current into the base of Q1 is approximately 6 uA, which is four orders of magnitude greater than the noise current. Therefore, using Equations 3.1 and 3.2, a mean input noise current density for this receiver is defined:

$$\langle i^2/B \rangle = 2qI_{base} + \frac{4kT}{R_f} \qquad (3.17)$$

Using Equation 3.17, a value of 6.17 x 10^{-24} A^2/Hz is calculated for the noise current density of the receiver used in this work. This compares well to the value calculated in reference 30 of 6.07 x 10^{-24} A^2/Hz, as well as the measured value of 6.92 x 10^{-24} A^2/Hz. In order to evaluate the signal-to-noise ratio for this receiver, the bandwidth (B) must be determined. Measurements on both the breadboarded and hybridized receiver circuits yield a bandwidth value of approximately 500 kHz. Using equations 3.6, 3.8, and 3.17, the signal-to-noise ratio for this receiver is approximately 67 dB. This value is likely to drop for the much higher bandwidth systems.

Variation of the input power will also affect the SNR in the following manner. At relatively low signal levels, thermal noise tends to dominate over quantum (shot) noise. In this range, referred to as the thermal-noise limit, the SNR varies as the square of the incident optical power (P_{opt}^2). On the other hand, for large input signals, the quantum (shot) noise tends to dominate over the thermal noise. In this shot-noise limit range, the SNR varies linearly with the incident optical power. From Equation 3.17, the thermal noise current density component (approximately 4.3 x 10^{-24} A^2/Hz) is only slightly larger than the shot noise current density component (approximately 1.9 x 10^{-24} A^2/Hz), indicating that the input signal is somewhat large. This is most likely attributed to the presence of the phototransistor in this system. Recall that a phototransistor may generate a large photocurrent with a low level of incident optical power. As discussed in Chapter 2, this capability is due to the inherent current gain mechanism of the phototransistor which enhances its sensitivity over that of the pin. This effect of power level on the receiver SNR may be illustrated with the following example. First, if the incident optical power is decreased such that the average current into the base of Q1 is 90% lower (0.6 uA), then the SNR would drop sharply from 67 dB to 49 dB (approximately 27%). However, if the incident optical power is increased such that the average current into the base of Q1 is 90% greater (11 uA), then the SNR would only increase from 67 dB to 72 dB (approximately 7%).

These calculations assume that the phototransistor gain is constant over the range of input powers. However, the gain of phototransistors, like ordinary transistors, is generally a function of the device current. At low current levels (approximately $< 10^{-4}$ A), the gain of the transistor increases gradually with an increase in the current. At higher current levels (mA range), the minority carrier density becomes significant, resulting in a reduction in the injection efficiency of the device. Thus, the transistor exhibits a decrease in gain with increasing current, known as the Webster effect.[28] Many of the newer devices, however, have been achieved using better wafer fabrication techniques that remove the nonlinear gain effect at low current levels (by minimizing recombination currents). Assuming that this particular phototransistor exhibits this enhanced feature, then the gain of the device may be accurately considered as a constant for current levels below the mA range. Otherwise, any reduction in the gain capability of the phototransistor would result in a lower receiver SNR.

3.5 Equipment

3.5.1 Evaluation and Testing Equipment

This section discusses the equipment used to test and evaluate the breadboarded receiver circuit prior to integration within the LTCC package. Primary materials include the breadboard components, Siemens SFH 325 phototransistor, EXFO FOT-51 fiber optic tester, and Tektronix equipment (2465B 400 MHz oscilloscope, FG504 40 MHz function generator, PS503A dual power supplies, and OT502 E/O converter).

3.5.2 Fabrication and Processing Equipment

This section discusses the equipment used in the processing of the printed receiver circuit layer to be integrated into the package (Chapter 5). Primary equipment includes photolithography materials (rubylith, Kodak film (Kodalith ortho film, type 3), developer, stop bath, fixer, 325/0.9 mesh screen, and Ulano CDF-4 emulsion), Green Tape™ 851-AT, DuPont 6142D silver paste, de Haart screen printer, and Blue-M drying oven.

3.6 Results and Conclusions

This chapter has discussed the fiber optic receiver portion of the integrated optoelectronics package. The role of the receiver, as well as the two main components of the receiver (the photodetector and the amplifier) have been identified. A main contribution of this chapter has been the identification and evaluation of factors that influence the performance of the receiver system. From these guidelines, proper components may be selected for the realization of a fiber optic receiver system. This level of individual component evaluation is indicative of the selectivity provided by the integration technique proposed in this work.

The chapter has provided a discussion of the various types of noise that influence a receiver system, including their origins and analytical expressions. The two primary components of the receiver system are then treated in greater detail. The role of the photodetector is discussed, in addition to some general requirements of a photodetector for use in fiber optic communications applications. A number of different photodetector types have been reviewed, including an analysis of their figures of merit and performance characteristics. The role of the amplifier in the receiver system is also discussed. Again, some general requirements of an amplifier for use in fiber optic communications applications are mentioned. The three main amplifier configurations are identified, including the performance characteristics of each.

The analyses described above have led to the selection of the phototransistor and the transimpedance amplifier configuration, in order to produce a high performance system. Individual components of the receiver system, including the E/O converter, the photodetector and associated bias, and the amplifier circuitry, have been modified and/or optimized for use in this particular work. The E/O converter has been tested, separately, in order to determine the optimum modulation conditions that will provide the maximum optical input to the receiver system. The APD of the original circuit has been replaced with a phototransistor, thus requiring a different biasing scheme. The amplifier circuitry has been modified for operation at a lower frequency. This allows additional verification

of the receiver circuit through breadboarding techniques. Experimental results have been presented for the receiver circuit in breadboarded, hybridized, and computer simulated versions, all of which are in excellent agreement. In addition, an analysis of the noise in the system has been performed and compared to values stated in the literature. Experimental measurements of the system bandwidth have also allowed the determination of the signal-to-noise ratio for this particular receiver.

Chapter 4 will discuss the planar optical waveguide, which may also be integrated within the optoelectronic package. This chapter reviews the structure and operation of planar optical waveguides, but will mainly focus on optical materials and processing techniques used in the fabrication of these devices.

Chapter 4
Materials for Planar Optical Waveguides

4.1 Introduction

The planar optical waveguide is an important component in any integrated optoelectronics system. It must provide a quality, reliable link between the "planar" electronics and the cylindrical optical fiber. In addition, some levels of integration may require waveguides to perform more active tasks such as coupling, filtering, modulating, and switching. This chapter reviews the structure and operation of planar waveguides, however, will focus primarily on optical materials and the techniques used to process these materials for planar waveguide realization.

4.2 Background

A planar optical waveguide, like an optical fiber, is composed of two main regions- the core, through which the optical signal travels, and the surrounding cladding which helps confine the light to the core region. Each of these regions varies in complexity, depending on the requirements of the application. In general, the core material exhibits a higher index of refraction than the cladding in order to allow total internal reflection of the traveling light signal.

The refractive index of a material is a measure of the speed of light in that material relative to the speed of light in a vacuum (Equation 4.1).

$$n = \frac{c}{v} \qquad (4.1)$$

where n = refractive index of the material

c = speed of light in a vacuum

v = speed of light in the material

The concept of total internal reflection may be explained by considering the reflection and refraction of light rays at the interface of two different materials (Figure 4.1). The relationship between the indices of refraction and the angles of reflection and refraction is given by Snell's law (Equation 4.2).

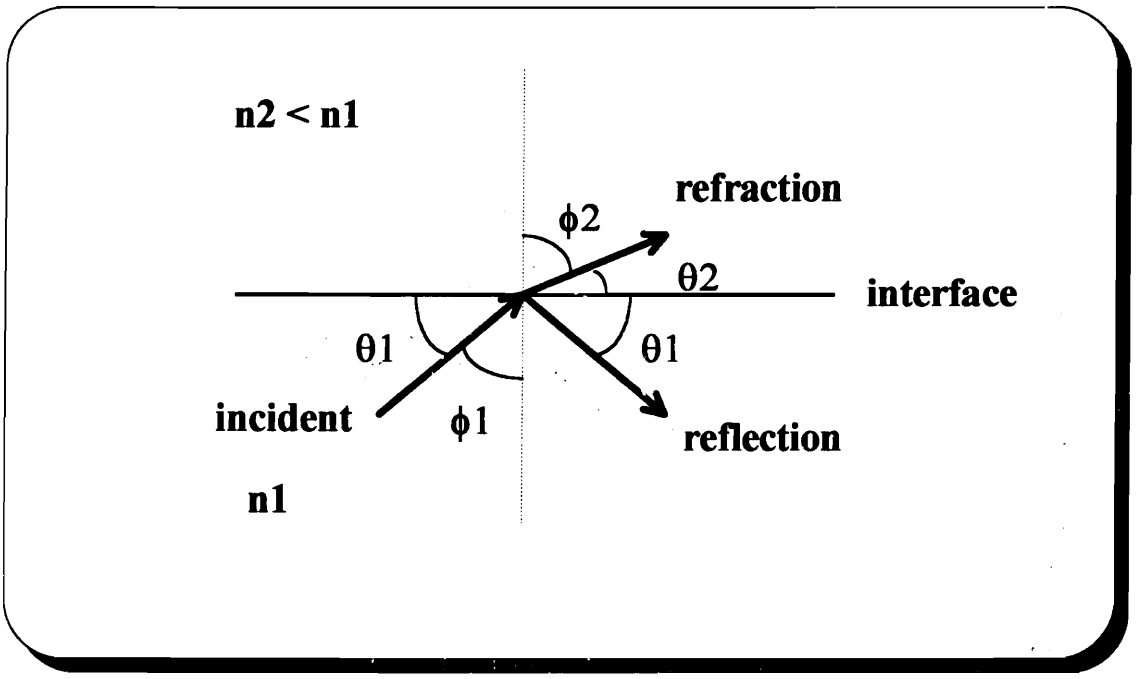

Figure 4.1 - Reflection and refraction of light rays at an interface[1]

$$n_1 \sin\phi_1 = n_2 \sin\phi_2 \qquad (4.2)$$

or equivalently,

$$n_1 \cos\theta_1 = n_2 \cos\theta_2$$

Total internal reflection occurs when the refracted light ray no longer penetrates into the other material, as shown in Figure 4.2. The incident angle at which this phenomenon begins is called the critical angle (θ_c). From Snell's law, one may write Equation 4.3.

$$\theta_c = \arccos\left(\frac{n_2}{n_1}\right) \qquad (4.3)$$

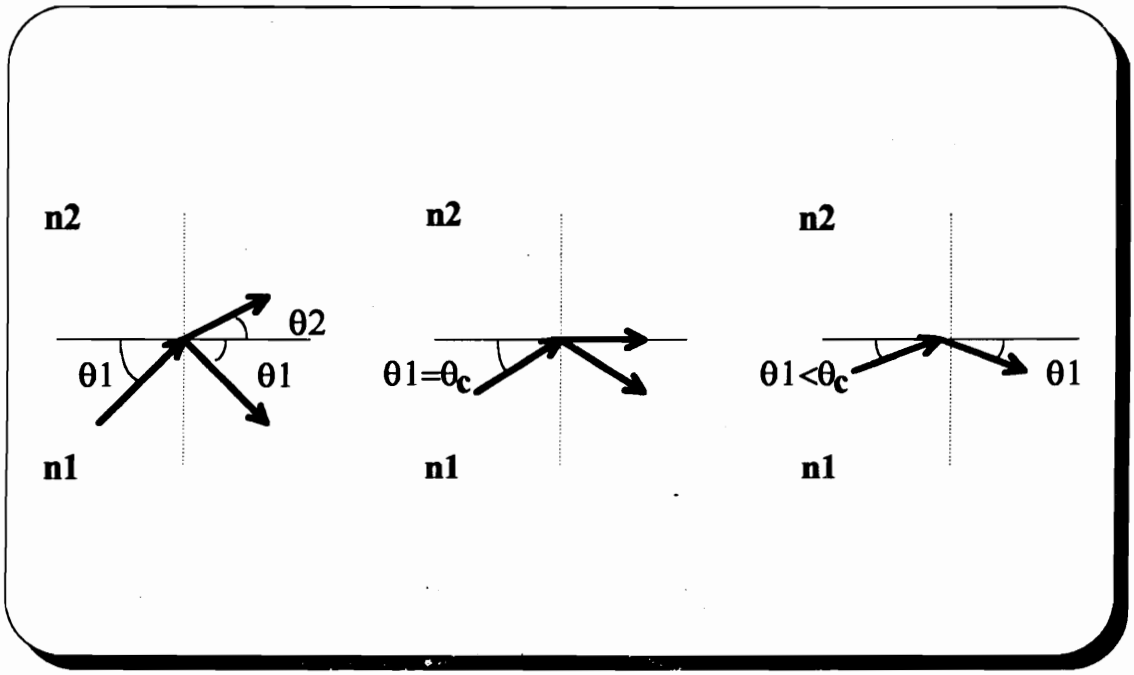

Figure 4.2 - Total internal reflection[1]

For incident angles less than the critical angle ($\theta_1 < \theta_c$), no refraction is possible, and total internal reflection is maintained. From Equation 4.3, it is clear that total internal reflection requires $n_1 > n_2$, as the arccos of values greater than unity is not defined for real values of θ_c.[1]

The materials used in the formation of an optical waveguide must also exhibit low-loss characteristics, in order to effectively propagate the signal with minimal use of expensive repeater systems. The loss (or attenuation) of a waveguide is expressed by Equation 4.4.

$$\alpha = \frac{10}{L}\log\left(\frac{P_{in}}{P_{out}}\right) \qquad (4.4)$$

where α = attenuation (dB/cm)

L = length of the waveguide (cm)

P_{in} = power coupled into the waveguide

P_{out} = power coupled out of the waveguide

The primary loss mechanisms in an optical waveguide are absorption, scattering, and radiative (or bending) losses. Absorption losses may be attributed to several factors, including defects in the waveguide material at the atomic level, impurities in the waveguide material (extrinsic), as well as the absorbing nature of the waveguide material, itself (intrinsic). Scattering (Rayleigh) losses often arise from inhomogeneities and defects in the composition of the waveguide. Finally, radiative (or bending) losses may be separated into two types - macroscopic and microscopic. Macroscopic radiative losses occur when the waveguide changes direction, while microscopic radiative losses are due to small fluctuations in the physical structure of the waveguide.[1] Therefore, loss characteristics will be influenced, not only by the type of material used, but also by the techniques used in processing the material into a planar waveguide structure.

The simplest planar waveguide is the two-dimensional (2-D) planar waveguide, or the slab waveguide (Figure 4.3). In this figure, n_1 is the index of refraction of the core, and n_2 and n_3 represent the indices of refraction of the cladding regions.

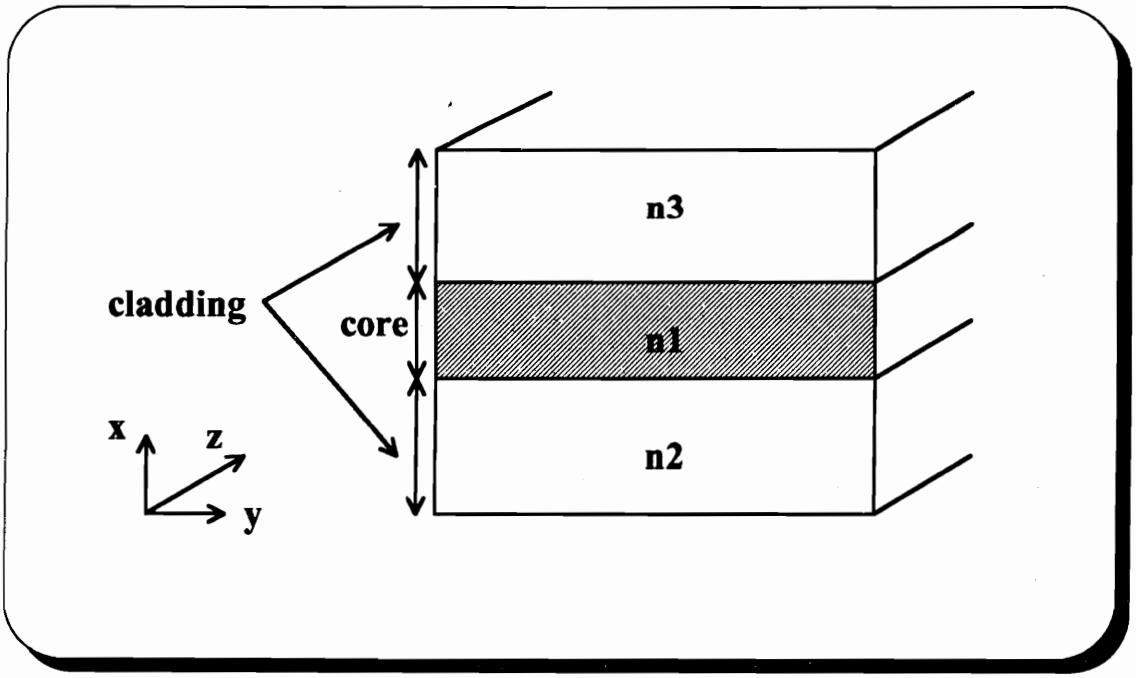

Figure 4.3 - Slab waveguide

As mentioned earlier:

$n_1 > n_2 \geq n_3$ (in general)

If $n_2 = n_3$, then the structure is called a symmetric slab waveguide, and

if $n_2 \neq n_3$, then the structure is called an asymmetric slab waveguide.

Due to its simple geometry (no y-dependence), the operation of the slab waveguide may be described with simple mathematical expressions. The mathematical analysis of planar waveguides begins with Maxwell's Equations (Equations 4.5 - 4.8).[1]

$$\nabla \times \mathbf{E} = -\frac{\partial \mathbf{B}}{\partial t} \tag{4.5}$$

$$\nabla \times \mathbf{H} = \frac{\partial \mathbf{D}}{\partial t} \tag{4.6}$$

$$\nabla \bullet \mathbf{D} = 0 \tag{4.7}$$

$$\nabla \bullet \mathbf{B} = 0 \tag{4.8}$$

where:

$\mathbf{D} = \varepsilon \mathbf{E}$ and $\mathbf{B} = \mu \mathbf{H}$

Using vector manipulation, Maxwell's relationships may be expressed in terms of the wave equations (Equations 4.9, 4.10).[1]

$$\nabla^2 \mathbf{E} = \varepsilon \mu \frac{\partial^2 \mathbf{E}}{\partial t^2} \tag{4.9}$$

$$\nabla^2 \mathbf{H} = \varepsilon \mu \frac{\partial^2 \mathbf{H}}{\partial t^2} \tag{4.10}$$

Since the propagation of light waves down the waveguide (z-direction) is the primary concern, the analysis will be limited to traveling wave solutions (Equations 4.11, 4.12).

$$\mathbf{E} = \mathbf{E}_o(x,y)e^{j(\omega t - \beta z)} \tag{4.11}$$

$$\mathbf{H} = \mathbf{H}_o(x,y)e^{j(\omega t - \beta z)} \tag{4.12}$$

Two independent sets of solutions, corresponding to the transverse electric (TE) and transverse magnetic (TM) fields, may then be separated out from the above vector expressions. By applying appropriate boundary conditions, separate "characteristic" or "eigenvalue" equations are established for the TE and TM solutions. Discrete solutions of these equations correspond to the operating "modes" of the waveguide. One important expression in waveguide analysis is the cutoff frequency. This is often used to find the frequency at which the device switches from multimode operation to single mode operation.[32]

For example, the "normalized" cutoff frequency, v_c, for TE_m modes is of the form:

$$v_c = \left(\frac{1}{2}\right)\arctan\left(\sqrt{\frac{n_2^2-n_3^2}{n_1^2-n_2^2}}\right) + \frac{m\pi}{2} \qquad m=0,1,2,... \tag{4.13}$$

By definition, $v_c \equiv k_{oc} a\sqrt{n_1^2 - n_2^2}$ (4.14)

and: $k_{oc} = \frac{2\pi}{\lambda_c}$ (4.15)

where: λ_c = cutoff wavelength
k_{oc} = cutoff propagation constant
(2a) = thickness of the core layer

Therefore, for single mode (TE_o) propagation:

$$\arctan\left(\sqrt{\frac{n_2^2-n_3^2}{n_1^2-n_2^2}}\right)\left(\frac{1}{k_o\sqrt{n_1^2-n_2^2}}\right) < 2a < \left(\arctan\left(\sqrt{\frac{n_2^2-n_3^2}{n_1^2-n_2^2}}\right) + \pi\right)\left(\frac{1}{k_o\sqrt{n_1^2-n_2^2}}\right) \tag{4.16}$$

However, a planar waveguide is often used as a coupling device from a fiber to an electronic component. Thus, in order to maximize the coupling efficiency, there should be confinement of light in the y-direction as well as the x-direction. This creates a three-dimensional structure, called a rectangular waveguide, that is much more difficult to analyze (Figure 4.4).

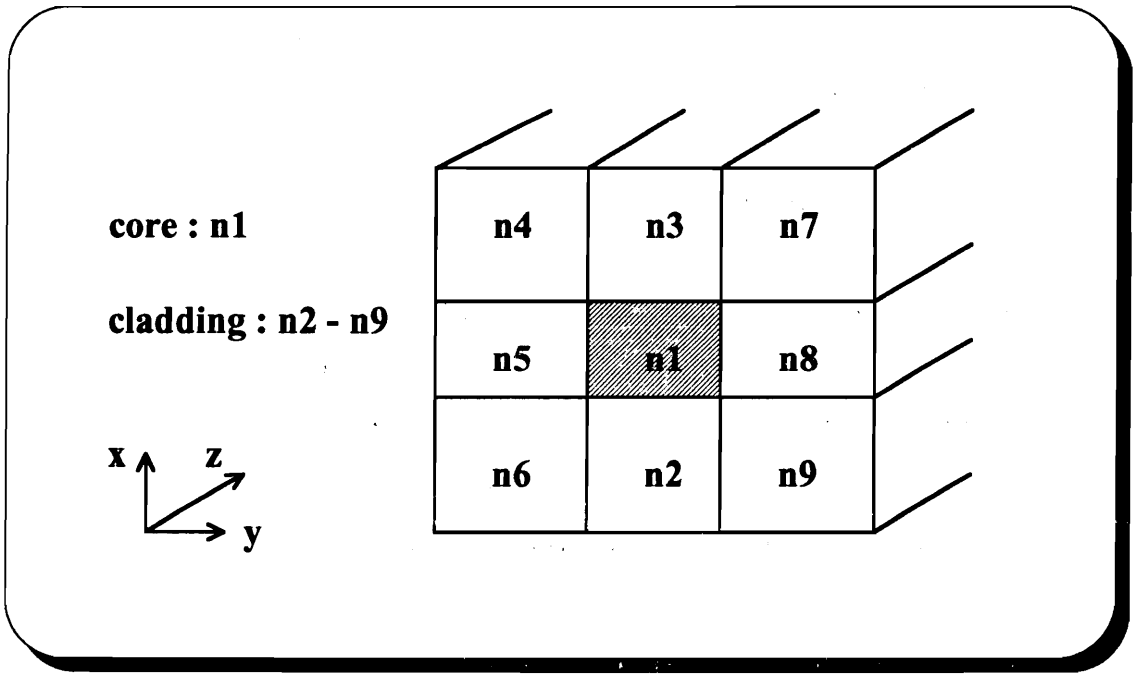

Figure 4.4 - Rectangular waveguide

Unlike the slab waveguide, an exact mathematical analysis of this structure is not possible. Instead, numerical approximation techniques must be implemented. One example is the effective index method which combines a 2-D analysis in the x-direction with a 2-D analysis in the y-direction.[32]

4.3 Materials for Optical Waveguides

This section will focus mainly on some of the materials used for optical waveguides, and the techniques used to fabricate them. First, selection of appropriate

materials and suitable fabrication techniques is dependent on satisfying the following criteria:[33]

1. It must be possible to vary the refractive index of the material on the order of 10^{-4}.
2. It must be possible to control the waveguide thickness to within a small fraction of a micron (thin films).

(items 1. and 2. are important in controlling the number of modes as well as allowing reproducibility)

3. It must be possible to use conventional techniques in defining the waveguide geometry with accuracy and reproducibility.
4. The material must have a high transparency at the operation wavelengths to reduce propagation losses.
5. The material must have very few defects to reduce propagation losses and, in some cases, prevent intermodal coupling.
6. The material must demonstrate both environmental and temporal stability.

Many of the materials used for optical waveguides also posses special properties that make them useful in forming more complicated structures and devices. For example, some materials are characterized as electrooptic, in that their optical properties are influenced by the application of an external electric field. Two phenomena related to this characteristic are the Pockels effect and the Kerr effect. The Pockels effect occurs when the change in the refractive index of a material is directly proportional to the applied field. The Kerr effect occurs when the refractive index change is proportional to the square of the applied electric field. Electrooptic materials have been used in applications such as modulators and memory devices.[34]

Another property that is related to the electrooptic effect is the photorefractive effect. Photorefractive materials experience a change in their optical properties upon absorption of light, by the following four-step process:[35]

1. Electric charge carriers are generated through photon absorption.
2. The charge carriers diffuse to regions of lower charge carrier concentration.
3. Eventually, the charge carriers become trapped at defect sites away from the photon absorption regions.
4. These trapped charge carriers create space-charge electric field regions, which produce changes in the optical properties of the material via the electrooptic effect.

The first photorefractive materials studied were also ferroelectric materials, including $LiNbO_3$ (lithium niobate) and $BaTiO_3$ (barium titanate). Ferroelectric is a term often given to crystals that experience a change in polarization upon application of an electric field.[35,36]

The electrical and optical properties of some materials are sensitive to stress and strain. Materials whose electrical properties are affected by mechanical stress are often termed piezoelectric.[37] Common applications for piezoelectric materials include transducers (such as microphones, headphones, and speakers) and resonators. On the other hand, materials whose optical properties are affected by stress and strain are called photoelastic.[37] One field which uses the photoelastic effect is acoustooptics. Acoustooptics is concerned with the interaction of sound and light, in that the stress and strain fields associated with sound waves propagating through a photoelastic material will induce a refractive index grating in that material. Common acoustooptic applications include modulators, filters, and switches.[38]

4.3.1 Glasses and Inorganics

Glasses and inorganic materials have attracted research as waveguide candidates for a number of reasons. Glasses exhibit high transparency and optical quality in the

visible and near infrared (near IR) regions. They are available in a wide range of refractive indices (1.4 - 2), are inexpensive, and can incorporate additive chemicals for tailored needs. In addition, glasses can allow for simple waveguide fabrication, they are environmentally stable, and (some) are moldable (i.e. alignment grooves may be formed for coupling to optical fibers).[33]

Various techniques exist for fabricating glass waveguides. The simplest example is the deposition of a different material on a glass substrate by means of evaporation, sputtering, lamination, chemical solutions, etc. Evaporation and sputtering are both performed under high vacuum conditions. In evaporation, the material to be deposited is evaporated by a filament, and condenses on the substrate to the desired thickness. In sputtering, the material to be deposited is struck by accelerated ions from a heated plasma, releasing ions which coat the substrate. Sputtered films are generally more compact and have better adhesion than evaporated films, and thus tend to produce a higher quality guide. Chemical solution deposition is an alternative for materials that can be dissolved in a suitable solvent. In this method, a thin coat of the solution is deposited on the substrate by spin-, dip-, or spray-coating. The solvent is then allowed to evaporate away naturally, or by baking. This technique is useful for large-area guides and inhomogeneous layers. Typical losses for guides produced through chemical solution are well below 1 dB/cm. The simplicity of this design is due to only two limitations on the choice of materials: refractive index and stability during the processing steps. As discussed in Chapter 2, more recent techniques have also utilized chemical vapor deposition (CVD) methods.[10,11]

A more popular example of waveguide fabrication is the formation of the guide directly within the glass substrate. This is usually performed through ion exchange or diffusion. In summary, diffusion is a two-step procedure in which a layer of the dopant material is deposited on the substrate by evaporation, sputtering, or chemical means. The temperature is increased to the diffusion temperature (usually ~ 1000° C), and the waveguide is formed. The characteristics of the waveguide are determined by the composition and thickness of the film, as well as the diffusion time. Typical waveguides

produced in this manner exhibit very low losses (~ 0.1 - 0.2 dB/cm in the near IR) and high stability (due to the high processing temperature). Ion exchange is used more frequently than diffusion due to its simplicity, low-cost, and flexibility. A glass containing a suitable mobile ion is placed in a molten salt containing an exchangeable ion. Diffusion of ions occurs under a potential and concentration gradient, producing a refractive index change that is linearly related to the concentration of the exchangeable ion. The flexibility gained by using this technique is, however, at a price, since more limitations are placed on the choice of glass. These limitations are summarized as follows:[33]

1. Sufficiently high content of mobile ions to allow an easy exchange in a reasonably short period of time
2. Chemical stability in the presence of strong reactive melts
3. Transition temperature compatible with processing temperature (250 - 500° C)
4. High purity
5. Absence of bubbles, inclusions, etc.

A variety of glasses are used in the fabrication of waveguides by ion exchange. Soda-lime and borosilicate glasses are the most frequently used, having intrinsic losses below 0.01 dB/cm. However, glass manufacturers are developing special glasses that are tailored to specific needs. Such glasses exhibit higher durability and allow more control over the index profile and value.

Inorganic materials are also gaining interest among researchers due to some interesting and useful properties. Some inorganics have refractive indices that are unusually high or that can be varied over a wide range. This permits the waveguide to be coupled efficiently to devices formed from many different types of materials. Others, such as ZnO (zinc oxide) and PLZT (lead-lanthanum zirconate titanate, a transparent ferroelectric ceramic), possess piezoelectric properties. ZnO has been useful in forming guides with good acoustooptic characteristics, while PLZT has been used in a variety of

electrooptic applications. Inorganic waveguides are usually fabricated through evaporation, sputtering, or chemical solution. Waveguide loss, which is typically high immediately after deposition, can reach as low as a few 0.01 dB/cm after annealing.

4.3.2 Polymers and Organics

Polymers and organic materials offer a low-cost alternative to glass and inorganic waveguides. While providing the same order of loss as glass/inorganic waveguides, polymer and organic waveguides offer additional flexibility by allowing deposition on many types of substrates, including non-planar surfaces, and the design of special films for individual applications. Polymer materials are also highly transparent at several important fiber optic wavelengths, including 670 nm, 780 - 840 nm, and 1300 nm. Despite these advantages, polymers and organics suffer from poor environmental stability.[33]

As was the case for inorganic materials, polymers and organics may be laminated, spray-coated, or dip-coated. Definition of the waveguide may be performed in a variety of ways. One popular technique is through etching/polymer-removal. Standard photolithography techniques are used to form a guide by etching away all of the polymer film except for a strip that will become the waveguide.

As discussed in Chapter 2, research into polymer waveguides has been active over recent years.[15-17] Some of these techniques are based on the processes of photolocking and photobleaching. Photolocking refers to the local change in refractive index caused by the selective diffusion of monomers within the polymer, in response to an exposure to light. Photobleaching refers to the decrease in the refractive index of a material caused by exposure to UV light, and is used to form cladding regions around unbleached waveguide regions.[15]

4.3.3 Single Crystals

An alternative to the amorphous materials discussed so far is the single crystal waveguide. Due to the complexity of the crystal growth process, however, these materials

are more expensive than those previously mentioned. Nevertheless, there are sufficient advantages gained by using single crystal waveguides to attract a great deal of research. In general, they possess much higher refractive indices and a much wider transparency range. Methods of fabricating single crystal waveguides include diffusion, ion exchange, epitaxial growth, and thin film deposition.

The most widely used and studied crystal is lithium niobate ($LiNbO_3$).[33] Due to its high Curie temperature (~ 1150° C), the crystal can withstand the high temperature diffusion process. Note that the Curie temperature represents the temperature above which the magnetization (or electric polarization) of the material changes from its normal state. $LiNbO_3$ is transparent in the range from 0.4 um to 4.5 um, and exhibits propagation losses on the order of 0.1 dB/cm. In addition, it possesses electrooptic, acoustooptic, piezoelectric, pyroelectric (change in polarization with a change in temperature),[39] photoelastic, and photorefractive properties, lending itself to a wide array of applications. As explained in Chapter 2, there are basically two main techniques in forming waveguides in $LiNbO_3$: titanium diffusion and proton exchange.[18]

Other single crystals of interest include lithium tantalate ($LiTaO_3$) and garnets. Lithium tantalate also exhibits a wide transparency range (0.45 um to 4.5 um) and losses less than 1 dB/cm. However, its Curie temperature (~ 610° C) basically limits it to fabrication by proton exchange. Garnets are characterized by their strong magnetooptical properties (change in optical properties with an applied magnetic field).[40] One example, YIG (Yttrium Iron Garnet), is used as an epitaxial layer grown by liquid phase epitaxy on GGG (Gallium Gadolinium Garnet). The transparency range of YIG/GGG is 1.1 um to 5 um, and it exhibits losses greater than 1 dB/cm.

4.3.4 Semiconductors

The use of semiconductors as waveguide materials is driven by monolithic technologies in which all devices are integrated on a single wafer chip. Until recently, impurities and defects in semiconductor materials produced high guide losses. Now,

losses have dropped to 0.2 to 1 dB/cm.[33] The most important semiconductors may be grouped into three categories: Silicon (Si), III-V compounds (GaAs, InP), and II-VI compounds (CdTe). Silicon is the most established technology due in part to its low cost and the availability of quality material. It has limited use as a waveguide material, however, due to the limited wavelength range of associated Si devices (< 1 um). III-V compounds are a more expensive, yet more flexible, alternative. Waveguides from III-V materials may be fabricated in a variety of ways, including epitaxial growth, diffusion, and ion implantation. Characteristics such as the band gap, transparency range, and refractive index of III-V materials are functions of the composition. For example, the ternary $Ga_{x-1}Al_xAs$ is well matched to GaAs, and has a lower refractive index (which can be varied by changing x), thus providing the ideal cladding material. As discussed in Chapter 2, quaternary compounds provide even more flexibility.[19]

4.3.5 Thick Films

During the past decade, an interest has emerged in the use of thick film materials for the development of optical waveguides. Thick film optical structures offer several advantages over the already mentioned technologies, including low cost and compatibility with the well-established hybrid microelectronics technology.[20,21]

Thin film optical waveguides have proven useful in single mode applications, such as communication systems, due to their small size and low-loss characteristics. Thick film optical waveguides, on the other hand, are more compatible with multimode applications, and have been limited to more passive structures (branches, couplers, attenuators) due to their traditionally higher losses (15 - 30 dB/cm).[20] In addition, due to their larger size, thick film optical structures are being considered for use in power applications.[21]

Thick film optical pastes differ significantly from their electrical counterparts. Materials used in the composition of electrical thick film pastes are often not appropriate for use in optical paste compositions. For example, thick film pastes are comprised of glass additives that enhance the sintering of the paste components, and promote the

adhesion of the paste to the substrate. A common glass additive used in electrical thick film pastes is lead borosilicate. This glass has a low melting point which makes it compatible with conventional thick film firing profiles. However, the presence of lead oxide (PbO) gives the glass a high refractive index.[41] In many glasses, a high refractive index and a high dispersion (variation of refractive index as a function of the optical wavelength) tend to go together.[41] A dispersive optical waveguide will distort an optical signal as it travels along the guide, since some spectral components of the signal will travel faster than others. Also, as the number of different materials within a paste increases, the possibility of compositional variations in the resulting film also increases. This causes small variations in the refractive index throughout the glass. These variations are a type of scattering mechanism, and therefore contribute to the optical loss of the film.

The production of a quality thick film optical glass is further complicated by the need to avoid devitrification. Devitrification is the conversion of a material from the glassy to the crystalline state. Unfortunately for optical purposes, few material compositions are immune to devitrification. The presence of crystalline structures is detrimental to the optical performance of the film in two ways. First, the crystals act as direct scattering mechanisms within an otherwise homogeneous medium. Second, differences in the coefficient of thermal expansion (CTE) between the crystalline and glassy phases of the film can result in strain and cracking of the film (another scattering mechanism). Another important factor to consider is the CTE match between the optical thick film(s) and the substrate. CTE mismatch between film and substrate can induce strain and cracking within the film, and may even cause the film to separate from the substrate.

Thick film optical structures, however, are very similar to their electrical counterparts in their method of fabrication. A squeegee pushes the thick film paste through a pattern in a wire mesh screen, and onto a substrate. The print is allowed to settle in order to remove any mesh impressions. A low temperature drying stage is used

to burn off solvents in the paste. Finally, a higher temperature firing profile removes the remaining inactive materials, and promotes sintering and adhesion.

4.4 Experimental Procedures

4.4.1 Oxidation of Thermally Evaporated Ge on Si

Due to its photosensitive nature, as well as its low-loss characteristics (especially at long wavelengths),[42,43] germanium oxide (GeO_2) is a promising material for use in a wide array of planar optical waveguide applications. The overall goal of this chapter, therefore, is the development and analysis of both thin and thick film materials for use in planar optical waveguides, using GeO_2 as the primary component.

This section discusses a set of preliminary experiments, designed to gain an understanding of the oxidation characteristics of thin film Ge. These experiments will investigate the conditions necessary to oxidize Ge, in order to form various thicknesses of GeO_2 for use in thin film waveguide structures. Knowledge of the appropriate oxidation conditions (oxygen flow rate, peak temperature, and peak hold time) is important to the thin film waveguide designer. Control over the oxide thickness is critical, since the modal characteristics of the thin film GeO_2 waveguide are determined by the thickness of the film. The oxidation of Ge, like the oxidation of Si, is a "replacement" process. That is, when a layer of GeO_2 is formed, a certain amount (proportional to the amount of oxide formed) of Ge is consumed in the process. These experiments will therefore provide information on the conditions necessary to fully oxidize a layer of Ge into GeO_2. The oxidation process is relatively fast during the early stages, since the Ge is in full contact with the oxygen flow. However, as a layer of GeO_2 develops, the Ge is no longer in direct contact with the oxygen flow, and the oxidation process slows. The formation of GeO_2 from Ge is dependent on the oxidation time and temperature, as well as an adequate supply of oxygen. Like SiO_2, the thickness of the GeO_2 layer is expected to increase with both the oxidation time and temperature.

A thin layer (~ 3000 angstroms) of Ge has been thermally evaporated onto a silicon wafer. Small sections of this wafer are then oxidized in a tube furnace under different conditions. The oxide thicknesses are then measured by ellipsometry techniques (Section 4.5.2) through the provision of the index of refraction of GeO_2 (1.65).

The oxidation experiments will use a Lindberg Tube Furnace, an Omega CN3000 Controller, and an O_2 flow meter. The set of oxidation conditions, as well as the oxide thickness results are shown in Table 4.1 and Figures 4.5 - 4.7. The peak oxidation temperatures have been selected with the following considerations in mind. The temperatures are low enough such that the Ge does not melt (~ 940° C), and the diffusion of Ge into the Si wafer is minimized (diffusion coefficient ~ 10^{-16} cm^2/s at 1000° C).[28] However, the temperatures are high enough to allow the formation of reasonably thick GeO_2 layers in a relatively short period of time. Relaxed ramp rates are chosen to avoid inflicting any type of thermal stress on the samples. A typical oxygen flow rate (100 ml/min is selected to ensure an oxygen-rich environment for the formation of GeO_2. Since GeO_2 is the most stable oxide of Ge,[44] the formation of oxides other than GeO_2 is not expected to be a great concern.

Note that the ellipsometry data for the 900° C/1 hour, 800° C/5 hours, and 800° C/10 hours samples, however, are irregular. This tends to suggest the occurrence of some interaction among the materials, aside from the normal oxidation process. Thus, there is less distinction between the interfaces, making ellipsometry techniques more difficult. This interaction may be occurring at the Si/Ge interface. Much work has been done recently to try to understand the oxidation process in Si/Ge systems.[45-48] For example, in the presence of both Si and Ge, oxygen is much more likely to form SiO_2 than react with the Ge.[45] Alloys of Si and Ge, along with oxygen deficient oxides of Ge have also been observed during the oxidation of very thin layers (2 - 5 angstroms) of Ge on a Si wafer.[46] Some evidence also indicates that oxides of Ge formed at oxidation temperatures above 500° C may be deficient in oxygen.[47] Based on these observations, some degree of error may therefore be expected in the thickness measurements.

Table 4.1 - Oxidation of Ge on Si

peak temperature (°C)	peak hold time (h)	ramp rates (°C/min)	O_2 flow rate (ml/min)	oxide thickness (angstroms)
30 (control)	-	-	-	176
700	1	5	100	269
800	1	5	100	454
900	1	5	100	1,020
30 (control)	-	-	-	177
750	1	5	100	264
850	1	5	100	533
800	1	5	100	433
800	5	5	100	578
800	10	5	100	966

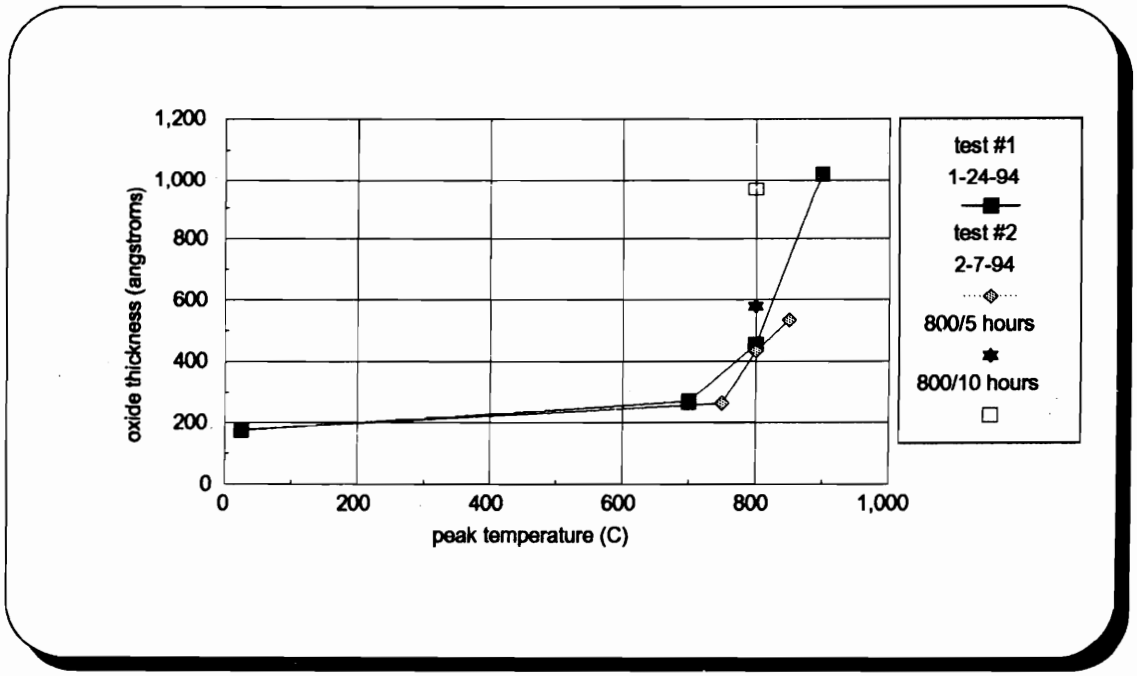

Figure 4.5 - Oxidation of Ge on Si

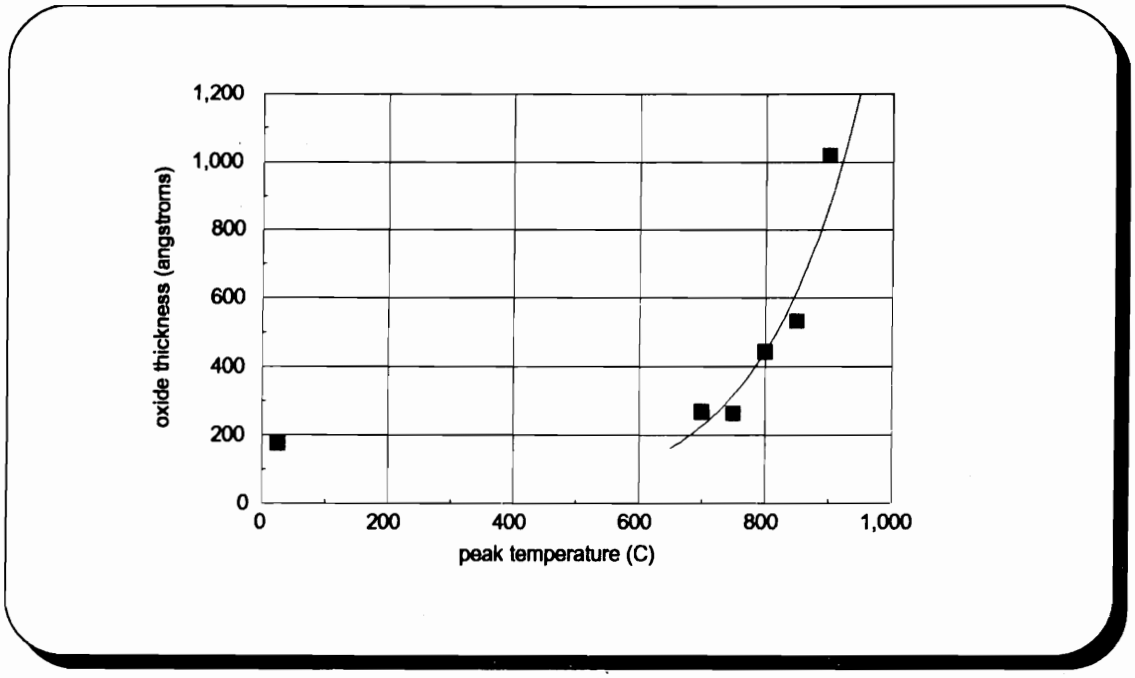

Figure 4.6 - Oxidation of Ge on Si

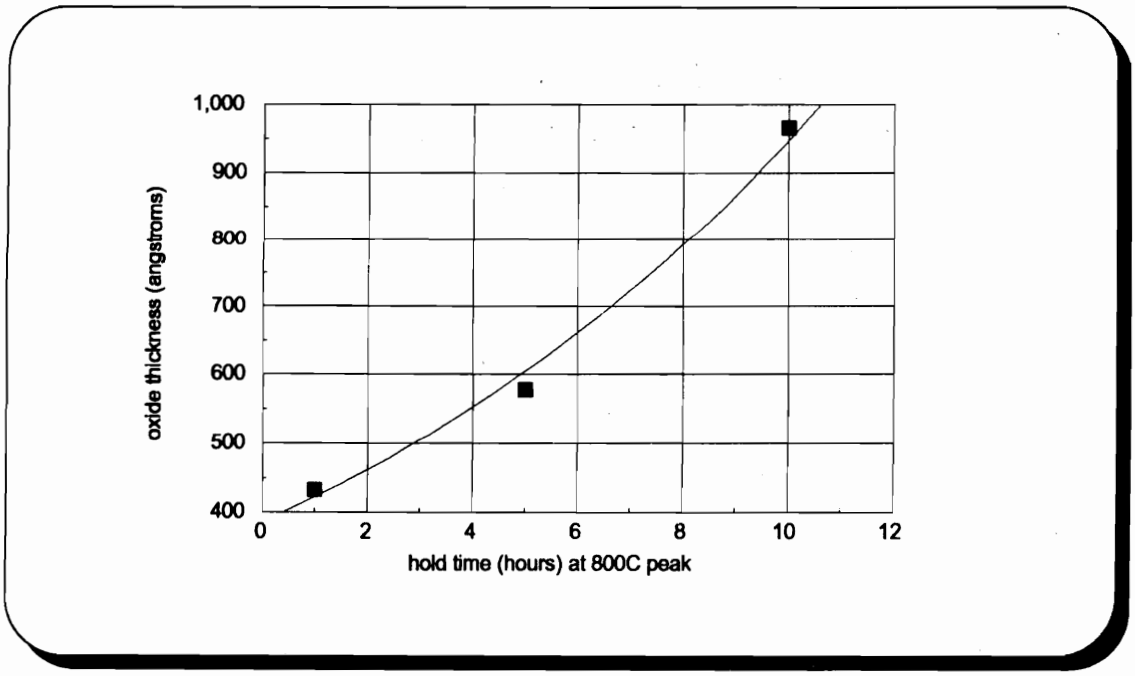

Figure 4.7 - Oxidation of Ge on Si

Another source of error in the thickness results is the value provided for the refractive index of bulk GeO_2 (1.65). The refractive index of a material in thin film form, however, may not be the same as that of the material in bulk form. This characteristic is often expressed in terms of a packing fraction (Equation 4.17).[49]

$$f = \frac{[(n_f^2 - 1)(n_b^2 + 2)]}{[(n_b^2 - 1)(n_f^2 + 2)]} \qquad (4.17)$$

where f = packing fraction

n_b = bulk refractive index

n_f = thin film refractive index

This factor typically varies between 0.8 and 1.0.

The results of these preliminary experiments clearly indicate how a substrate material can influence the formation of surface GeO_2 thin film layers. Si/Ge systems and their oxidation characteristics are important in the development of new electronic devices.[45-48] However, the use of Si as a substrate for the development of pure GeO_2 optical waveguides by Ge oxidation is definitely questionable. For relatively shallow Ge oxidations, where the oxygen does not "see" the underlying Si wafer, interaction is not very likely to occur. This is achieved through lower peak oxidation temperatures and/or shorter peak holding periods. Figures 4.5 - 4.7 indicate that significant oxide layers do not begin to form until peak temperatures approach 800° C. Figure 4.5 illustrates all of the data listed in Table 4.1. Figure 4.6 provides a curve fit to the data involving the one hour holding time. Figure 4.7 displays the effect of holding time on the resulting oxide thickness for a constant peak temperature (800° C). Results such as these normally provide information on the optimum conditions for waveguide production. As mentioned earlier, control over the waveguide thickness is critical to achieving desired optical characteristics, such as single mode propagation. Although the shapes of the curves in Figures 4.5 - 4.7 are as expected, the actual thickness values are in question due to the error factors discussed earlier.

4.4.2 Oxidized Ge and Thermally Evaporated GeO_2 on Quartz and LTCC

This section evaluates and compares two techniques in the formation of thin film GeO_2 structures. The first technique involves the oxidation of thermally evaporated Ge thin films, while the second technique involves the direct thermal evaporation of GeO_2 thin films. Quartz and fired LTCC will now be used as the substrate materials. LTCC will be tested as a substrate material, since this is the material to be used in the proposed integration technique. The formation of GeO_2 thin films on transparent quartz substrates will allow the use of spectrophotometry techniques to evaluate the optical quality of the films. Based on the results of the previous section, the oxidation tests will be performed at a lower peak temperature of 700° C, in order to minimize any type of diffusion or interaction between the film and the substrate. The ramping rates and the oxygen flow rate will remain the same. One thousand angstroms of Ge is thermally evaporated onto the quartz and LTCC substrates. A peak holding time of 8 hours will be tested first, and then subsequently modified until the entire Ge layer is oxidized. Visual inspection of the samples after oxidation shows that the Ge film has turned from its original metallic color to virtually transparent, suggesting that the Ge layer has fully oxidized. As mentioned, GeO_2 powder is also thermally evaporated onto quartz and fired LTCC substrates, as a comparison technique. Due to an evaporator limitation, only 480 angstroms of the oxide is deposited onto the substrates. These films appear to be slightly darker than those created from the oxidation of the Ge films, possibly due to a low oxygen content in the films, as observed in reference 13.

A scanning spectrophotometer (Section 4.5.2) is used to measure the optical quality of the evaporated GeO_2 films, as well as the oxidized Ge films over a wide wavelength range. This instrument can measure the percent transmittance and percent reflectance for the films, and thus give an estimate of the percent absorptance using Equation 4.18.

$$\%T + \%R + \%A = 100\% \qquad (4.18)$$

The percent transmittance, percent reflectance, and percent absorptance is measured from the quartz samples, while only the percent reflectance can be measured from the LTCC samples (Figures 4.8 - 4.10).

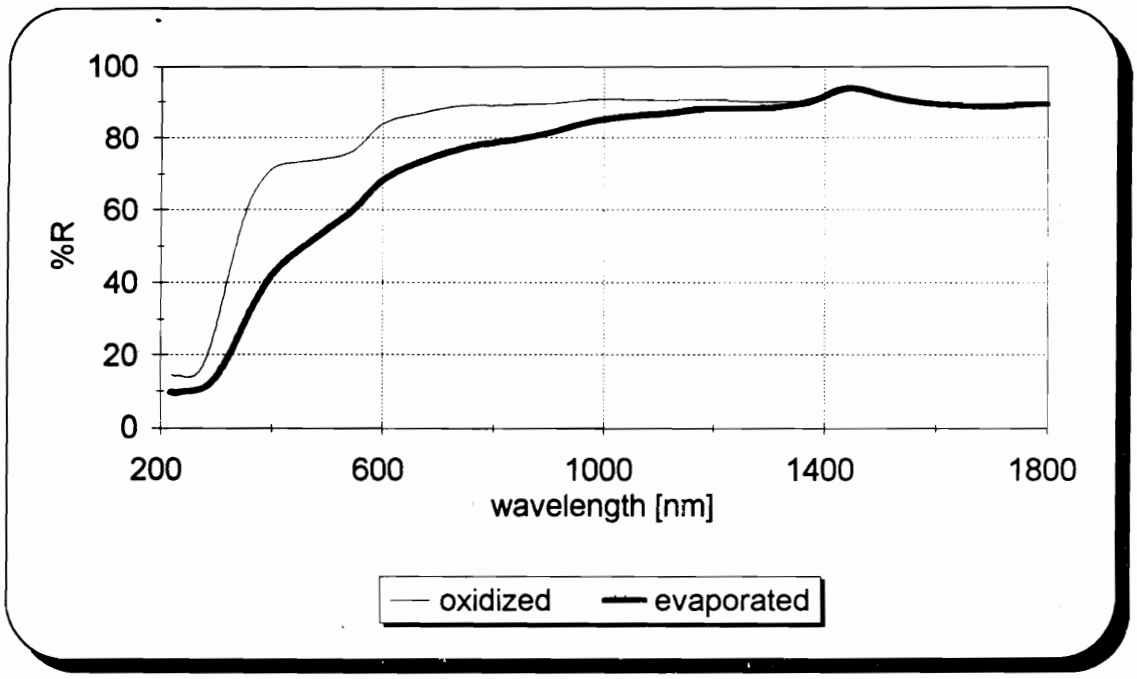

Figure 4.8 - % reflectance for films on LTCC

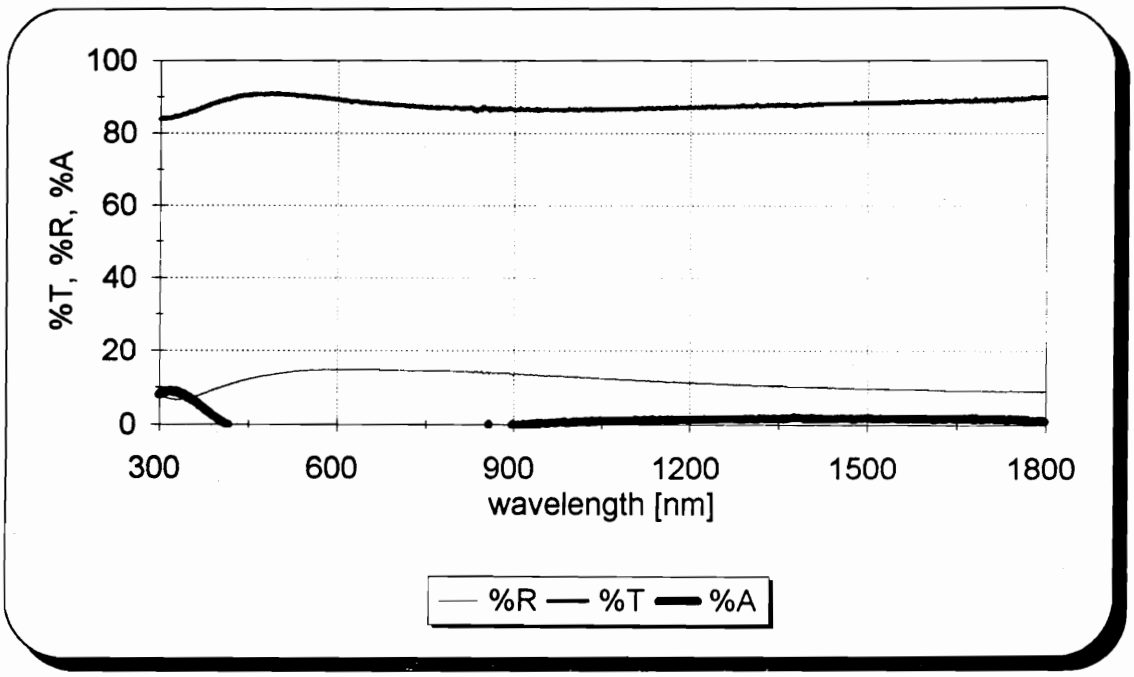

Figure 4.9 - % transmittance, % reflectance, % absorptance for oxidized Ge on quartz

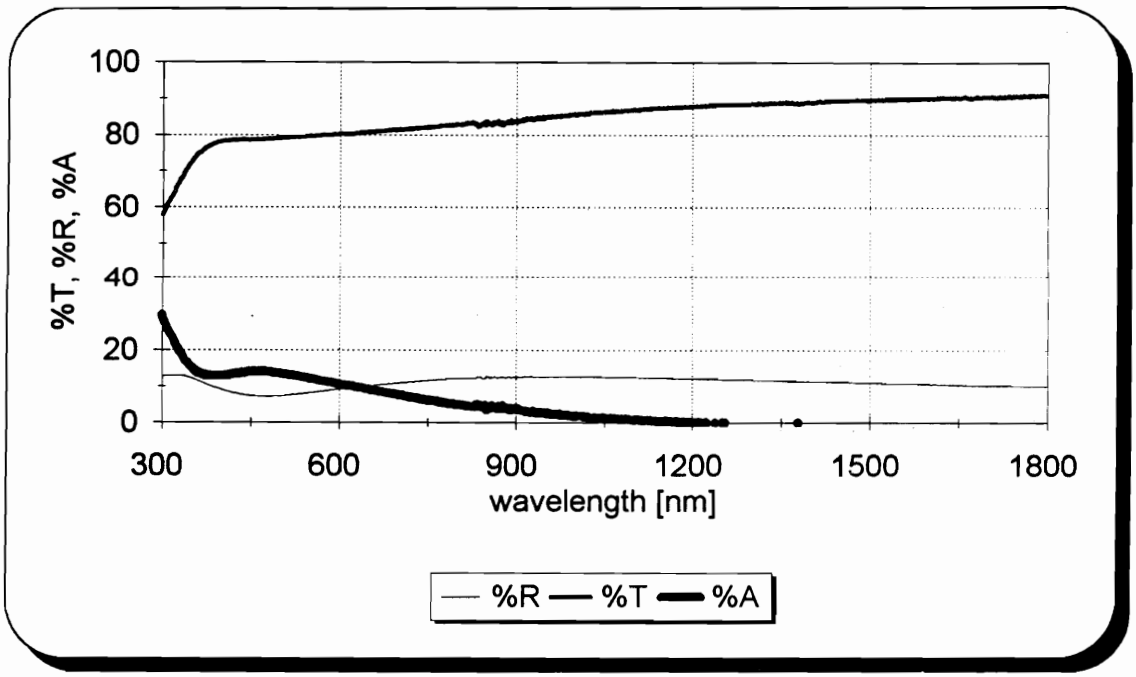

Figure 4.10 - % transmittance, % reflectance, % absorptance for evaporated GeO_2 on quartz

The thermally evaporated GeO_2 films seem to exhibit a higher (up to 20% higher) loss than the oxidized Ge films, especially at the lower wavelengths (300 - 900 nm). Much of this loss may be attributed to low quality deposition, as film quality has been shown to be very sensitive to deposition rates and other conditions, such as atmosphere, substrate temperature, and annealing techniques.[13,50] Deposition by thermal evaporation techniques tends to create films that are columnar in structure, and that possess voids between the columns.[51] As discussed earlier, thin film structures are often described in terms of a packing fraction. The packing fraction describes the difference between the refractive index of the thin film and that of the bulk material due to the significant difference in their densities. The voids within the film also tend to absorb moisture, making the thin film optically unstable, mechanically less durable, and more prone to poor adhesion. Figures 4.11 and 4.12 demonstrate the effect of annealing and deposition rate on the quality of thin film GeO_2 waveguides. Note the significant improvement in waveguide performance that is achieved through the annealing process (Figure 4.11). Annealing is a technique in which the entire system (film and substrate) is exposed to a common elevated temperature. This process allows a "relaxation" of the residual strains developed within the system (such as those created by the solidification of hot gaseous compounds on a relatively cool substrate during thermal evaporation). During the oxidation of the thermally evaporated Ge film, it is possible that some annealing is also taking place at the elevated oxidation temperatures. This may account for the higher film quality observed for the oxidized samples in Figures 4.8 and 4.9, as compared to the evaporated films in Figures 4.8 and 4.10. In addition, the films have been evaporated at a relatively high rate, on the order of several angstroms per second. As shown in Figure 4.12, an increase in the deposition rate results in a severe decline in film quality. This will also contribute to the loss characteristics observed in Figures 4.8 - 4.10.

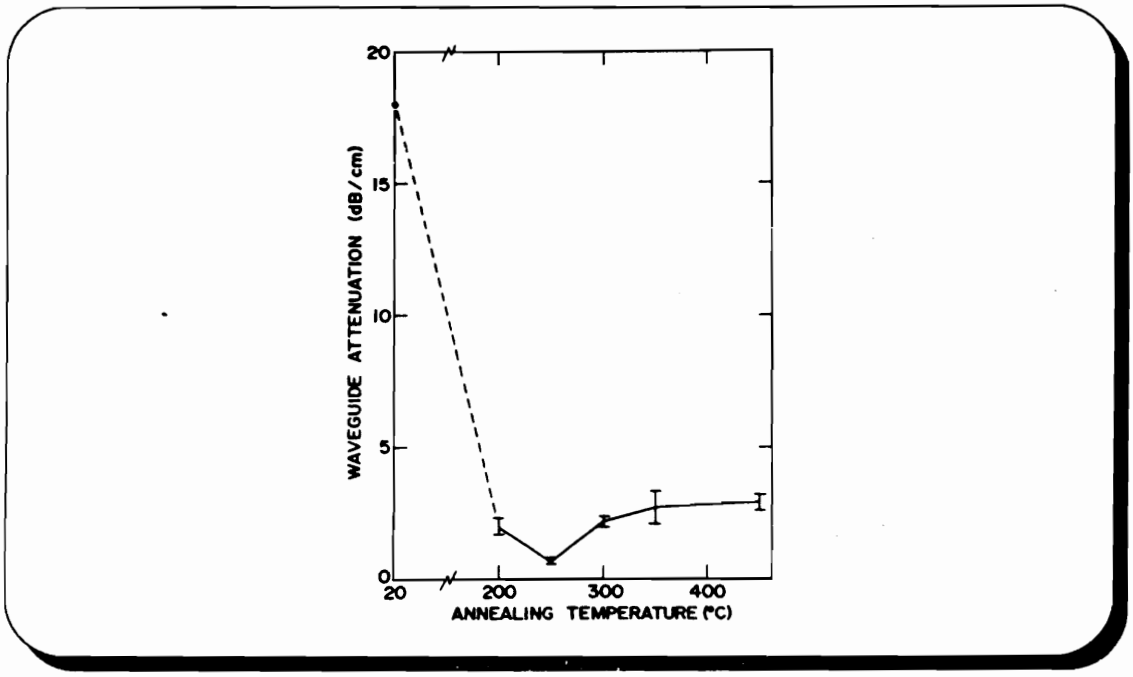

Figure 4.11 - GeO_2 waveguide attenuation vs annealing temperature[13]

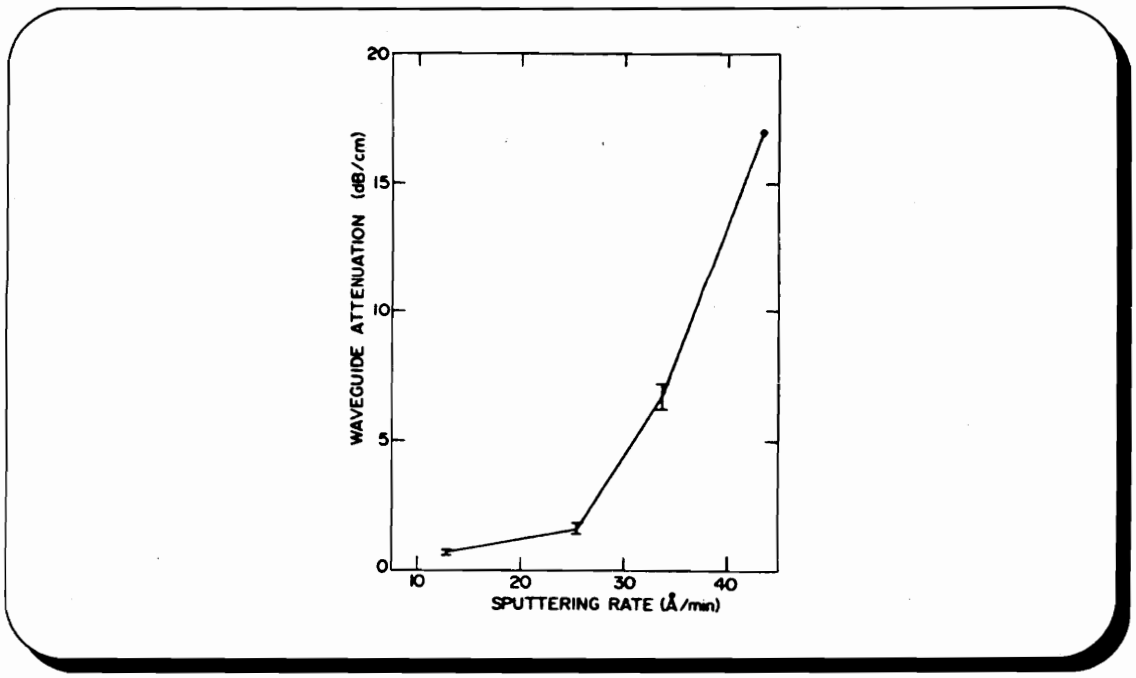

Figure 4.12 - GeO_2 waveguide attenuation vs deposition (sputtering) rate[13]

The increase in loss toward the lower wavelengths may be attributed to Rayleigh scattering, which is proportional to $\frac{1}{\lambda^4}$.[1] The more pronounced loss in the thermally evaporated GeO_2 film at the lower wavelengths is not surprising, as more scattering is expected from a lower quality film. The films on the LTCC substrate also appear to suffer from a slightly higher loss than those on the quartz substrates. This is likely, due to the difference in smoothness between the quartz and the LTCC surfaces. Scattering from the rough surface of a waveguide substrate will degrade waveguide performance, regardless of the quality of the film material. In general, materials in the form of thin films tend to have higher loss characteristics than those in the bulk form, due again to deposition conditions.[49] Thus the relatively low loss results shown in Figures 4.9 and 4.10 (at wavelengths > 900 nm) may provide the waveguide designer with a false sense of security. A high degree of transparency for a very thin (1000 angstroms) film does not imply that a long (several centimeters) waveguide of the same material will exhibit the same low loss characteristics.

These results have compared two techniques in the formation of thin film GeO_2 - direct thermal evaporation of GeO_2, and post-oxidation of thermally evaporated Ge. The characteristics of the two films appear similar, however, the post-oxidation technique may have a slight advantage due to its inherent annealing feature. It is important to note that the spectrophotometry results shown in Figures 4.9 and 4.10 do not separate out any effect of the substrate material (in this case, quartz) on the overall absorptance of the structure. The important information that should be taken from these measurements is not a quantitative evaluation of the loss, but instead, a comparison of the two techniques. Since the substrates used for both techniques are the same, the difference in the absorptance curves of Figures 4.9 and 4.10 is due to different film characteristics and not the substrate material. Films deposited by thermal evaporation, however, have a maximum thickness of only a few microns. This is due primarily to adhesion problems that develop as the film thickness increases. Thus, if thicker waveguide structures are desired, an alternative technique such as thick film processing must be investigated.

4.4.3 Thick Film GeO_2 Paste

4.4.3.1 Paste Formulation and Processing

The thin film structures evaluated in the previous section are not very efficient in coupling directly to optical fibers or relatively large packaged devices (as used in the proposed integration technique of Chapter 5), without the use of external lenses and mirrors. As mentioned earlier, thicker structures formed by conventional thin film techniques are unreliable due to problems such as poor adhesion. This is the incentive behind the development of a thick film GeO_2 optical paste that may be more compatible with the proposed optoelectronic packaging technique.

The development of a thick film GeO_2 paste begins with weighing out the appropriate amounts of primary and secondary materials. The primary material is the GeO_2, while the secondary ingredients consist of glass and binder materials. These materials are then placed in a small mill jar that is half-filled with milling balls. A small amount of ethyl alcohol is added to the jar to facilitate removal of the materials after milling. After a 12 - 15 hour milling process, the material is strained into a large beaker, using additional ethyl alcohol to wash the milling balls. The liquid is heated at 100° C under a fume hood to evaporate off all of the ethyl alcohol. The dried material is then removed from the beaker and crushed back into powder form using a mortar and pestle. The powder is placed in a small beaker where alpha terpineol (a volatile solvent) is added in small increments to create a paste. Once the paste reaches the desired viscosity, it is stirred well to ensure a homogeneous mixture. From this point on, the paste is processed in the same manner as traditional thick film pastes. The paste is squeegeed through a wire mesh screen onto a substrate. The print is allowed to settle for 10 minutes to remove any mesh patterns from the print, and then dried at 150° C for 10 minutes to burn off the volatile solvent. A subsequent firing profile then burns off the remaining binder material before ultimately fusing the GeO_2 and glass materials to each other and to the substrate.

Optimization of the thick film paste, however, requires many modifications to the material compositions and processing techniques mentioned above. Early experiments, for

example, utilized unmilled powders, no glass additives, and simple stencils instead of a wire mesh screen. Using the melting point of GeO_2 (~ 1100° C) as a starting point, various firing profiles were tested in an attempt to find the optimum sintering conditions of the film. Peak firing temperatures between 850° C and 1050° C were investigated with peak holding times between 10 and 45 minutes. The results of these experiments, however, suffered from poor adhesion to the substrate, minimal sintering of the GeO_2, and inhomogeneity of GeO_2 material within the print. Based on these results, the paste composition and processing techniques are modified as follows. First, a low temperature glass powder is added to the composition to promote sintering and adhesion. Second, all of the powders are milled prior to creating the paste, in order to reduce the particle size. This will allow the use of traditional wire mesh screens and improve the homogeneity of the print. The composition of the primary and secondary materials for the paste, by weight percent, is listed as follows:

90% GeO_2 powder (-200 mesh)
5% Bismuth-zinc-borate (Bi-Zn-B) glass powder
5% Ethylcellulose binder

4.4.3.2 Results

The new paste is first tested on an alumina substrate using a 250 mesh screen and the standard thick film firing profile shown in Figure 4.13 (850° C/10 min. peak). The resulting film is a homogeneous white color, and exhibits very good adhesion. However, the ESEM photograph in Figure 4.14 shows large voids on the order of 5 - 10 um. This indicates that the film suffers from poor densification, requiring a higher processing temperature and longer peak holding time in order to properly "fuse" the particles of GeO_2 in the film. Another sample is processed at a peak temperature of 1100° C with a peak holding time of two hours (ramping rates unchanged). In this case, the resulting film is more transparent than the first, indicating better densification. However, a slight yellow

tint suggests the film is not yet fully optimized. When the peak firing temperature is increased to 1200° C, the film becomes smoother and loses the yellow coloration. The ESEM photograph in Figure 4.15 shows the improved densification (no voids, complete fusion of GeO_2 particles) and homogeneity of the film, as well as the apparent development of some type of crystal structure, of the order of 2 um.

In order to determine the optical characteristics of the film, a scanning spectrophotometer will be used to measure the percent transmittance and percent reflectance over a wavelength range. A transparent substrate able to withstand a 1200° C processing temperature is necessary to perform the percent transmittance measurement. The film is therefore printed on part of a polished sapphire disk. The other portion of the disk will be used to characterize the sapphire, alone, in order to isolate the film characteristics from the sapphire characteristics. After processing on a transparent substrate, a white cloudiness of the film is observed that was not visible on the alumina substrate. This may be due to some crystallization within the film, as noted in the ESEM photograph in Figure 4.15.

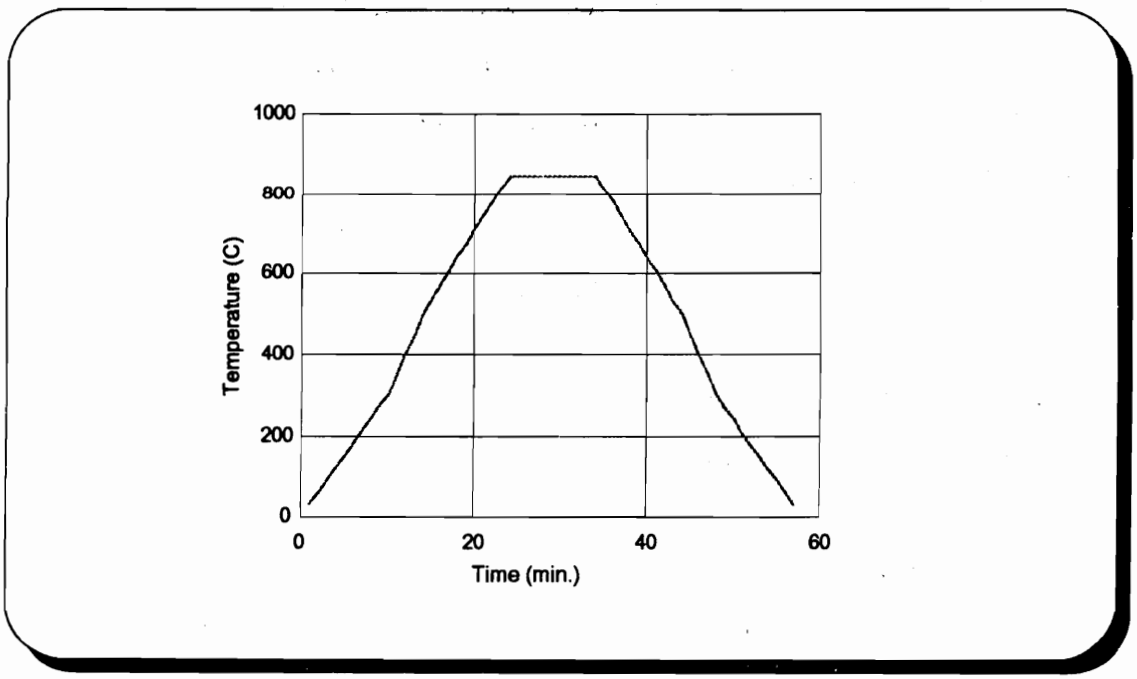

Figure 4.13 - Standard thick film firing profile

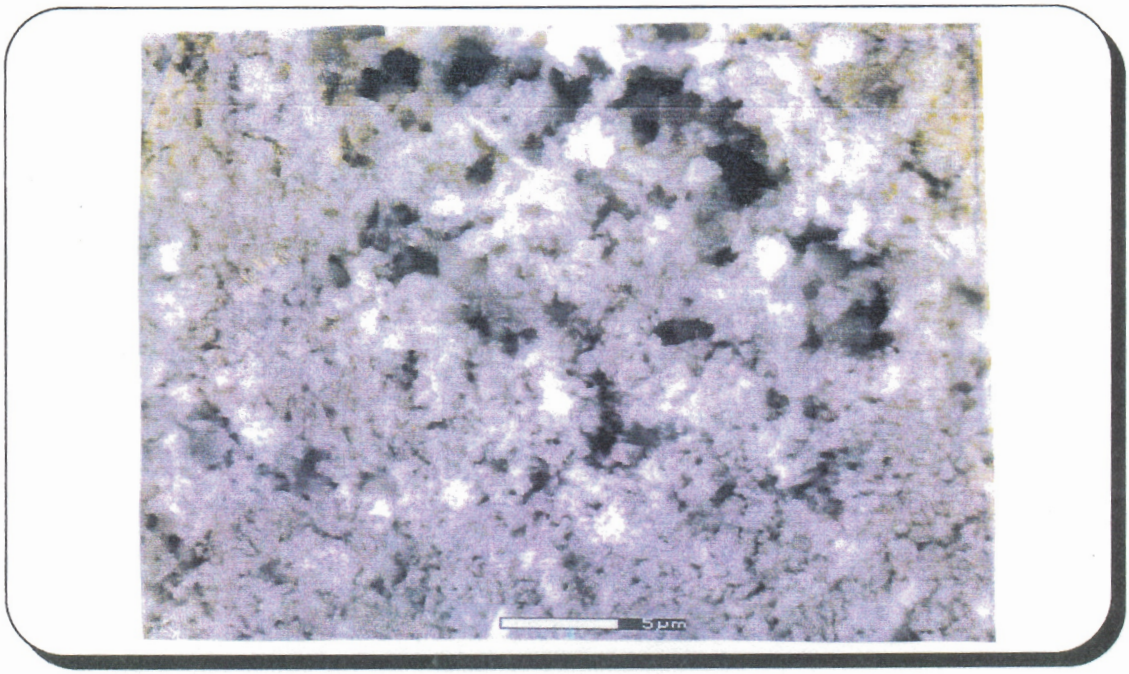

Figure 4.14 - ESEM photograph of thick film (850° C)

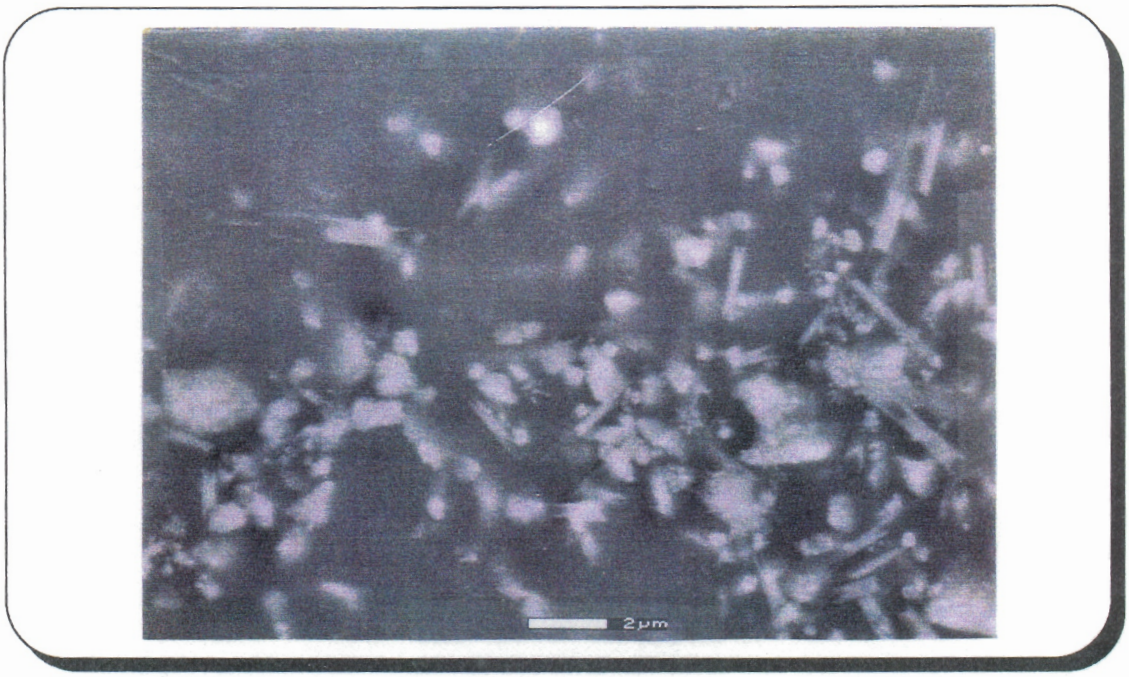

Figure 4.15 - ESEM photograph of thick film (1200° C)

Percent transmittance and percent reflectance measurements are performed on both the coated and uncoated regions of the sapphire disk. The percent transmittance and the percent reflectance data for the uncoated region are added together. From Equation 4.18, the remaining percentage of light represents the percent absorptance of the sapphire substrate. Similarly, the percent transmittance and percent reflectance data for the coated region are added together. Again, the remaining percentage of light represents the percent absorbed by the film and the sapphire substrate. Subtracting away the absorptance of the sapphire substrate, obtained earlier, therefore provides an estimate of the absorptance of the film, alone. This technique gives a good estimate of the film absorptance as long as the difference between the refractive indices of the film and sapphire remains relatively small. Otherwise, large reflections will occur at the film-sapphire interface. This will cause the light to make multiple passes through the film, and thus distort the percent absorptance estimate.

The results of these spectrophotometry measurements, shown in Figure 4.16, indicate a relatively high loss estimate for the film, on the order of 15 - 20%. It should be noted that the percent transmittance measurements are performed with a different calibration than the percent reflectance measurements (due to the need for a different calibration "standard" in each measurement technique). Specifically, in order to measure percent reflectance, the equipment must first be calibrated by placing a high-reflectance disk into the sample holder to set the 100% reflectance level. In order to measure percent transmittance, a separate calibration is performed that uses an empty sample holder to set the 100% transmittance level. The addition of results that have been obtained from different calibration techniques introduces error into the final sum. This is the reason why the sum of the percent transmittance and percent reflectance for the sapphire exceeds 100%. Nevertheless, the coated and uncoated regions are still measured using the same percent transmittance calibration and the same percent reflectance calibration. Thus, the relative difference between the percent absorptances of the coated and uncoated regions remains a good estimate of the absorptance of the film.

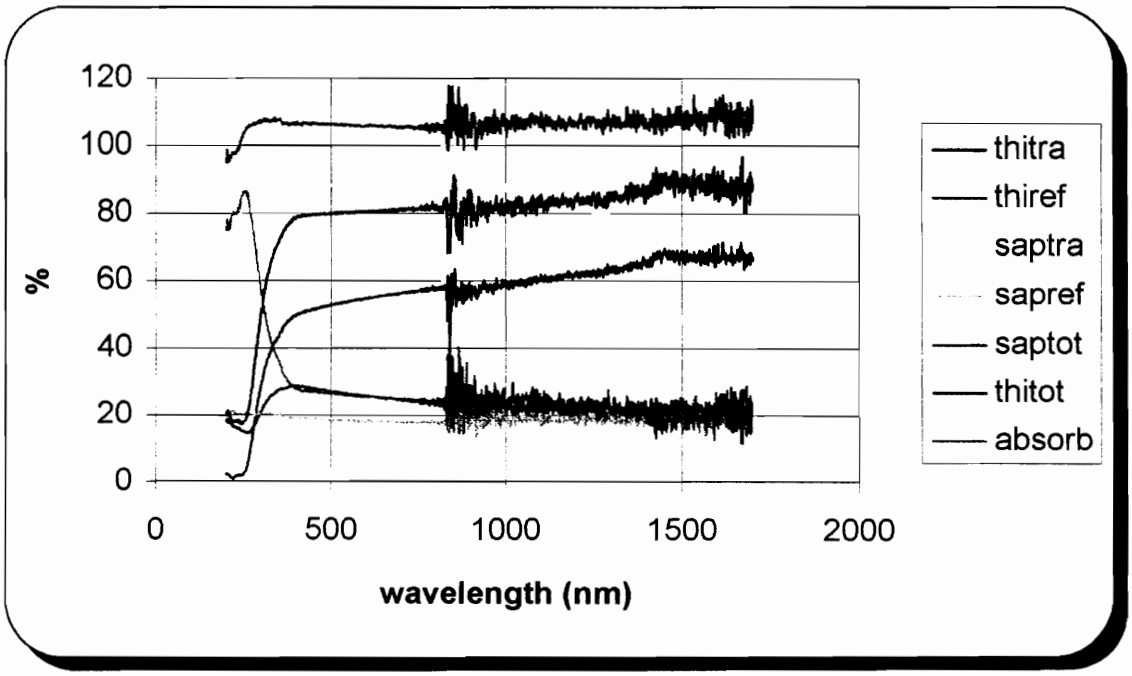

Figure 4.16 - Spectrophotometry results for thick film on sapphire

Note:

thitra = transmittance of the thick film on sapphire

thiref = reflectance of the thick film on sapphire

saptra = transmittance of the sapphire

sapref = reflectance of the sapphire

saptot = saptra + sapref (= 100% - absorptance of the sapphire)

thitot = thitra + thiref (= 100% - absorptance of the thick film on sapphire)

absorb = saptot - thitot (estimate of the absorptance of the film, alone)

Five additional thick film pastes are produced, with different compositions, in order to investigate the effect of composition on the refractive index of the resulting film. The compositions of all of the pastes are listed in Table 4.2. Control over the refractive index value is important in the design of waveguide cores for specific applications. However, the ability to modify the paste composition in order to produce lower refractive

index cladding regions is equally important. In some cases, the substrate material doubles as cladding for a deposited waveguide core. However, the ability to develop specialized cladding materials has several advantages. First, additional design flexibility is gained, since the cladding characteristics are not restricted to those of the substrate material, and no limitations are placed on the core region. Second, a separate cladding layer isolates the waveguide core from undesirable substrate characteristics such as surface roughness, which can produce additional scattering losses.

Table 4.2 - Thick film paste compositions

Paste #	Glass additive	GeO_2 (wt. %)	Glass (wt. %)	Ethylcellulose (wt. %)
0	Bi-Zn-B	90	5	5
1	Bi-Zn-B	75	20	5
2	Bi-Zn-B	60	35	5
3	SiO_2	90	5	5
4	SiO_2	75	20	5
5	SiO_2	60	35	5

Due to some difficulty in printing some of the pastes through the 250 mesh screen, a plain (unemulsified) 80 mesh screen is substituted. Although this will increase the surface roughness of the resulting film, it will ensure that a representative composition of the paste is being deposited on the substrate (and not stuck in the screen mesh). Ultimately, the increased surface roughness will not be a factor anyway, since the films must be polished in preparation for ellipsometry measurements. All of the pastes are settled, dried at 150° C for 10 minutes, and then fired using the 1200° C/2 hour peak profile. The films are then polished to minimize surface roughness, and allow ellipsometry measurements to be performed in order to determine the indices of refraction.

In 1836, Cauchy developed an expression to represent the change in the refractive index of a material with wavelength (Equation 4.19).[52] This Cauchy model is used to fit the experimental ellipsometry data.

$$n(\lambda) = A + \frac{B}{\lambda^2} + \frac{C}{\lambda^4} \quad (4.19)$$

where A, B, and C are positive constants that depend on the material

Due to their relatively large thicknesses, the films are best modeled as bulk materials, rather than thin films on substrates. An example of the ellipsometry data and modeling technique is shown in Figure 4.17. As discussed in Section 4.5.2, ellipsometry uses changes in the polarization of light, such as that caused by reflection from a surface film, to determine the index of refraction. Figure 4.17 illustrates the experimental data and the "model fit" that are obtained for one of the films. These results show ψ (a measure of the polarization change) under three separate measurement conditions (angles of incident light = 70°, 75°, and 80°). Figures 4.18 and 4.19 illustrate the results of the modeling techniques. Figure 4.18 shows the refractive index versus wavelength for each of the six compositions. Figure 4.19 graphs the refractive indices versus the glass composition by weight percent.

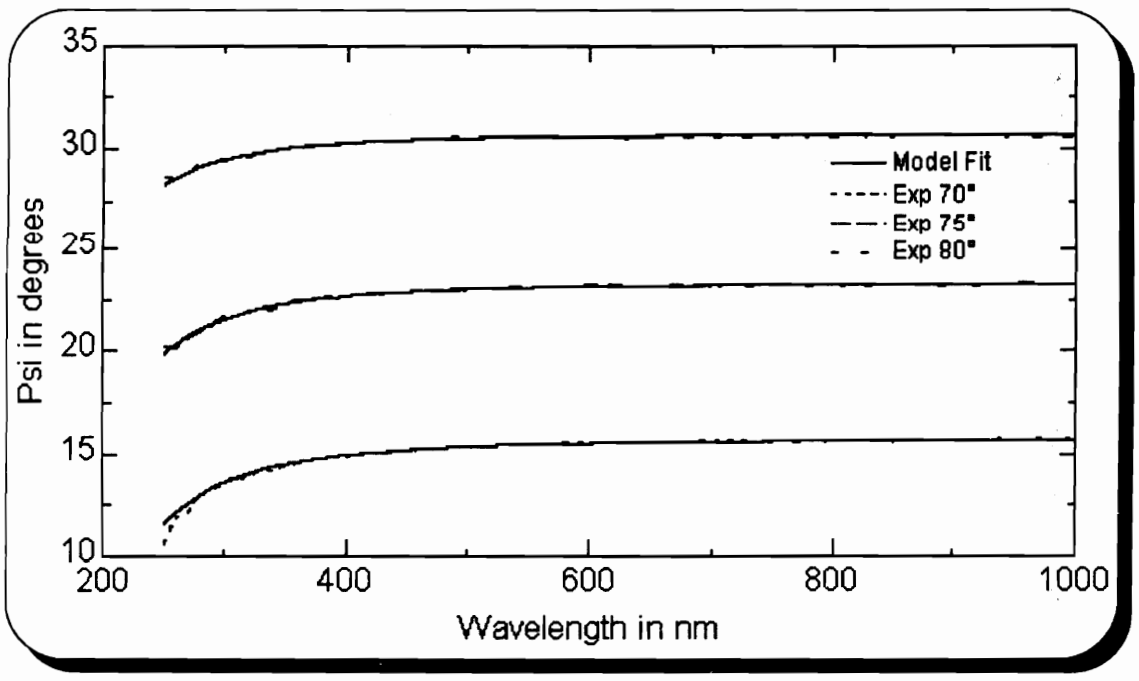

Figure 4.17 - Example of ellipsometry data and modeling

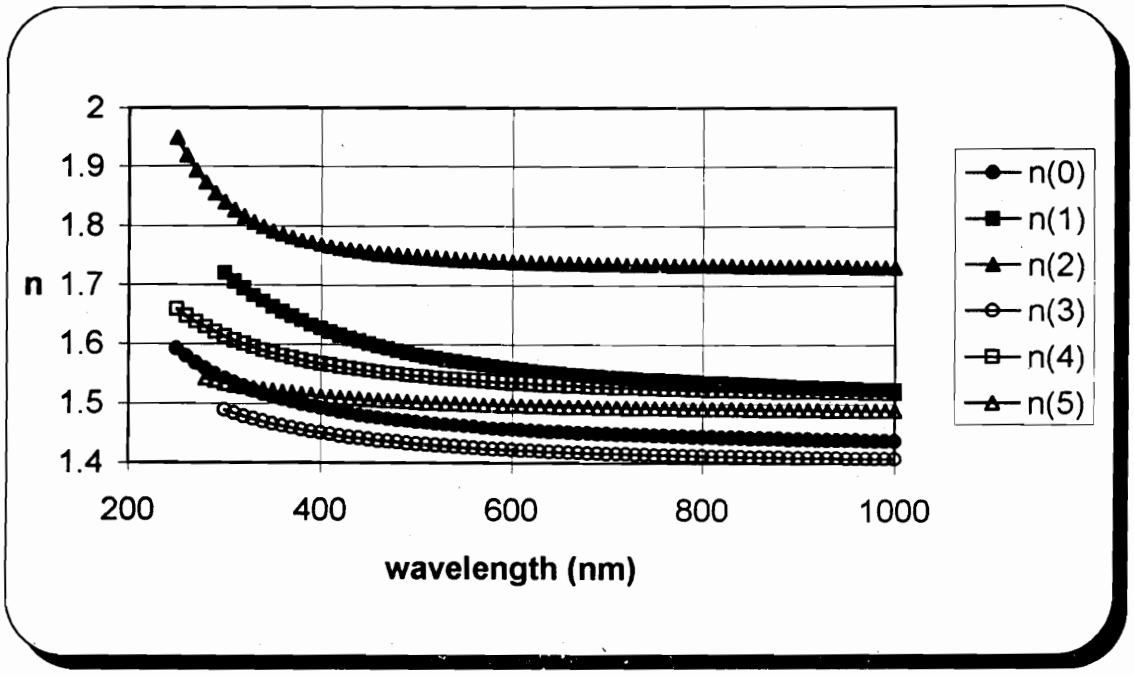

Figure 4.18 - Index of refraction of different paste compositions

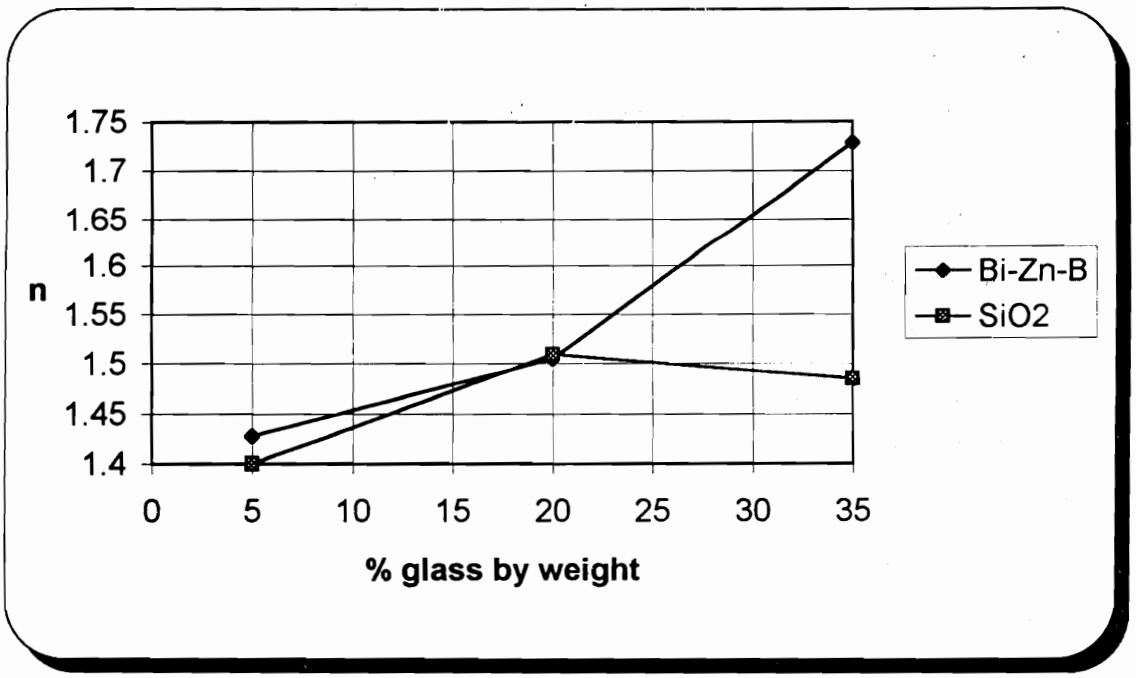

Figure 4.19 - Change of refractive index with glass addition

These results indicate a clear dependence of the refractive index on the glass composition of the paste. An explanation and clear understanding of these results, however, is much more involved. As noted earlier, the form of a material (i.e. thin film or bulk) has a significant impact on its optical properties. Similarly, the optical characteristics of a material in thick film form are expected to differ from those of the same material in either thin film or bulk form. This situation is further complicated by the glass additives used in thick film paste compositions. These additives have their own optical characteristics which will influence the overall optical properties of the thick film. Although no comparison data is available for thick film GeO_2 compositions, published results on glassy GeO_2 materials and oxides used in glass additives will assist in analyzing the results of this work.

As shown in Table 4.2, two types of glass additives are investigated in this research work - Bi-Zn-B and SiO_2. The Bi-Zn-B glass is composed of < 45% Bi_2O_3 (bismuth oxide), < 35% ZnO (zinc oxide), and < 35% B_2O_3 (boron oxide). The addition of increasing amounts of Bi_2O_3 has been shown to cause a drastic increase in the refractive index of the overall system.[53] Glassy GeO_2 has a refractive index of approximately 1.61. However, through the addition of Bi_2O_3, the refractive index of the system rapidly increases to values greater than 2.0. ZnO, as mentioned in Section 4.3.1, is a useful optical material on its own. The refractive index of ZnO is also relatively high - approximately 2.0.[33] B_2O_3 is the only constituent of this glass additive that possesses a relatively low index of refraction - approximately 1.46.[53] One may expect that the paste consisting of 90% GeO_2 by weight, and 5% Bi-Zn-B by weight (Paste #0) will produce a film with an index of refraction very similar to that of glassy GeO_2. However, one can see from Figures 4.18 and 4.19 that this is not the case. The refractive index value of this film, as determined by ellipsometry techniques, is approximately 1.43 - significantly lower than the 1.61 value for glassy GeO_2. When the Bi-Zn-B additive content of the paste is increased to 20% by weight (Paste #1), the refractive index of the resulting film increases to approximately 1.50. This increase may be attributed to a greater concentration of

higher refractive index additives (Bi_2O_3 and ZnO). The Bi-Zn-B additive content in the paste is then further increased to 35% by weight (Paste #2). This composition change causes a drastic increase in the refractive index of the resulting film to approximately 1.73. This relatively high refractive index value is more indicative of the high refractive index constituents of the glass additive.

As mentioned, SiO_2 is also used as the glass additive in the GeO_2 paste composition. This is contrary to the more popular notion of using GeO_2 as a dopant in SiO_2 glasses. Unlike the Bi-Zn-B additive, SiO_2 possesses a relatively low refractive index of approximately 1.46. A paste is developed consisting of 90% GeO_2 by weight, and 5% SiO_2 by weight (Paste #3). Ellipsometry measurements of the resulting film provide a refractive index value of approximately 1.40. This is similar to the value produced by Paste #0 (90 wt. % GeO_2 / 5 wt. % Bi-Zn-B) of 1.43. Again, this value varies significantly from the refractive index value of 1.61 for glassy GeO_2. The SiO_2 content in the paste is then increased to 20% by weight (Paste #4). The resulting film possesses a higher refractive index of approximately 1.51. This value is interesting, since it is higher than that of both the SiO_2 and the experimental 90 wt. % GeO_2 thick films, but lower than that of glassy GeO_2. This result is therefore more consistent with published results for glassy GeO_2/SiO_2 systems having refractive indices between 1.46 and 1.61.[53] Finally, the SiO_2 content in the paste is increased to 35% by weight (Paste #5). The resulting film has a refractive index of approximately 1.48. This value is very similar to that observed in pure SiO_2 films.

The above analysis of the experimental data is based on the optical characteristics of the individual paste components. This assumes that there are no chemical reactions occurring between paste components. In other words, the GeO_2 and the oxides which comprise the glass additives maintain their structure and their associated optical features. Although this is true for some systems, other systems may undergo a compositional rearrangement in which new chemical compounds are formed. These new compounds may possess optical properties that vary significantly from those of the original

constituents of the compound. Whether or not a composition experiences such a rearrangement depends on the materials, the concentrations of the materials, as well as the processing conditions involved. One must consider this possibility of creating new compounds when analyzing the refractive index data presented above.

As we have seen, the formation of quality optical thick films is a complicated process that is heavily dependent on processing conditions and paste composition. Pure melted GeO_2, for example, forms a nice transparent glass if cooled rapidly. Otherwise, it devitrifies into an opaque white glass.[41] In addition, upon exposure to atmospheric moisture, pure GeO_2 glass is prone to surface devitrification.[54] The crystals noted in the ESEM photograph (Figure 4.15) may be the onset of some devitrification. It is also known that not all compositions may be formed into glasses without devitrification. Some successful glass compositions include flux materials such as Na_2O (sodium oxide) and CaO (calcium oxide or lime) which reduce the melting temperature of the composition. The substitution of K_2O (potassium oxide or potash) for Na_2O will reduce the tendency of the glass to devitrify. Al_2O_3 (aluminum oxide or alumina) or B_2O_3 (boron oxide) is often added to lower the thermal coefficient of expansion, an important factor in minimizing the strain between the film and the substrate. In addition to producing scattering losses, such strains in the thick film have also been known to cause a homogeneous, isotropic glass to become birefringent, such that its optical properties now vary in different directions inside the film.[41,55]

4.4.4 Waveguide Fabrication

Using the information presented in Table 4.2 and Figure 4.18, a waveguide with the structure shown in Figure 4.20 may be developed.

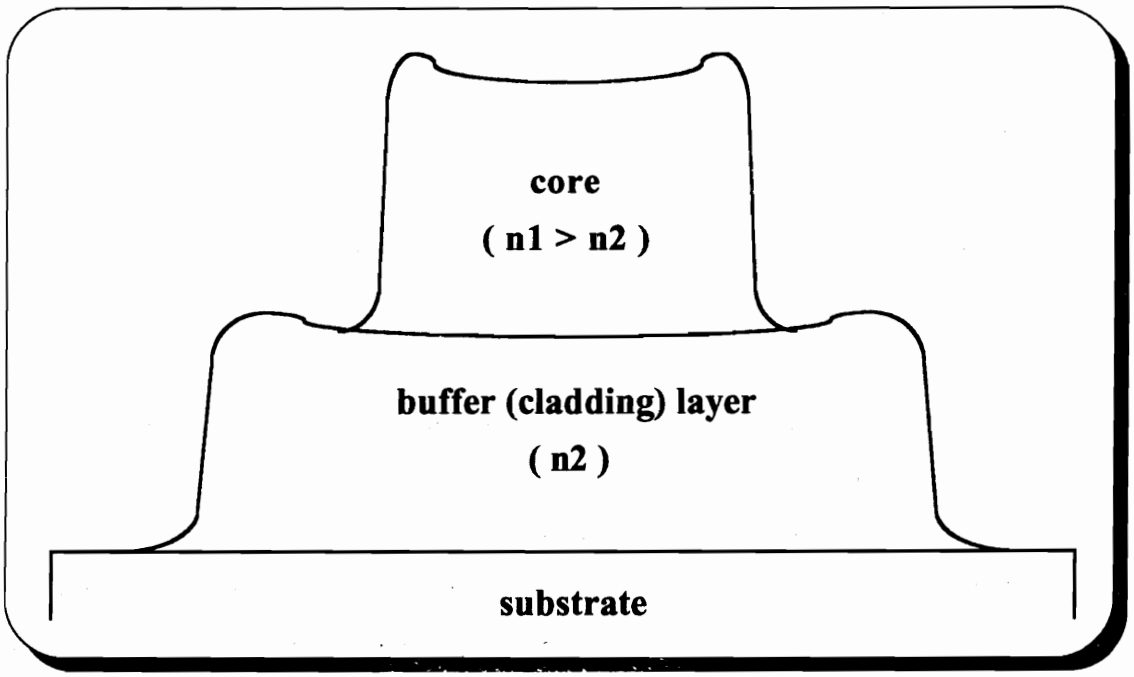

Figure 4.20 - Thick film optical waveguide

The first step in the fabrication of the thick film optical waveguide structure is the creation of the buffer/cladding layer. As discussed earlier, this layer isolates the waveguide core from the alumina substrate, and also serves as the waveguide cladding. As the cladding region, this layer must be formed from a paste that produces a film with a lower refractive index than the waveguide core. Paste #0 ($n \sim 1.43$) is therefore selected for use in forming the buffer/cladding layer. A large area pattern is screen-printed onto an alumina substrate. The print is then settled, dried, and fired using the 1200° C/2 hour peak profile.

A higher index paste is then selected for use in defining the waveguide core region. Paste #2, with a refractive index of approximately 1.73, will be used for this purpose. A small strip is screen-printed on top of the fired buffer/cladding layer. Again, the print is settled, dried, and fired using the 1200° C/2 hour peak profile. The fired waveguide core strip is approximately 100 mil wide, 750 mil long, and 10 um thick. At the edge of the

substrate, however, the ends of the waveguide core strip tend to taper to thicknesses less than 10 um.

These waveguide dimensions have not been selected to achieve a specific modal characteristic, but rather to demonstrate the development and processing of a generic thick film waveguide structure. The design of a thick film optical waveguide for a particular application may proceed, as follows. First, if the waveguide is to be used in coupling to an optical fiber, then the analysis presented in the Appendix is quite useful. This analysis involves an evaluation of the coupling efficiency between an optical fiber and a rectangular waveguide. Note that these results indicate that a better coupling efficiency is achieved with a square waveguide, as opposed to a rectangular waveguide. In addition, this analysis (based on the effective index method) provides the waveguide designer with the optimum waveguide dimensions for a given set of operating conditions (wavelength, indices of refraction, fiber dimensions). In general, however, the design of a thick film waveguide may be approached in two ways. If the waveguide is "slab-like" (i.e. its width is much greater than its thickness), then the designer may use Equation 4.16 to estimate the waveguide thickness for single mode propagation, given a particular operating wavelength and refractive index values. If the waveguide is rectangular (or square), the waveguide design again begins with the effective index method. Note that the thick film waveguide structure of Figure 4.20 has a different cladding above (air) and below (buffer layer) the core region. As demonstrated in the Appendix, these boundary conditions lead to the determination of various characteristic equations, through the use of the effective index method. Due to their tangential nature, these equations have an infinite number of solutions, each corresponding to a particular "mode" of the waveguide. For a certain combination of wavelength, waveguide dimensions, and refractive index values, a given mode will cease to propagate. This is referred to as the "cut-off" condition. When all of the modes are cut-off except for one, single mode propagation is achieved. Thus, use of the effective index method allows the waveguide designer to determine the proper waveguide characteristics to achieve single mode propagation at a given wavelength.

However, the thick film waveguide structure is often limited to multimode applications, since its thickness is generally too large to achieve single mode operation. Although the modal characteristics of the waveguide are primarily determined by the dimensions of the core region, the thickness of the cladding is also an important factor. As shown in the Appendix, guided modes within the core exhibit electromagnetic fields which decay exponentially in the cladding. Therefore, the cladding must be sufficiently thick, so that the decaying fields are negligible at the outer cladding boundary.

An alternative technique in the development of the thick film optical waveguide structure is also investigated. This technique utilizes a single firing (cofiring) stage, as opposed to the multiple firing method discussed earlier. This technique skips the firing cycle between the drying of the buffer/cladding layer and the printing of the waveguide core strip. Then, once the waveguide core has been dried, a single firing profile (1200° C/2 hour peak) is used to cofire the entire structure. A comparison of these two techniques indicates better core definition using the cofiring method. Multiple firings, on the other hand, appear to cause more blending of the core and cladding regions. Regardless of the firing technique, however, crystalline structures are still noticeable, under magnification, in both the core and cladding materials. In addition, some interaction is also likely at the interface between the buffer and core regions due to their equivalent firing conditions. Thus, this interface layer beneath the core may have characteristics which are a combination of the two separate regions. This may be more comparable to a gradient index waveguide, instead of a step index waveguide.

Three different techniques have been attempted to characterize the attenuation of the thick film waveguide structure. The first technique involves the use of optical fibers to couple light into and out of the planar thick film waveguide structure. This procedure is illustrated in Figure 4.21. Note that this technique is a variation on the popular cut-back technique,[10,17,40] where waveguides of varying lengths are evaluated with this type of set-up to obtain a plot of transmitted signal amplitude versus waveguide length. The slope of this plot, therefore, provides an estimate of the attenuation of the waveguide structure.

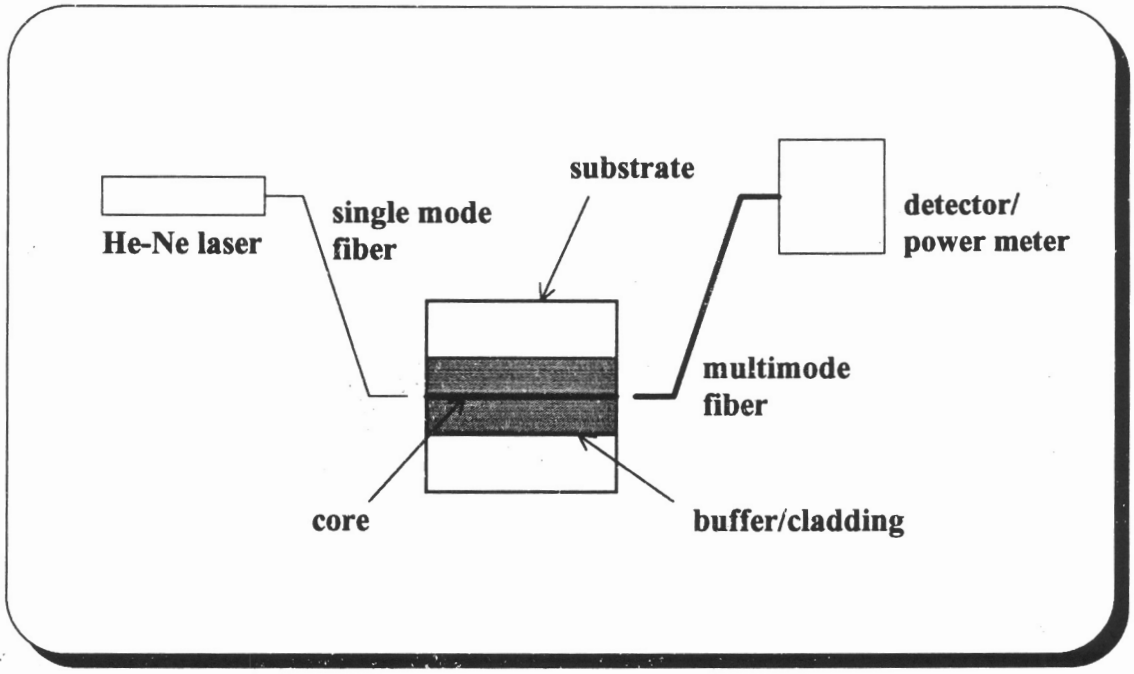

Figure 4.21 - Fiber coupling technique

The advantages of this technique lie in the simplicity of its design. First, light from a He-Ne laser (633 nm) is coupled into a 3.8 um single mode fiber. Micropositioning equipment is then used to direct the light from the end of the fiber into the end of the planar waveguide. A large core multimode fiber is used to couple light out of the other end of the waveguide, and into a photodetector for power transmission measurements. The waveguide structure is then removed from the set-up, and the single mode fiber is coupled directly to the multimode fiber. The difference between the amount of power transmitted through the system, with and without the waveguide structure in place, is a measure of the attenuation of the waveguide. Due to coupling losses at the ends of the waveguide structure, this technique is prone to errors. This is especially true for low loss waveguides where the coupling loss is greater than the attenuation of the waveguide. Although this situation is not expected for this thick film waveguide structure, other difficulties have been experienced. First, there is an inability to accurately couple light from the single mode fiber into the waveguide end face. Second, any light incident on the

waveguide end face is quickly scattered due to the crystalline features within the film. Even after polishing the waveguide end faces, significant bulk and surface scattering prevent this technique from providing any attenuation data on the waveguide structure.

The second technique involves the use of optical prisms to couple light into and out of the top surface of the waveguide structure.[13,40] This procedure is illustrated in Figure 4.22.

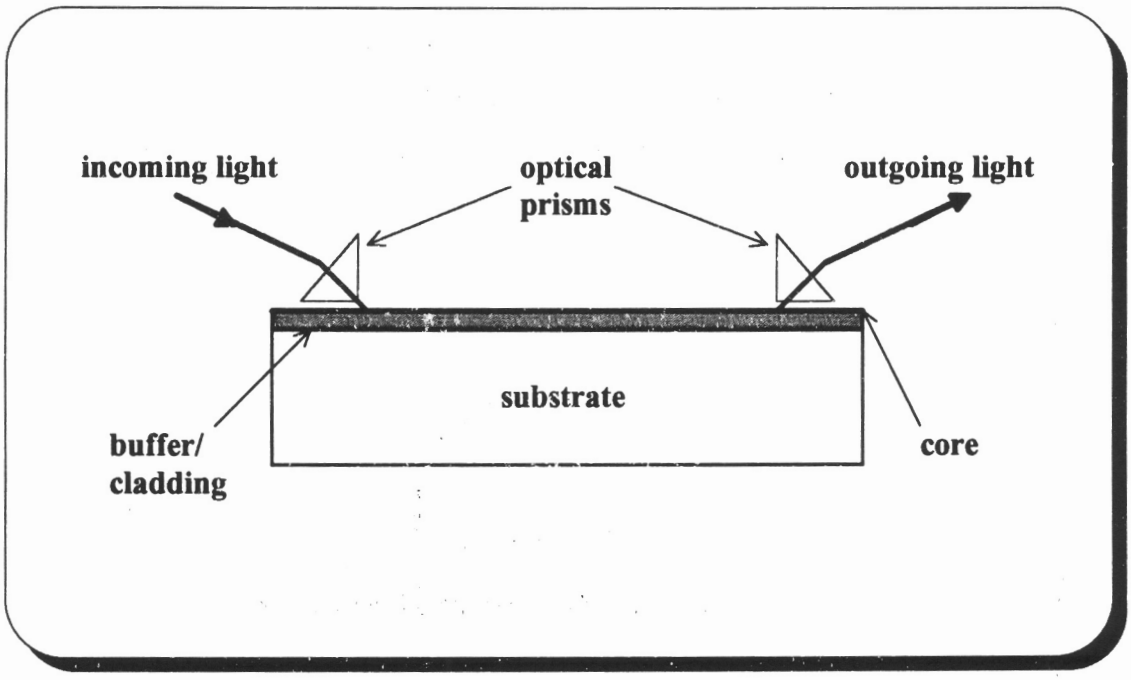

Figure 4.22 - Prism coupling technique

The realization of this technique is somewhat more difficult than the first due to the increased complexity of the set-up. However, the concept is fairly straightforward. Light from a He-Ne laser is directed into an optical prism on the top surface of the waveguide. The light refracts such that it is properly coupled into the planar waveguide. At a given distance along the length of the waveguide, a second optical prism is used to couple light back out of the waveguide top surface, and into a photodetector/power meter. Measurements are repeated at different prism separation distances. The slope of the

transmitted power versus prism separation distance provides a measure of the attenuation of the waveguide. This technique is very popular in measuring the attenuation of relatively smooth thin film structures. However, difficulties in measuring the thick film waveguide structure arise from its increased surface roughness characteristic. Index matching liquids are often used between the prisms and the surface of the waveguide to enhance the coupling of light in and out of the waveguide. Nevertheless, (despite the use of these index matching liquids) significant scattering of light from the waveguide again prevents this technique from providing any attenuation data on the thick film waveguide structure.

The third technique involves the measurement of the scattered light intensity along the length of the waveguide structure.[20,40] This procedure is illustrated in Figure 4.23.

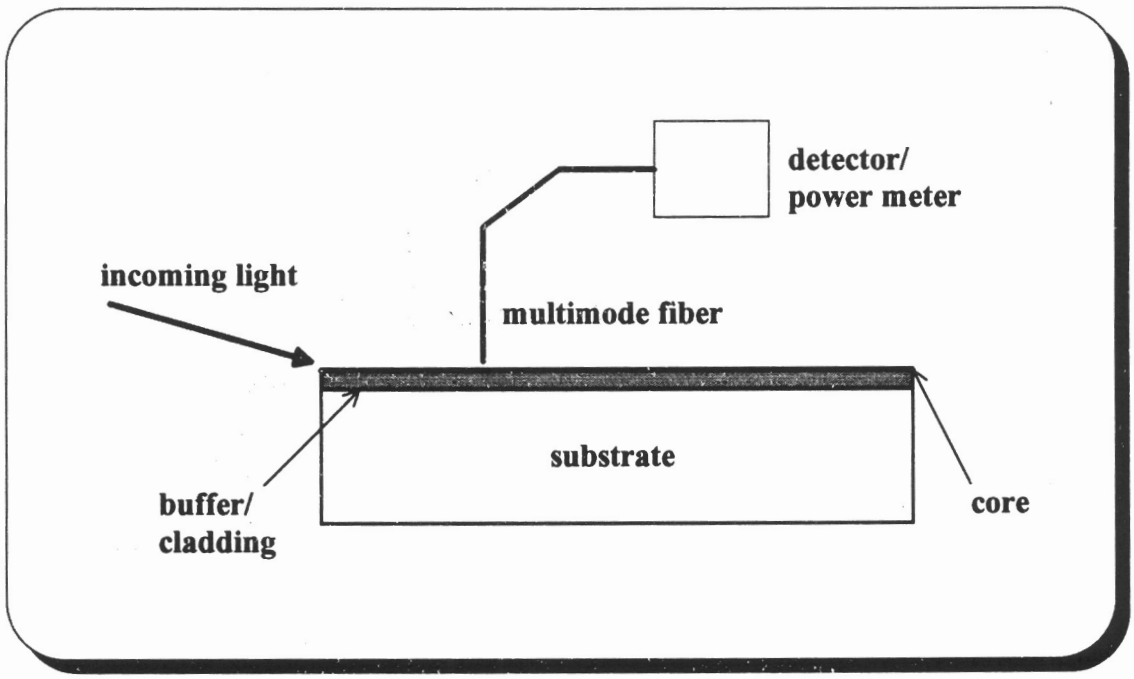

Figure 4.23 - Scattered light intensity technique

This technique is useful in evaluating the attenuation of waveguide structures that suffer from significant scattering. Light from a He-Ne laser is directed onto the end face of the planar waveguide. A large core multimode optical fiber is positioned a few millimeters

above, and perpendicular to, the top surface of the waveguide. Scattered light from the waveguide couples into the fiber, is detected by a photodetector, and is measured with a power meter. Measurements are taken at several points along the length of the waveguide by moving the optical fiber short intervals. The slope of the scattered light intensity versus distance along the waveguide gives an approximation of the attenuation of the structure. Difficulties are again encountered with coupling light from the He-Ne laser into the end face of the waveguide. This will obviously introduce error into the measurement results. Nevertheless, using repeated measurements in an attempt to reduce this error factor, an estimate of the attenuation is obtained (Figure 4.24).

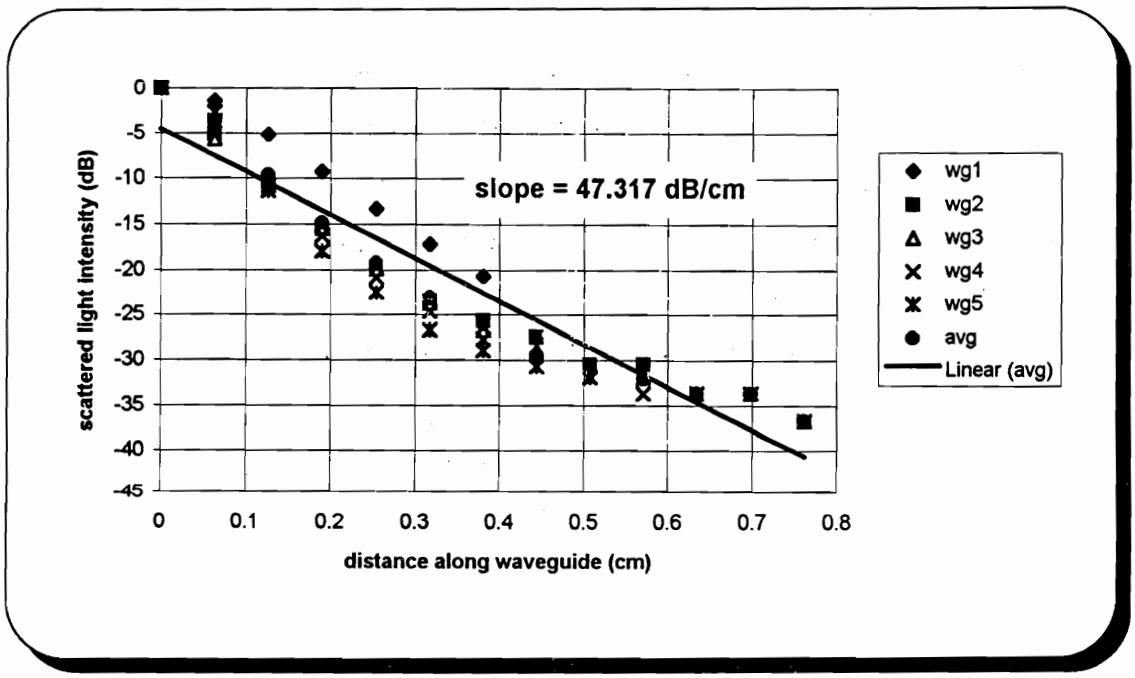

Figure 4.24 - Estimated attenuation of thick film waveguide structure

This result (47 dB/cm) is notably higher than the values reported for lower temperature glasses (750° C - 980° C), using the same evaluation technique (7.7 - 28 dB/cm).[20] Such a high value, however, is expected due to the excessive scattering of light that has been observed. As discussed earlier, modification of the paste components and/or processing

conditions, may eliminate the crystalline structures that are detrimental to the optical performance of this thick film waveguide structure. These modifications may include the use of different glass additives to decrease the possibility of devitrification. In addition, recall the importance of rapidly cooling a GeO_2 melt in order to maintain a glassy state. A modified firing profile, with faster cooling stages, may therefore be implemented.

4.5 Equipment

4.5.1 Fabrication and Processing Equipment

This section discusses the equipment used in the processing and realization of the various films for this research work.

Primary materials used in the formation of the thin films include Ge and GeO_2 powders, oxidation equipment (Lindberg tube furnace, Omega CN3000 controller, and O_2 flow meter), a thermal evaporation chamber, and substrates (quartz and LTCC).

Primary materials used in the formation of the thick films include the weighing scales, paste components, milling equipment, 80 and 250 mesh screens, de Haart screen printer, Blue-M drying oven, Deltech programmable furnace (model DT-31-FL) with Eurotherm controller (type 818), and substrates (alumina and sapphire).

Primary materials used in the production of the LTCC substrates include Green Tape™ 851-AX, blanking die (3" x 3"), laminating die (3" x 3"), Dake uniaxial press, and Isotemp programmable ashing furnace (model 497).

4.5.2 Evaluation and Testing Equipment

This section discusses the equipment used to characterize the various films produced in this research work.

An environmental scanning electron microscope (ESEM) has been used to analyze the sintering quality of the thick films at several processing temperatures.

Ellipsometry equipment has been used to determine the indices of refraction of the thick films, and estimate the thicknesses of the thin film structures. Ellipsometry uses

reflection of light from the surface of a film to determine the complex refractive index of the film. The complex refractive index is given by Equation 4.20.[51,56]

$$N = n + ik \tag{4.20}$$

where: N = complex index of refraction

n = (real) index of refraction

k = extinction coefficient

and $\alpha = \frac{4\pi k}{\lambda}$ = absorption coefficient

$\varepsilon = \varepsilon_1 + i\varepsilon_2 = N^2$ = dielectric function

where: $\varepsilon_1 = n^2 - k^2$

$\varepsilon_2 = 2nk$

The electric field vector associated with the light may be expressed by Equation 4.21.

$$\mathbf{E} = (E_x\mathbf{x} + E_y\mathbf{y})\exp[i\omega(Nz/c - t)] \tag{4.21}$$

As shown in Figure 4.25, this electric field vector may be resolved into two components - one parallel (p) and one perpendicular (s) to the plane of incidence. Light of a given polarization is incident on the surface of the film at an angle, ϕ. The complex amplitude reflection coefficients are then defined by Equations 4.22 and 4.23.

$$r_p = |r_p|\exp(i\delta_p) \equiv E_{rp}/E_{ip} \tag{4.22}$$
$$r_p = (\varepsilon_s N_{a\perp} - \varepsilon_a N_{s\perp})/(\varepsilon_s N_{a\perp} + \varepsilon_a N_{s\perp})$$

$$r_s = |r_s|\exp(i\delta_s) \equiv E_{rs}/E_{is} \tag{4.23}$$
$$r_s = (N_{a\perp} - N_{s\perp})/(N_{a\perp} + N_{s\perp})$$

where: $N_{a\perp} \equiv N_a\cos\phi$

$N_{s\perp} \equiv N_s\cos\phi_t = (\varepsilon_s - \varepsilon_a\sin^2\phi)^{1/2}$

δ = phase change upon reflection

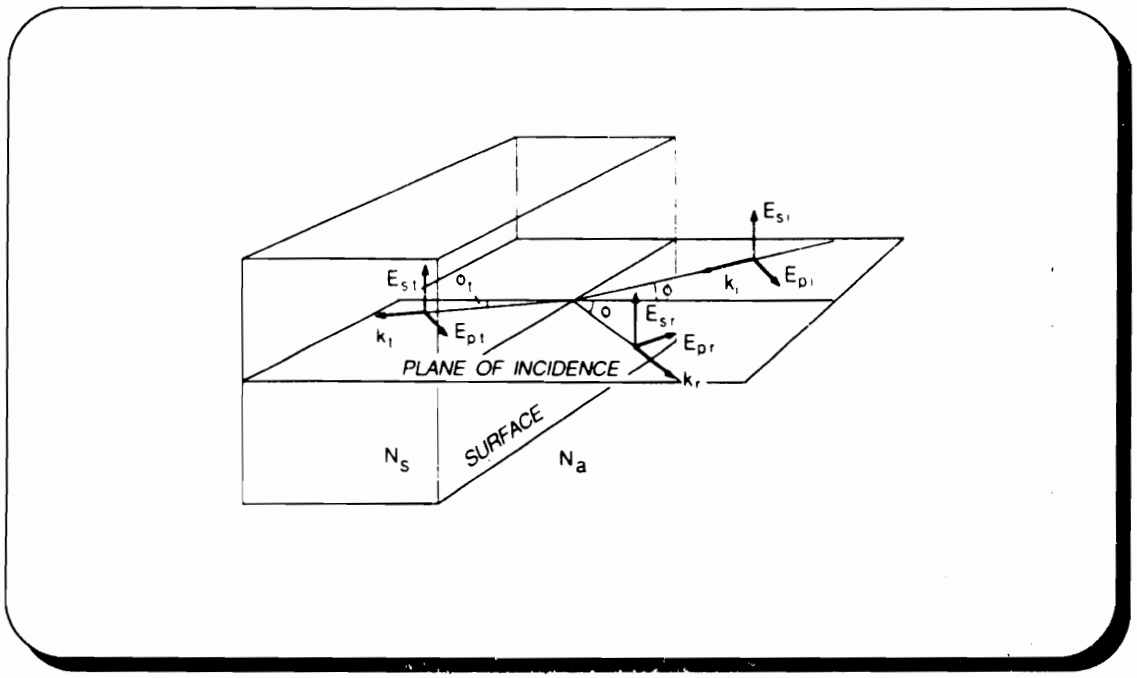

Figure 4.25 - Electric field components[56]

Ellipsometry measures the change in the polarization of the light upon reflection from the surface of the film. The polarizations of the incident and reflected light are given by the complex ratios (E_{ip}/E_{is}) and (E_{rp}/E_{rs}), respectively. The change in polarization upon reflection is then expressed as the ratio of reflected to incident polarizations, called the complex amplitude reflection ratio (ρ) (Equation 4.24).

$$\rho \equiv r_p/r_s = [(E_{rp}E_{is})/(E_{ip}E_{rs})] \qquad (4.24)$$
$$\rho = (|r_p|/|r_s|)\exp[i(\delta_p - \delta_s)]$$
$$\rho \equiv \tan\psi\exp(i\Delta)$$

In this research work, measurements of ψ and Δ have been performed for three angles of incidence (70°, 75°, and 80°). The experimental Ψ data are then fit to a Cauchy model to determine n over a wavelength range. A good estimate of k is not possible due to excessive noise in the experimental Δ data. For thin film samples, similar equations may be developed which take into account a two-interface system (ambient-film-substrate), and the resulting multiple reflections.

A scanning spectrophotometer has been used to provide an estimate of the loss of both the thick and thin films, by giving an estimate of the percent absorptance. The spectrophotometer illuminates the sample film with radiation over a range of wavelengths. The percent transmittance through and percent reflectance from the film are then measured. The remaining radiation, therefore, provides an estimate of the absorptance of the film. Figure 4.26 shows a block diagram of a spectrophotometer.[57]

A He-Ne laser, positioning equipment, large core optical fiber, photodetector, and power meter have been used in estimating the attenuation of the thick film waveguide structure.

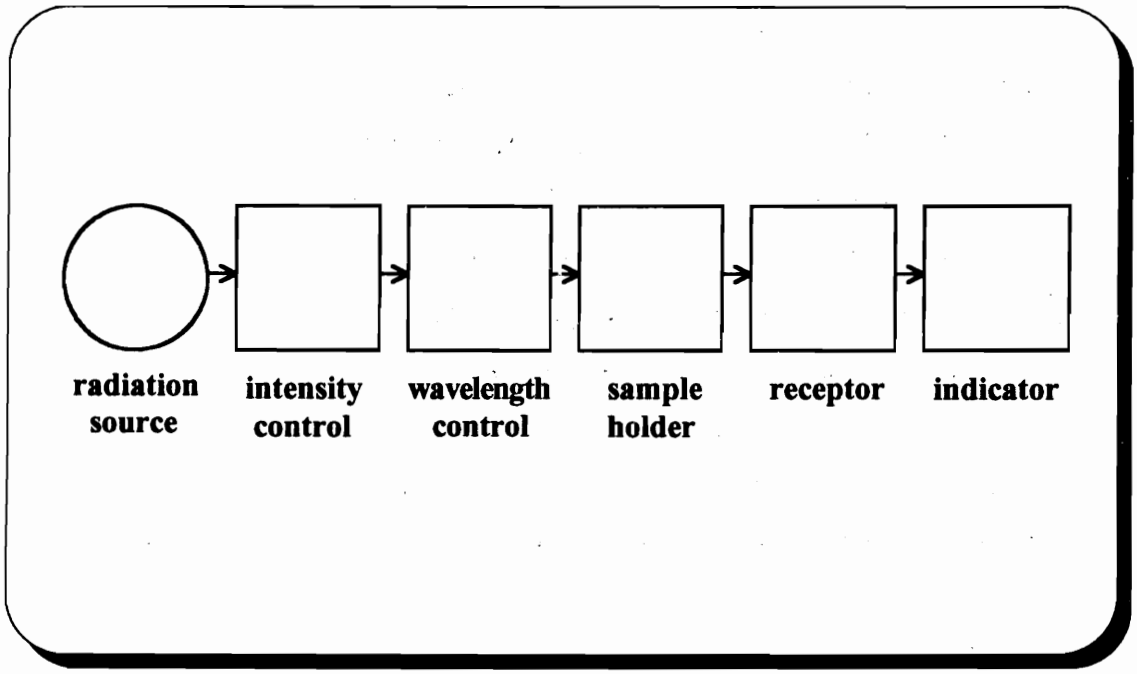

Figure 4.26 - Block diagram of a spectrophotometer[57]

4.6 Results and Conclusions

This chapter has addressed the planar waveguide portion of the integrated optoelectronics package. A discussion of the operation, design, and analysis of planar waveguides is included, however, the focus of Chapter 4 has been on the development of

optical materials that may be used in the fabrication of planar waveguide structures. Along these lines, the chapter has identified some general waveguide criteria. In addition, it has provided a review of the wide variety of materials, as well as the main fabrication techniques, used for planar waveguide structures.

Research results have been presented for the development of both thin film and thick film GeO_2 materials. Preliminary tests have been performed to evaluate the oxidation characteristics of Ge. These results also describe the effects a substrate material may have on the oxidation of thin surface films. Ellipsometry data have been presented which demonstrate the effect of different oxidation conditions on the thickness of the oxide formed. As expected, the oxide thickness increases with oxidation time and temperature.

From these tests, two types of thin film GeO_2 are designed and fabricated - an oxidized Ge thin film and a thermally evaporated GeO_2 thin film. Spectrophotometry data have been obtained to evaluate the optical quality of these two types of GeO_2 thin films. The oxidized Ge film appears to suffer less loss than the thermally evaporated GeO_2 film. This may be attributed to two factors - poor deposition quality of the evaporated film, and some inherent annealing of the Ge film that takes place during oxidation. In addition to their inherent porous nature, thermally evaporated thin films are prone to stress effects. The deposition of hot gaseous components onto a relatively cool substrate induces thermal stresses which act as scattering mechanisms. These stresses may be relaxed by post-annealing techniques that heat both the film and the substrate to a common elevated temperature.

In order to enhance the application potential of the new optoelectronic integration package, a thick film GeO_2 paste is also investigated. Many paste compositions and processing conditions have been investigated in an attempt to optimize the optical quality of the printed film. Six different paste compositions have also been manufactured and processed, using two types and three concentrations of glass additives. Ellipsometry has been used to determine the effect of different compositions on the refractive indices of the films.

These results indicate a relatively low refractive index value for the high GeO_2 concentration films. The 90 wt. % GeO_2 / 5 wt. % glass additive compositions have produced films with refractive indices of 1.40 and 1.43. This is significantly lower than the 1.61 value reported for pure glassy GeO_2. This discrepancy may be due to a number of factors, including the physical structure of the film, impurities in the paste components, and chemical reactions among paste components during processing.

Higher concentrations of the Bi-Zn-B glass additive in the paste composition have resulted in an increase in the refractive index of the resulting film. The 75 wt. % GeO_2 / 20 wt. % Bi-Zn-B film has a refractive index of approximately 1.50. This value increases to 1.73 for the 60 wt. % GeO_2 / 35 wt. % Bi-Zn-B composition. This increase in the refractive index with glass additive concentration is likely due to the relatively high refractive index features of the oxides which comprise the glass.

Higher concentrations of the SiO_2 glass additive in the paste composition have resulted in a less drastic increase in the refractive index of the resulting film. The 75 wt. % GeO_2 / 20 wt. % SiO_2 film has a refractive index of approximately 1.51. However, this value drops to 1.48 for the 60 wt. % GeO_2 / 35 wt. % SiO_2 composition. Thus, as the concentration of SiO_2 increases, the resulting film behaves more like pure SiO_2 glass ($n \sim 1.46$).

Again, spectrophotometry data have been used to evaluate the loss characteristics of one of the films, providing a loss estimate on the order of 15 - 20%. Although thick films have traditionally been more lossy than their counterpart thin films, this high loss estimate is possibly due to some devitrification of the film. Additional optimization of the composition and processing conditions, in order to prevent devitrification, is therefore likely to reduce these loss values.

The results concerning the effect of paste composition on the refractive index of the thick film have allowed the development of a waveguide structure. A low index paste is used as the buffer between the substrate and the core region. The core region is then formed from a higher index paste. Two techniques have been investigated in the

fabrication of thick film optical waveguides - cofiring and multiple firing. The cofiring method produces waveguides with noticeably better core definition. The use of multiple firings, on the other hand, causes more interaction between the buffer and core layers, and therefore less structural definition. Three separate techniques have been used in an attempt to determine the attenuation characteristics of the thick film waveguide structure. Two of the methods, involving the coupling of light in and out of the waveguide through optical fibers and prisms, have not been successful. Bulk and surface scattering of the light due to crystalline structures within the films prevent sufficient transfer of light through the waveguide. A third technique measures the intensity of the light scattered along the length of the waveguide. This method has provided a means of estimating the high attenuation characteristics of a structure that suffers from significant scattering mechanisms. Again, optimization of the paste compositions and processing conditions is necessary to prevent devitrification of the film. Minimizing the crystalline structures within the film will not only lower the attenuation due to bulk scattering, but will also improve the coupling efficiency by reducing surface scattering. These improvements will allow the attenuation to be measured through more traditional techniques.

Chapter 5 will discuss the integration of the planar optical waveguide of Chapter 4, as well as the optical receiver circuitry developed in Chapter 3. This chapter will also address the integration of an optical fiber within the electronic packaging material.

Chapter 5
Integration of Optical and Electronic Components

5.1 Introduction

This chapter proposes and evaluates a new packaging scheme for integrated optoelectronics applications. The base material for this integration is a low temperature cofireable ceramic (LTCC). LTCC materials have attracted much attention recently in electronic packaging applications, such as multichip modules (MCMs). The use of LTCC materials in fiber optic systems is not a new concept.[22,23] However, this research presents an alternative technique in which an optical fiber is not just connected to the LTCC package, but is actually integrated within the LTCC material along with the electronic circuitry. This technique provides the internal interconnection capability described in Chapter 1.

Chapter 5 is comprised of three main tasks. First, the integration of a fiber within an LTCC package is investigated. Second, this integration is expanded such that the fiber also interfaces with the optical receiver circuitry of Chapter 3. Finally, incorporation of a thick film planar waveguide within the LTCC material is investigated. This will allow optical waveguide structures and devices to be packaged within the same LTCC module as the electronic circuitry.

5.2 Background

As discussed in Chapter 2, there are various techniques used in the integration of optical and electrical components.[24-26,33] In general, these techniques involve some physical modification of the package and/or the addition of extra connector structures in order to couple an optical fiber to electronic circuitry and planar waveguide components. The goal of this research, therefore, is to avoid additional processing steps and reduce package size by integrating an optical fiber directly within an LTCC electronic package.

Regardless of the integration technique used, the main factor that will determine its effectiveness is the coupling efficiency. Coupling efficiency may be defined as a measure of the amount of optical power that is coupled from one device (1) to another (2) (Equation 5.1):[1]

$$\eta = \text{coupling efficiency} = \frac{P_2}{P_1} \qquad (5.1)$$

In this work, there are three important coupling efficiencies to consider:

1. from the fiber to the detector
2. from the fiber to the waveguide
3. from the waveguide to the detector

If the detector has a large sensitive area (relative to the fiber and waveguide dimensions), items 1 and 3 become less important. The interface between two components of similar dimensions (item 2), however, must be treated more carefully. Analysis of this type of interface is addressed in the Appendix.

The quality of the coupling between two waveguides is influenced by the following factors:[1]

1. geometrical characteristics, such as the size and shape of the two waveguides
2. waveguide characteristics, such as the refractive indices of the core and cladding regions
3. mechanical misalignments between the two waveguides
4. power distribution throughout the cross section of the waveguide structures (dependent on modal characteristics)
5. end face quality of the two waveguides

Differences in the geometrical shape of the two waveguide cores will clearly affect the coupling efficiency. For example, if the receiving core is smaller than the source core, optical power will be lost. Similarly, waveguide characteristics, such as the indices of refraction of the core and cladding regions, influence the coupling efficiency by determining the "acceptance angle" of the waveguide. The acceptance angle represents the range of directions from which light can enter the waveguide and propagate effectively.

Mechanical misalignment is divided into three categories - lateral misalignment, longitudinal misalignment, and angular misalignment (Figure 5.1). Anywhere from none to all three of these may be present in a given situation.

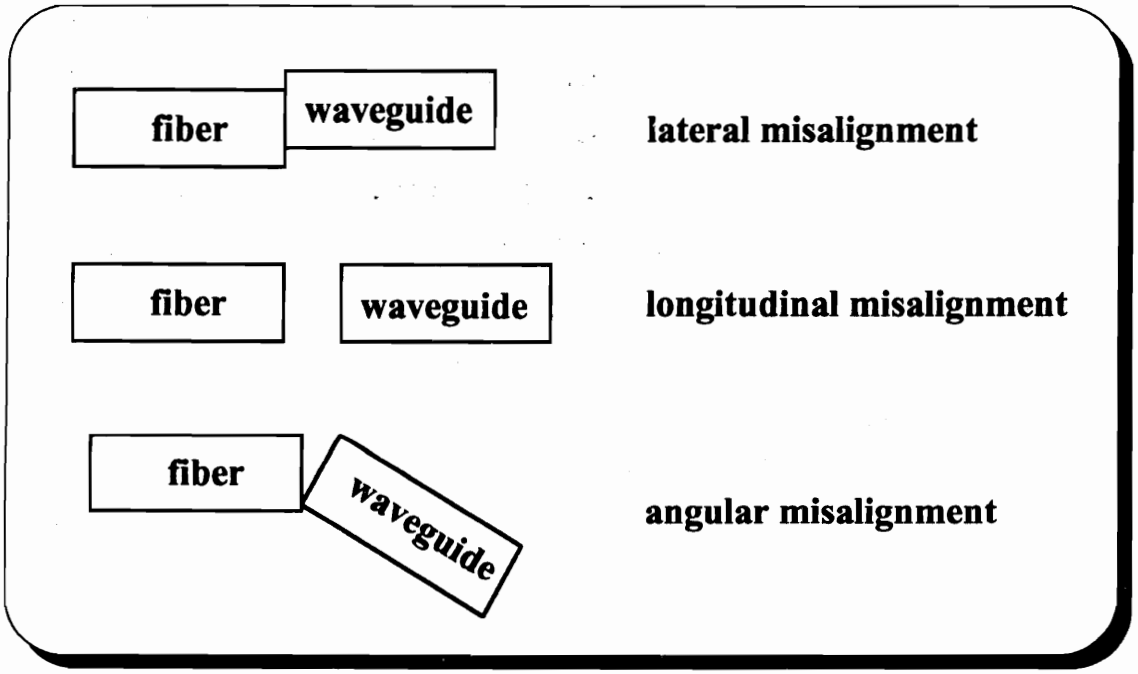

Figure 5.1 - Mechanical misalignment[1]

Coupling efficiency is also affected by the power distribution within the core. If all modes are equally excited, the power is evenly distributed throughout the core. This requires very careful alignment, as the entire core area is carrying information. However,

for long waveguides, a steady state equilibrium condition is reached such that most of the power is eventually distributed among the lower order modes. Thus, not all of the core region is carrying information, and alignment becomes less critical.

Finally, the quality of the end faces of the two waveguides will also determine the efficiency of the coupling. Reflection and scattering from the end faces of the waveguides will alter the amount of light that would normally enter through the acceptance angle.

5.3 Experimental Procedures

5.3.1 Integration of Fiber within LTCC Material

In order to integrate an optical fiber within an LTCC package without the need for extra connectors, processing steps, etc., the fiber must be inserted before the lamination stage of the Green Tape™ fabrication process. In the first test, a total of 12 layers of 851-AT will be used. A 1" x 1" window is cut in the center of six of the tape layers. The other six layers are positioned in the 3" x 3" laminating die. A short length of fiber is placed on top of these layers, and the remaining six layers (with windows) are then placed on top of the fiber. The fiber is positioned such that it extends partially into the window region formed in the upper six layers of tape (Figure 5.2). The other end of the fiber that extends outside of the package will be cut off by the top of the laminating die. The window "cut-outs" are reinserted into the window on top of a release layer before lamination is performed. This allows sufficient pressure to reach the window cavity, while the release film prevents the cut-outs from laminating and closing up the window. After lamination, the cut-outs and release film are removed, and the package is burned-out and fired. After firing, visual inspection reveals that the plastic coating of the fiber has burned off, leaving behind an ashy residue, and that the fiber is also moveable along the axis of its channel. Inspection under a microscope reveals no apparent damage to the fiber.

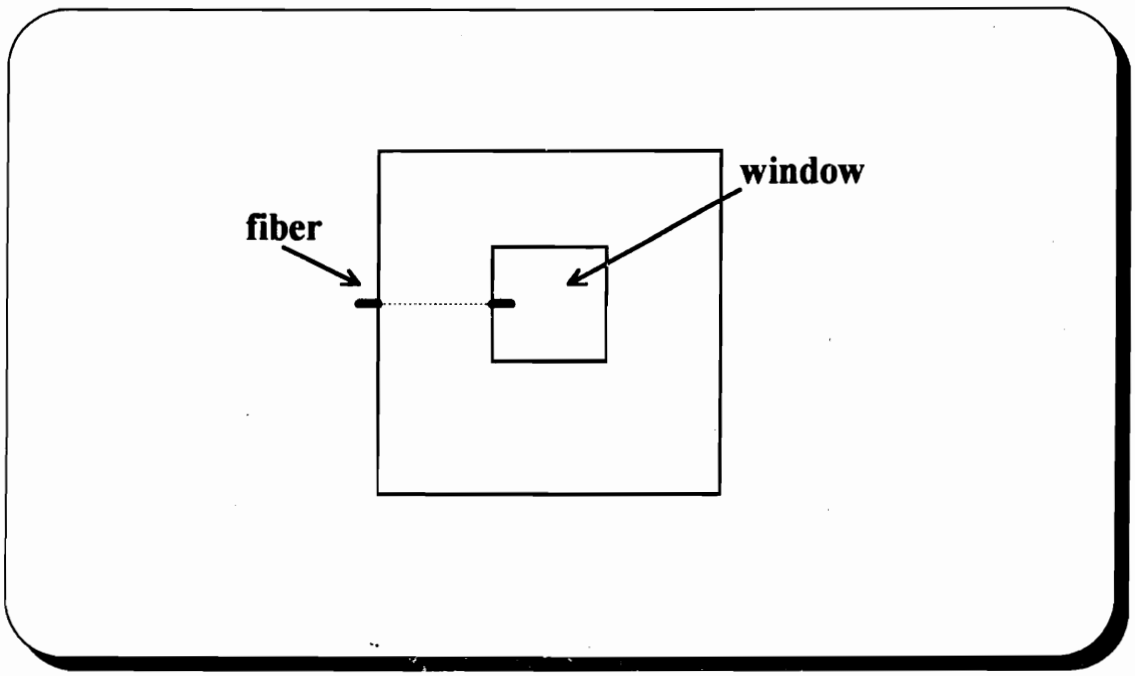

Figure 5.2 - Package with window

The focus now turns to the development of a sample with a longer fiber end extending outside the package, so that measurements may be performed. Since the laminating die may not be used, an isostatic lamination system will be utilized. This process involves stacking the Green Tape™ layers on a large alumina setter. The fiber is then positioned in the middle of the stack with both ends extending outside the stack (Figure 5.3). A release film is used at the bottom of the stack to prevent any sticking to the setter, and on the top of the stack such that the stack may be taped in place on the setter. The long fiber ends, outside the sample, are wound and taped to the setter, as well. The setter is then placed in an anti-static bag and vacuum sealed. To prevent water from the isostatic lamination chamber from contacting the sample, the sample is double-bagged as a precaution. After lamination, the tape stack and the wound fiber ends are untaped, and the release films are removed. The setter is cleaned, and the fiber ends are rewound and taped to the setter. Small alumina substrates may be placed on top of the windings to prevent shifting once the tape burns off during burn-out and firing. After firing is complete, visual inspection

reveals some breakage in the wound ends. This is due to stress induced during lamination, as well as the brittle nature of the fiber after processing.

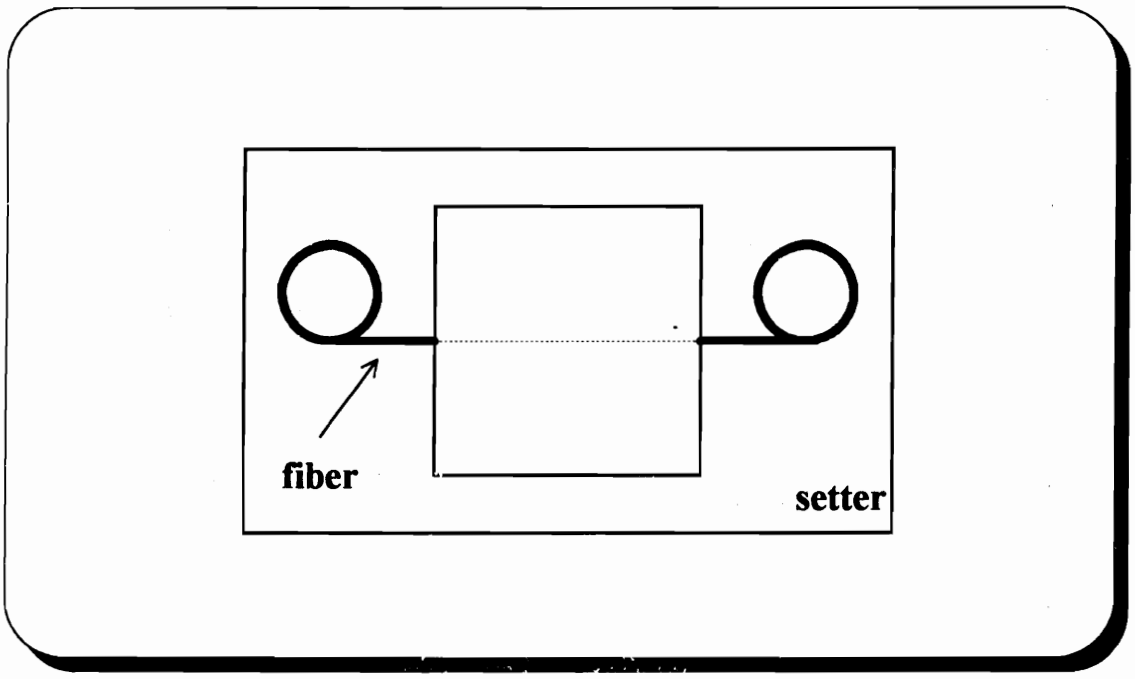

Figure 5.3 - Package with wound fiber ends

Based on these results, a new approach is implemented. Since the fiber is not fixed in the channel, and is too brittle for measurements, it will be completely removed from the channel and replaced with a new, long piece of fiber. This new fiber must first be stripped (or a smaller diameter fiber must be used), since the fiber coating burns off during processing, and thus the channel conforms to the size of the uncoated fiber. Since the fiber has created its own "custom-made" channel (which remains rigid after firing), a stripped replacement fiber of the same type provides a perfect fit with no expected loss in coupling effectiveness and negligible added process time. Although a smaller unstripped fiber may provide a less perfect fit, the effectiveness will only be affected if coupling to a device that is similar in size to the fiber diameter. An optical spectrum analyzer is then used to evaluate the effect of the integration on the fiber, by measuring the power through

the fiber both before and then after it has been inserted into the channel. A stripped 1300 nm fiber and a smaller diameter 500 nm fiber (unstripped) are tested, and the results are shown in Figures 5.4 - 5.7.

These results demonstrate that the process of integrating an optical fiber within the LTCC material has no effect on the transmission properties of that fiber. This appears to be equally true for unstripped fibers, as well as fibers that have been stripped of their external plastic coating. During the integration process, there is a possibility that some stress may be induced on the fiber due to its confinement within the LTCC channel. This type of external force often results in the formation of small bends (microbends) along the length of the fiber.[1] These structural deformities act a type of loss mechanism. They may cause power to be coupled from one mode to another, resulting in signal distortion, or they may cause power to be coupled out of the fiber altogether.

Figures 5.4 and 5.5 demonstrate the results for the integration of an unstripped 500 nm fiber into the LTCC material. Around the operation wavelength, the difference between the power transmission through the fiber, before and after insertion, is negligible (i.e. within the repeatability range of the measurement). In particular, between the wavelengths of 460 nm and 600 nm, the fiber exhibits only a 1 - 2 dB variation before and after integration. A larger variation in the power transmission is observed around the 425 nm wavelength. This wavelength may be close to the cutoff wavelength for the single mode fiber. As the operation wavelength approaches the cutoff wavelength, a larger percentage of power is carried in the fiber cladding. Power in the cladding is more sensitive to bends in the fiber, such as may occur as a result of the integration technique.

Figures 5.6 and 5.7 demonstrate the results for the integration of a stripped 1300 nm fiber into the LTCC material. This fiber exhibits negligible change in its transmission properties before and after insertion. Specifically, for operation wavelengths from 1050 nm - 1550 nm, there is less than a 1 dB variation in the performance of the fiber. This is definitely within the repeatability range of the measurement.

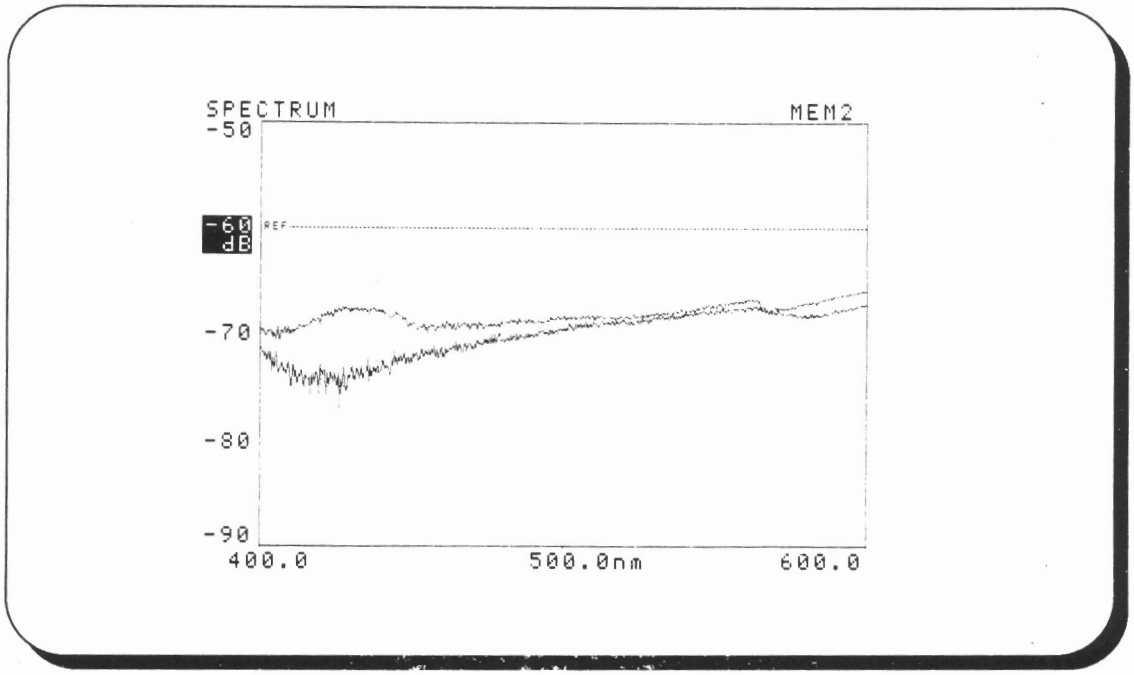

Figure 5.4 - 500 nm fiber

(responses for the fiber alone and the fiber integrated within the LTCC)

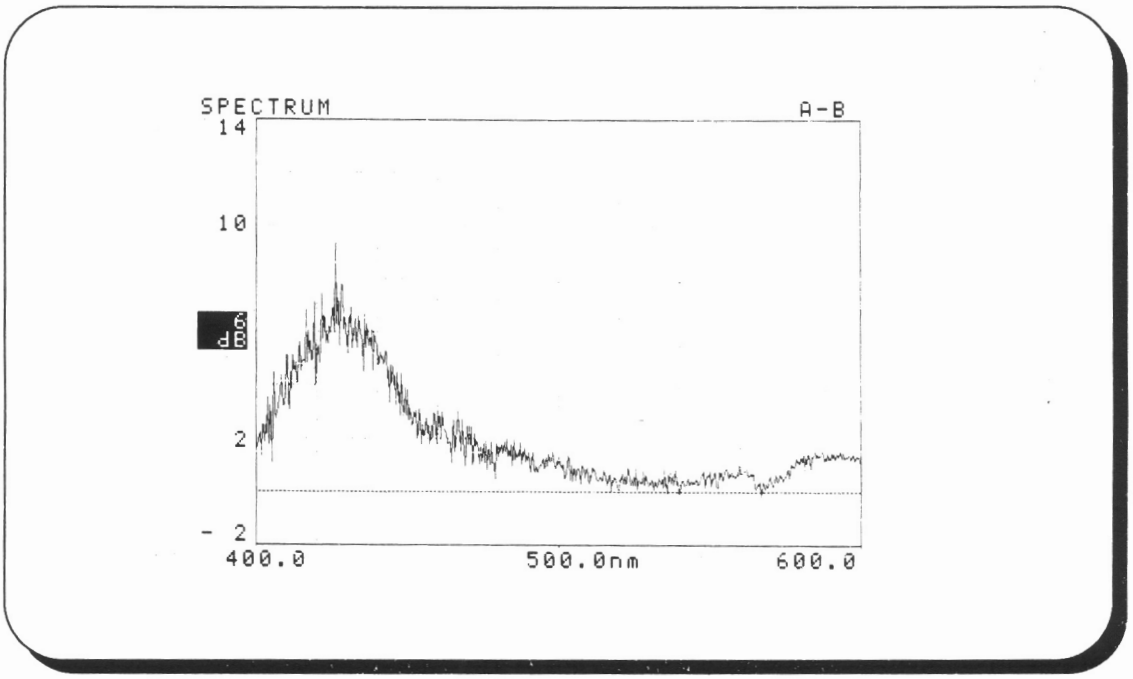

Figure 5.5 - 500 nm fiber

(difference between the two responses of Figure 5.4)

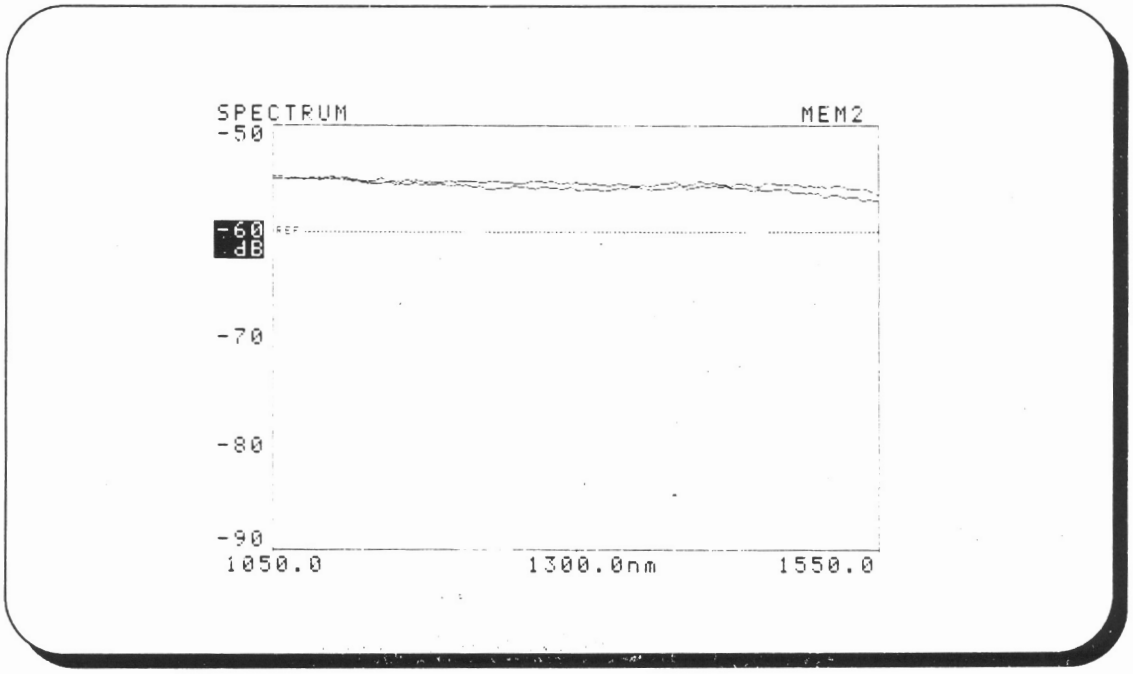

Figure 5.6 - 1300 nm fiber

(responses for the fiber alone and the fiber integrated within the LTCC)

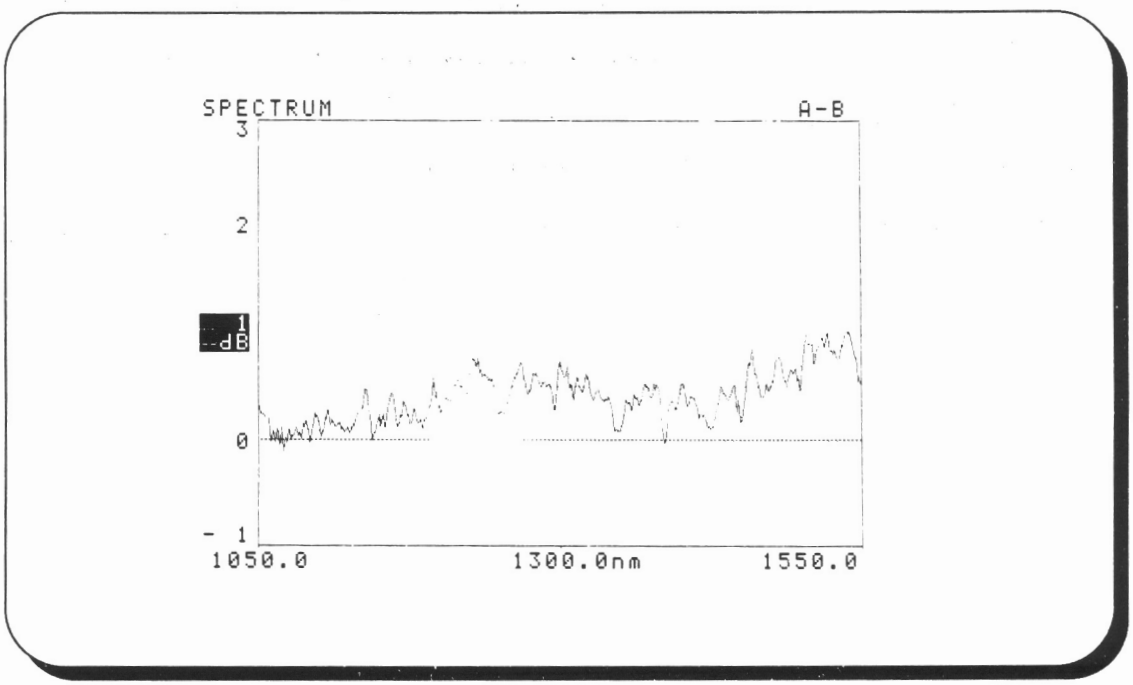

Figure 5.7 - 1300 nm fiber

(difference between the two responses of Figure 5.6)

5.3.2 Integration of Fiber with Optical Receiver Circuitry

The strategy of this section is to produce a fiber optic receiver in which the interface between the electronic circuitry and the optical fiber is self-contained within an LTCC module, without the use of extra connectors or additional mechanical processing steps. Normally, the interface between an optical fiber and the electronics is achieved through the use of a mechanical connector, which holds the fiber in place and properly couples it to the electronic component. The ability to integrate the optical fiber within the LTCC packaging material, and couple it to an electronic component within the module is beneficial in that it eliminates the need for this mechanical connector. The packaging material creates its own "connector" which is automatically a custom fit to the size of the integrated optical fiber(s). This capability enhances the flexibility of module design, and promotes further miniaturization of the overall package.

The proposed structure of the LTCC fiber optic receiver module is shown in Figure 5.8. The package consists of a cavity region which contains the hybridized receiver circuitry. The cavity is surrounded by a wall, approximately 0.5" wide and approximately 0.13" high, on three sides. This wall structure is created by cut-out layers of LTCC material. The optical fiber enters the wall region (between successive layers of LTCC) approximately 0.1" above the level of the cavity region, such that it may interface with the active portion of the phototransistor (Figure 5.9). The fourth side of the package provides access to the receiver biasing and output.

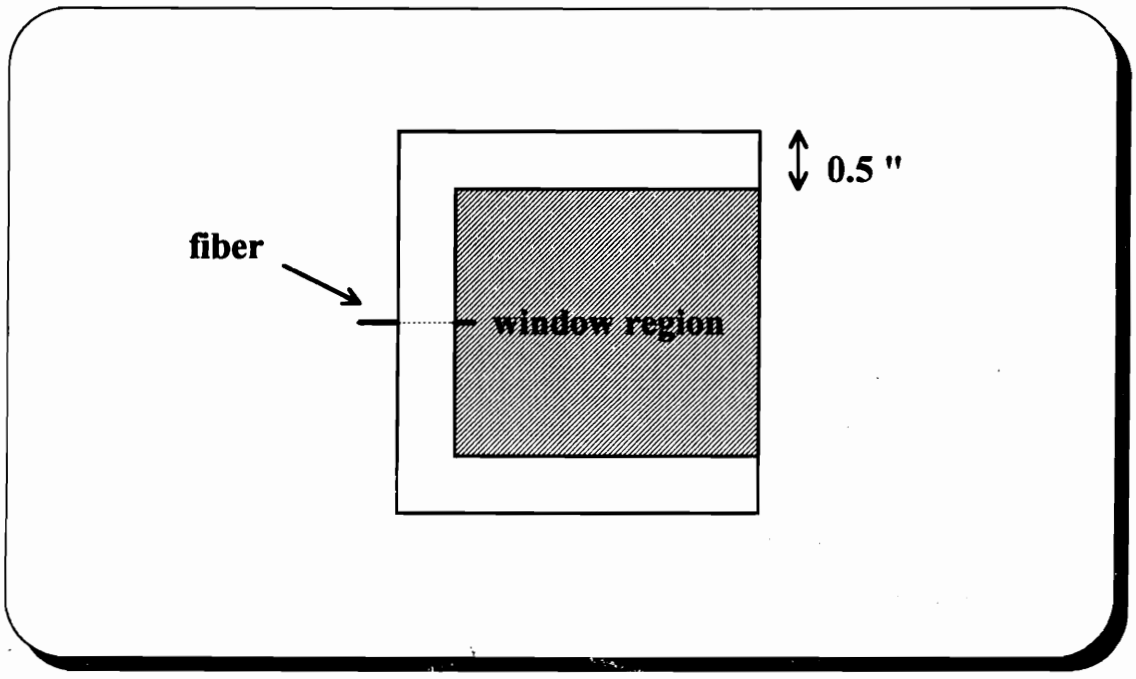

Figure 5.8 - Integration of fiber with receiver circuit

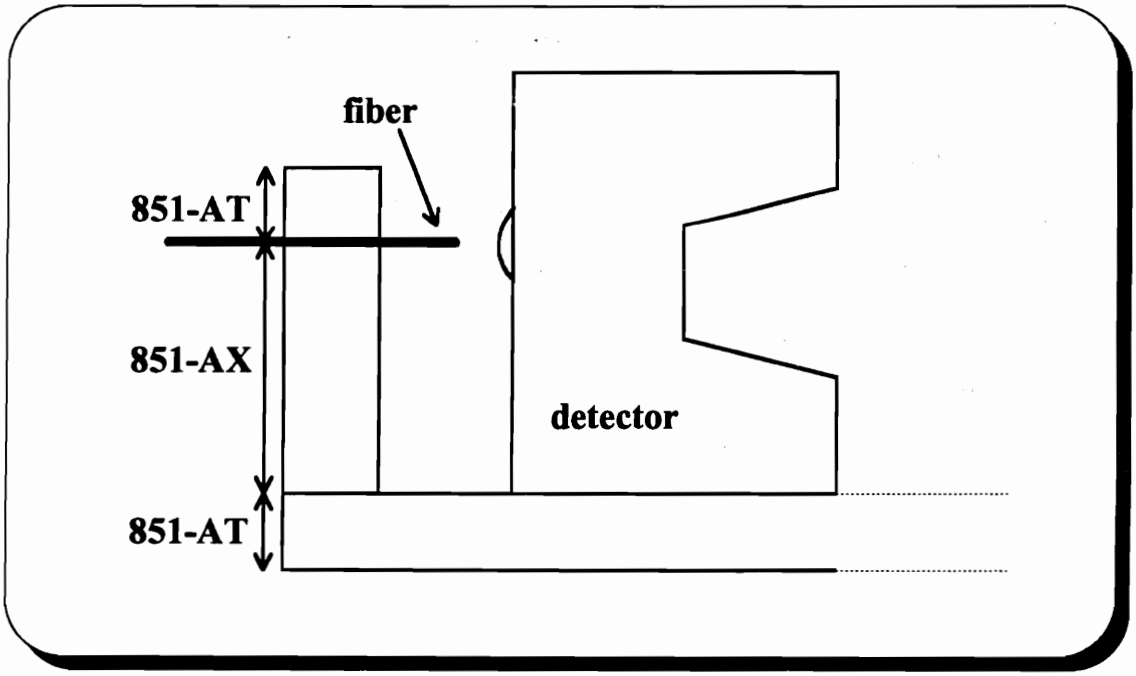

Figure 5.9 - Composition of the wall region

Additional Green Tape™ parts are blanked to create this structure:

8 layers of 851-AT
12 layers of 851-AX
7 layers of 851-AT

Note that the Green Tape™ 851 system exhibits a z-direction (thickness) shrinkage of approximately 17% after firing. The 851-AT tape has a thickness of 4.5 mil before firing, and approximately 3.7 mil after firing. Likewise, the 851-AX tape has a pre-fired thickness of 10.5 mil, and a post-fired thickness of approximately 8.7 mil.

A window is cut in the top eight layers of 851-AT and the 12 layers of 851-AX. The other seven layers of 851-AT are used for support below the printed layer from Chapter 3. The layers are positioned in the laminating die, beginning with the seven layers of 851-AT and the one printed layer, followed by the 12 layers of 851-AX. A short piece of 1300 nm fiber is inserted on top of the uppermost 851-AX layer, as shown in Figure 5.9. The eight layers of 851-AT are then placed on top of the fiber, to complete the structure.

Again, the window region "cut-outs" are reinserted (on top of release film), and the stack is laminated at 70° C for 30 minutes (instead of the usual 10 minutes) due to the increased thickness. After lamination, the cut-outs and release film are removed, and the part is burned-out/co-fired in the ashing furnace with the following profile (Figure 5.10). Note that this profile performs burn-out and firing in a single stage, without having to relocate the sample. The fiber is carefully removed from the package after firing.

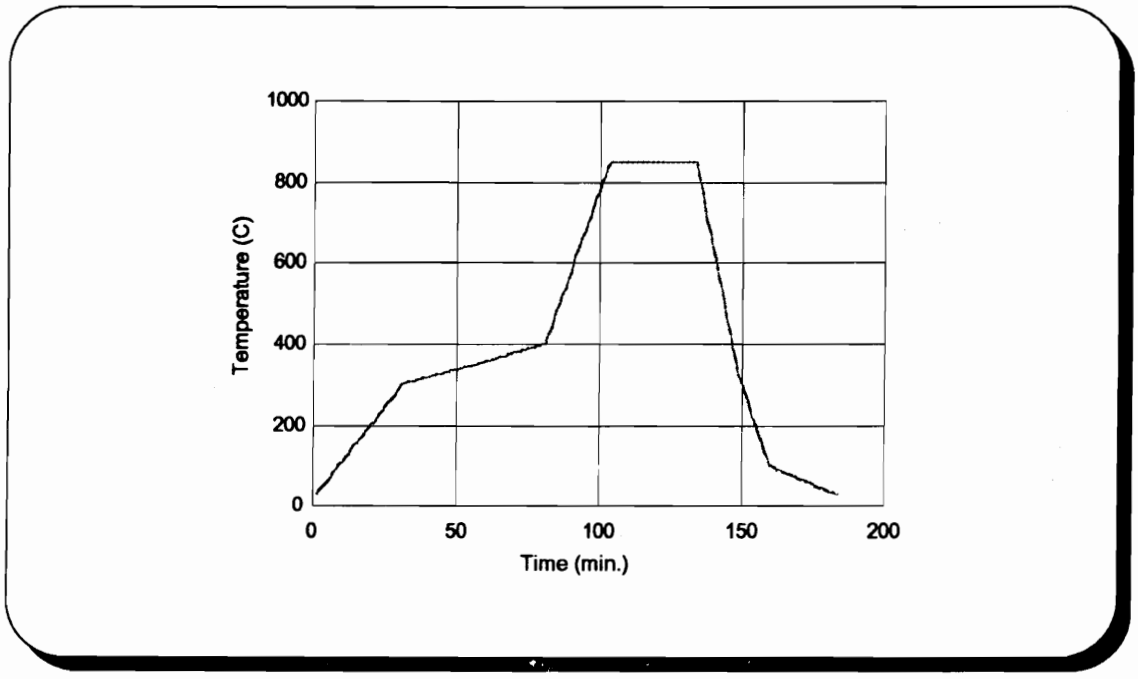

Figure 5.10 - Burn-out/co-fire profile for Green Tape™ 851 system

Attempts to solder the receiver components, as well as lead wires, to the printed pattern are unsuccessful, due to the composition of the DuPont 6142D paste. Instead, Epo-tek H20E silver epoxy is mixed and carefully dabbed onto the component pads. The components (and lead wires) are then positioned on the pads, and the epoxy is cured at 100 - 110°C for one hour. Continuity is verified with an ohmmeter after curing.

An approximately two foot length of 820 nm fiber is stripped and cleaved on both ends. Alignment equipment, consisting of a mounting frame, an X-Y positioner with fiber chuck, and a bracket holder, will be used to test the package (Figure 5.11). The pigtail end from the E/O converter is taped down to the bracket holder. One end of the fiber is placed in the chuck, and the chuck is then inserted into the X-Y positioner. The other end of the fiber is carefully inserted into the package channel. After some rough alignment of the E/O pigtail end to the fiber, a clean output sinusoidal signal is observed.

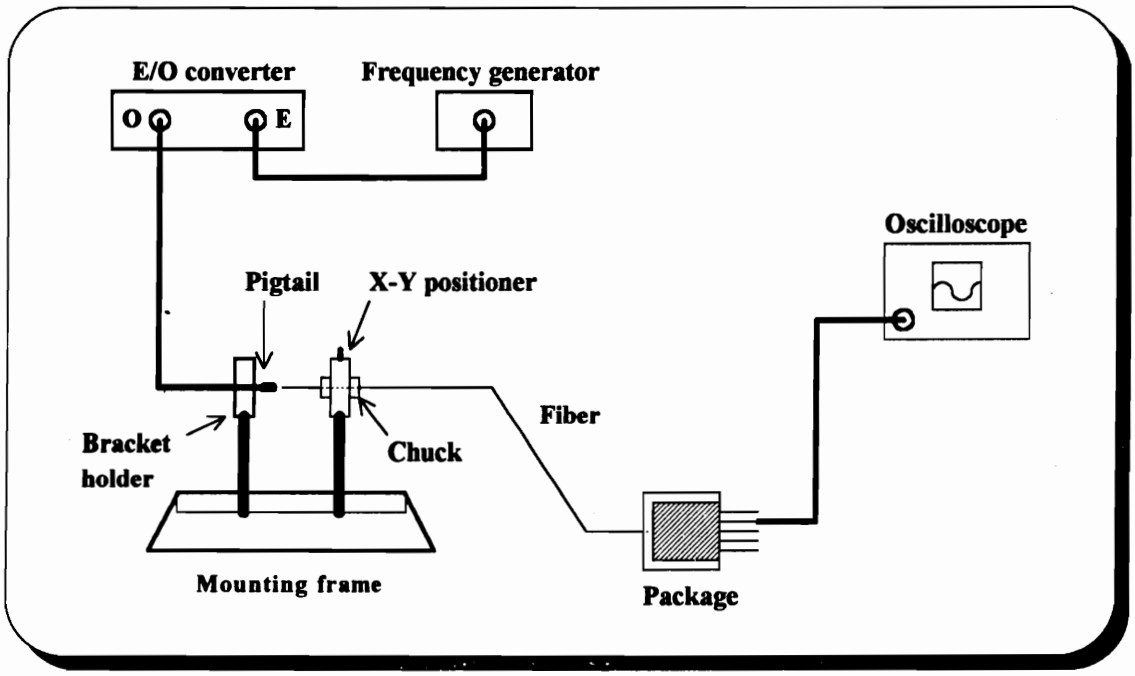

Figure 5.11 - Test set-up for the package

It is important to note that alignment has not been a problem with this design. The alignment of the fiber to the detector is not very critical due to the large sensitive area of the component. Nevertheless, the packaging style limits movement of the fiber to along the direction of the channel. The number of Green Tape™ layers, and the positioning of the fiber in the stack before lamination may be determined so as to minimize the lateral misalignment. Angular misalignment is automatically minimized by laminating the fiber between two planar tape layers. The amount of longitudinal separation between the fiber and the detector may be adjusted for best performance, and then the fiber may be epoxied in place. In addition, the most difficult alignment, between the pigtail end and the fiber, is not a practical concern. This is due to the use of splice tubes which, in practice, will connect the incoming optical fiber to the fiber that is integrated within the receiver package.

5.3.3 Integration of Waveguide with Package

The ability to include a planar optical waveguide within an LTCC package enhances the flexibility of the proposed integration technique even further. The use of planar optical waveguide structures and devices within a fiber optic system typically requires a larger, or possibly separate, packaging module. The use of cofireable ceramics, on the other hand, allows the planar optical waveguides to be incorporated simply as another layer within the same multilayer module as the electronics. To take advantage of this feature, the demonstrated ability to integrate an optical fiber within the internal layers of an LTCC module is critical.

However, the waveguides investigated in Chapter 4 of this work must currently be processed at temperatures (1200° C) that exceed the capability of LTCC materials (850° C). One alternative may be to develop new thick film waveguide compositions that may be fired with an 850° C peak profile. This, however, may severely limit the types of materials that may be used in the thick film paste. Another alternative involves the use of high temperature cofireable ceramic (HTCC) materials. HTCC materials offer the same multilayer integration capabilities as the LTCC materials. However, these materials require processing temperatures of 1400° C - 1600° C. Although the use of HTCC materials may extend the range of potential thick film optical materials, the internal electrical structures must be formed from pastes based on lower conductivity refractory metals. As long as the processing temperatures for the thick film waveguide are lower than the processing temperatures of the ceramic packaging material, the waveguide may be incorporated as a post-fired (surface) component. Integration of the waveguide on an internal layer of the package, however, requires more exact compatibility between the waveguide processing conditions and the ceramic firing profile. To further complicate the situation, many cofireable ceramic materials experience shrinkage during their processing. Thus, thick film optical pastes, for internal integration, must also be designed to shrink in conjunction with their packaging material.

5.4 Equipment

5.4.1 Fabrication and Processing Equipment

This section discusses the equipment used in the processing of the integrated package. Primary materials include LTCC processing equipment (Green Tape™ 851-AT, Green Tape™ 851-AX, blanking die (3" x 3"), laminating die (3" x 3"), Dake uniaxial press, Pacific Trinetics Corp. isostatic lamination system - model IL-4008, Blue-M drying oven, and Isotemp programmable ashing furnace - model 497), and fiber materials (1300 nm fiber, 500 nm fiber, 820 nm fiber, and stripping/cleaving equipment).

5.4.2 Evaluation and Testing Equipment

This section discusses the equipment used to characterize the integrated package. Primary materials include alignment equipment (mounting frame, X-Y positioner, fiber chuck, and bracket holder), Tektronix equipment (2465B 400 MHz oscilloscope, FG504 40 MHz function generator, PS503A dual power supplies, and OT502 E/O converter), and ANDO AQ-6310C optical spectrum analyzer.

5.5 Results and Conclusions

This chapter has discussed the development of a new integrated optoelectronics package, in which the interface between the optical fiber and the electronic components is self-contained within the electronic module. This eliminates the need for extra connectors or other mechanical modifications to the package in order to couple optical fibers to the module. Benefits of this technique include more design flexibility and enhanced miniaturization of the total package.

The base material used in the proposed integration technique is a low temperature cofireable ceramic (LTCC) material. This material has been successful in transferring the internal interconnection capabilities of monolithic technology to the traditional field of thick film microelectronics. The result has been the emergence of multichip module (MCM) packaging of electronic systems. The integration capability developed in Chapter

5 extends the use of LTCC materials to the packaging of optical systems, while still maintaining their internal interconnection features.

The coupling efficiency term is introduced in Chapter 5 as a means of evaluating the quality of the integration technique. Important factors which influence the coupling efficiency are described in detail. Although the coupling of an optical fiber to a large sensitive area electronic device is usually not a concern, the coupling of optical fibers and planar optical waveguides is much more involved. This issue is addressed in the Appendix of this work.

Experimental results have been presented for the integration of an optical fiber within an LTCC material. This chapter outlines the equipment and the procedures used to achieve several types of integration. Optical spectrum analysis measurements are performed to evaluate the effect of integration on stripped and unstripped optical fibers. Measurements of the optical power through the fibers, both before and after they have been inserted in the package, indicate no performance degradation due to the integration.

A fiber optic receiver module is designed using these integration techniques, along with the hybridized circuit of Chapter 3. The structure of the package, as well as the fabrication and evaluation procedures, are outlined in Chapter 5. Note that measurements of the completed hybrid module are presented in Chapter 3 as a comparison to the results from the breadboarded receiver and the computer simulation.

The importance of the planar optical waveguide work (Chapter 4) as it relates to the integration techniques of Chapter 5 is also discussed. It is noted that the waveguide processing temperatures are too high for use with LTCC materials. Instead, the planar optical waveguide structures have successfully been fabricated on alumina substrates. The material properties of alumina are similar to those of high temperature cofireable ceramic (HTCC) materials which have the same integration capabilities as LTCC materials. Thus HTCC materials are a viable alternative for the integration of planar optical waveguides requiring high temperature processing.

Chapter 6 provides a general conclusion, and presents some possible considerations for future work.

Chapter 6
Conclusions and Future Work

6.1 Conclusions

The objective of this research has been the development and evaluation of a new style of integrated optoelectronics which combines the selectivity of traditional hybrid microelectronic techniques with the internal interconnection capability offered by monolithic technologies. This new packaging technique is based on a low temperature cofireable ceramic (LTCC) material, and has been implemented in a fiber optic receiver system. The work has been divided into six chapters and an Appendix.

Chapter 1 provides an overall introduction to this dissertation. This chapter includes the motivation behind the selection of this research topic. Chapter 1 outlines the goals of the research, and the role each chapter plays in accomplishing these objectives.

Chapter 2 has highlighted published studies related to integrated optoelectronics and fiber optic receiver packaging. Specifically, Chapter 2 is divided into three main sections, to reflect the three primary research topics - the receiver, planar optical waveguides, and the integration of electrical and optical components. The first section of Chapter 2 is dedicated to the receiver portion of the research effort. Work related to photodetector devices, and especially phototransistors is discussed in this section. The second section evaluates a variety of materials and techniques used in the processing of planar optical waveguides. The third main section of Chapter 2 covers some of the recent techniques used to integrate electrical and optical components within an optoelectronic device.

Chapter 3 discusses the receiver portion of the integrated optoelectronics package. This chapter demonstrates the selectivity of the proposed packaging technique. Components of the receiver system are evaluated on an individual basis, allowing the selection of particular devices to achieve a desired level of performance. This chapter has described the role of the receiver and its two primary components - the photodetector and

the amplifier. Sources of noise in a fiber optic receiver system have also been identified and characterized. Both the photodetector and the amplifier components of the receiver system are then discussed in detail. Various types of photodetectors are described, including their operation and figures of merit. The three main amplifier configurations are also identified and evaluated. A phototransistor and transimpedance amplifier configuration are selected for use in realizing the fiber optic receiver circuit. Individual components, such as the E/O converter and photodetector bias, are modified to enhance the performance of the system. Both a breadboarded and a hybridized version of the circuit have been constructed and compared to each other, as well as to a computer simulation of the receiver. In addition, an analysis of the receiver noise has been performed, leading to a determination of the system signal-to-noise ratio.

Chapter 4 involves the planar optical waveguide. The work performed in this chapter will enhance the performance of the proposed packaging technique by providing an additional level of integration capability. This allows greater flexibility in package design, as well as a higher degree of miniaturization. This chapter includes a discussion of the operation, design, and analysis of planar waveguide structures. Much of the chapter, however, is devoted to the materials and techniques used to fabricate these devices. Due to some attractive characteristics, GeO_2 (germanium oxide) has been selected as the material to be investigated in this study. Two types of thin film GeO_2 have been developed and evaluated. The first type is created by the oxidation of a thermally evaporated Ge film. The second type is formed by the direct thermal evaporation of GeO_2. Spectrophotometry results indicate that the first type of GeO_2 thin film is of a higher optical quality, possibly due to some annealing inherent to the oxidation process. In addition, a thick film version of GeO_2 is investigated through the development of several thick film GeO_2 pastes. A number of different paste compositions have been manufactured and processed, using various types and concentrations of glass additives. The effect of paste composition on the refractive index of the resulting film has been determined through ellipsometry measurements. A high loss estimate has been obtained

for one of the GeO_2 thick films through spectrophotometry measurements. This is likely due to some devitrification of the film, which may be prevented by modifying the processing conditions and/or the paste composition. Two techniques for the formation of thick film optical waveguide structures (cofiring and multiple firing) have been tested and compared. Results indicate that better structural definition is achieved through the cofiring method. Attempts to characterize the attenuation of the waveguide structure are discussed, including difficulties encountered due to bulk and surface scattering.

Chapter 5 discusses the integration portion of the research work. The goal of this chapter is to package both the electrical and optical components of a fiber optic receiver system within a single LTCC module. This chapter demonstrates the internal interconnection capability of the proposed packaging style. A measure of the quality of an integration technique, the coupling efficiency, is discussed in great detail. An Appendix section is included at the end of the work, which analyzes the coupling of an optical fiber to a thick film rectangular waveguide. The process of integrating an optical fiber within an LTCC package is described. This process is both novel and important, in that it demonstrates how cofireable ceramics are no longer limited to electronic packaging applications, but are now capable of packaging optical components as well. Optical spectrum analysis results verify that the process of integration does not affect the performance of the optical fiber. To conclude this research study, the hybridized receiver circuit of Chapter 3 is realized in an LTCC module, and an optical fiber is integrated within the package to interface with the phototransistor component. The feasibility of expanding these integration capabilities to include the optical thick film technologies developed in Chapter 4 is also discussed.

Chapter 6 provides a conclusion to the research, and proposes some possible future work based on this study.

6.2 Future Work

This study has successfully demonstrated the integration of a fiber optic receiver system within a single LTCC module. This packaging technique may also be used in the integration of fiber optic transmitters, optical switches, optical regenerators, and virtually any application in which fiber optic cables interface with electronic circuitry. Planar optical waveguides may also be incorporated into this packaging technique in order to provide even more flexibility to the integration of optoelectronic devices. Research should therefore continue into the optimization of materials and techniques for the fabrication of thick film optical waveguides. This includes the development of new paste compositions and processing profiles that will reduce the loss characteristics of the thick film. Additional research should also be performed to investigate the potential photosensitivity features of thick film GeO_2 materials. This feature has already been demonstrated in GeO_2 thin films and GeO_2-doped optical fibers, and now may possibly be extended to GeO_2 thick films. The thick film materials developed in this work are currently limited to use in high temperature (HTCC) packaging. In addition, if the cofireable ceramic experiences shrinkage during processing, the thick films cannot be incorporated within layers of the packaging material. Future research should therefore attempt to overcome these limitations by improving the compatibility between the pastes and the packaging materials. The degree of modification to the paste composition, however, will be limited by its effect on the optical performance of the final product. One should also note that thick film optical materials may never produce waveguides with the extremely low loss characteristics observed in structures developed by other technologies. These thick film materials, however, are not intended for the manufacture of devices for long distance optical transmission. They are designed, instead, for use in miniaturized modules. Thus, a slightly higher loss may be sacrificed in favor of the benefits provided by an improved packaging capability.

Appendix

Fiber to Rectangular Waveguide Coupling Efficiency

This section evaluates the coupling of an optical fiber to a planar rectangular waveguide (Figure A.1). The effective index method discussed in Chapter 4 will be used to determine an expression for the coupling efficiency (Chapter 5) of this arrangement. This analysis will provide the waveguide designer with the ability to select appropriate parameters to optimize the coupling of these two components within the optoelectronic package.

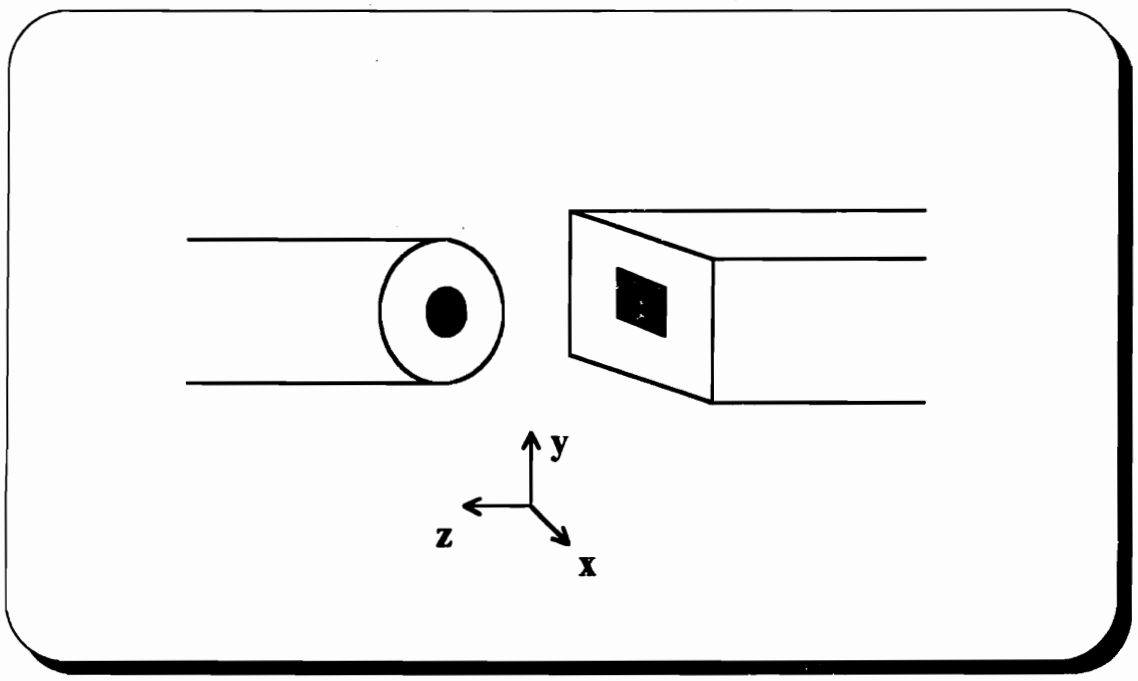

Figure A.1 - Fiber to rectangular waveguide coupling

Parameters:

fiber: core radius = a

core index of refraction = n_1

cladding index of refraction = n_2

waveguide: core length (x-direction) = b

core width (y-direction) = c

core index of refraction = n_3

cladding index of refraction = n_4

The system is considered to be single mode. Thus, the modes of interest include the LP_{01} mode for the fiber, and the fundamental mode for the rectangular waveguide.

First, consider the rectangular waveguide:

The effective index method is used to find expressions for the transverse fields. Beginning with the reduced wave equation:

$$\nabla_t^2\psi + \left(k^2n^2 - \beta^2\right)\psi = 0$$

$\psi(x,y) = \psi_x(x)\psi_y(y)$ by separation of variables

$$\frac{d^2\psi_x}{dx^2} + k_x^2\psi_x = 0$$

$$\frac{d^2\psi_y}{dy^2} + k_y^2\psi_y = 0$$

$$\beta^2 = k^2n^2 - k_x^2 - k_y^2$$

Since the x-dimension (b) of the waveguide core region is larger than the y-dimension (c), the properties of the waveguide are influenced more by the index profile in the y-direction. Therefore, the effective index method will begin in the y-direction:

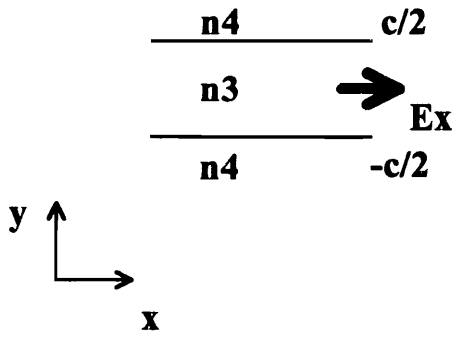

Assuming x-polarization, the electric field is parallel to the refractive index interfaces. This is indicative of a TE-type solution. Since the fundamental mode is of interest, the EVEN TE_o solution is desired:

From the wave equation:

$$\frac{d^2\psi_y}{dy^2} + k_y^2\psi_y = 0$$

$$\Rightarrow \quad \psi_y(y) = Ce^{-\gamma_4 y}\ ,\ y > c/2$$
$$\psi_y(y) = A\cos(k_y y)\ ,\ |y| < c/2$$
$$\psi_y(y) = Be^{\gamma_4 y}\ ,\ y < -c/2$$

where: $\gamma_4^2 = k^2(n_3^2 - n_4^2) - k_y^2$

From boundary conditions (continuity of ψ and $\frac{d\psi}{dy}$ at $y = \pm c/2$), the following characteristic equation is derived:

$$\sqrt{k^2(n_3^2 - n_4^2) - k_y^2} = k_y \tan\left(k_y \frac{c}{2}\right)$$

This equation is then solved for k_y.

In addition, the boundary conditions provide a determination of the constants B and C in terms of the constant A:

$$B = C = A[\cos(k_y \tfrac{c}{2}) e^{(\gamma_4 \frac{c}{2})}]$$

An effective index is defined as:

$$n_{eff} = \sqrt{n_3^2 - (\tfrac{k_y}{k})^2}$$

This value will replace the index of the waveguide core region (n_3) for the x-direction calculations:

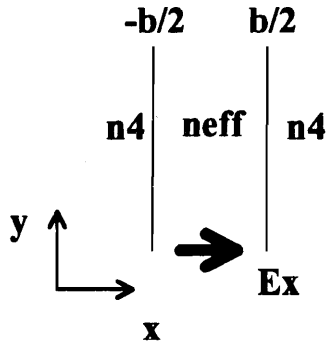

The electric field is now perpendicular to the refractive index boundaries, indicative of a TM-type solution. Again, since the fundamental mode is of interest, the EVEN TM_o solution is desired:

From the wave equation:

$$\frac{d^2\psi_x}{dx^2} + k_x^2\psi_x = 0$$

$$\Rightarrow \quad \psi_x(x) = Fe^{-\bar{\gamma}_4 x}\ ,\ x > b/2$$
$$\psi_x(x) = D\cos(k_x x)\ ,\ |x| < b/2$$
$$\psi_x(x) = Ee^{\bar{\gamma}_4 x}\ ,\ x < -b/2$$

where: $\bar{\gamma}_4^2 = k^2(n_{eff}^2 - n_4^2) - k_x^2$

Again, from the boundary conditions (continuity of ψ and $\frac{d\psi}{dx}$ at $x = \pm b/2$), the following characteristic equation is derived:

$$\sqrt{k^2(n_{eff}^2 - n_4^2) - k_x^2} = k_x \tan(k_x \tfrac{b}{2})$$

This equation is then solved for k_x.

In addition, the boundary conditions again provide a determination of the constants E and F in terms of the constant D:

$$E = F = D[\cos(k_x \tfrac{b}{2})e^{(\bar{\gamma}_4 \frac{b}{2})}]$$

Note that the waveguide has been divided into nine regions, as shown below.

The corner (unnumbered) regions will be neglected, as the fields in those regions experience two exponential decays (one in the x-direction and one in the y-direction). The field expressions for the other five regions are also shown below.

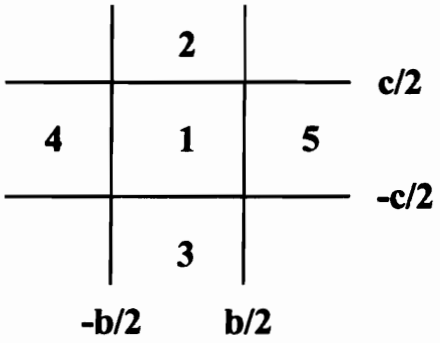

$$\psi(x,y) = e_{x1} = \begin{cases} A'\cos(k_x x)\cos(k_y y), & \text{in region 1} \\ A'\cos(k_x x)B'e^{-\gamma_4 y}, & \text{in region 2} \\ A'\cos(k_x x)B'e^{\gamma_4 y}, & \text{in region 3} \\ A'C'e^{\bar{\gamma}_4 x}\cos(k_y y), & \text{in region 4} \\ A'C'e^{-\bar{\gamma}_4 x}\cos(k_y y), & \text{in region 5} \end{cases}$$

where: $A' = AD$

$B' = \cos(k_y \frac{c}{2})e^{\gamma_4 \frac{c}{2}}$

$C' = \cos(k_x \frac{b}{2})e^{\bar{\gamma}_4 \frac{b}{2}}$

The single mode illumination from the fiber will be represented as a Gaussian beam with the following field expression:

$$\vec{E}_x = Ae^{\left(\frac{-r^2}{2w^2}\right)}\hat{a}_x$$

where: w = mode field radius (spot size)

$\frac{w}{a} \cong 0.65 + 1.619V^{-3/2} + 2.879V^{-6}$, for $1.2 < V < 2.4$ [27]

$V = \frac{2\pi}{\lambda}a\sqrt{n_1^2 - n_2^2}$

Therefore the power incident on the waveguide from the fiber is expressed as:

$$P_i = \frac{1}{2}(120\pi)n\int_{A\infty} \left|\vec{E}_x\right|^2 dA$$

$$P_i = \frac{1}{2}(120\pi)n(\pi A^2 w^2)$$

The field generated inside the waveguide is dependent on the characteristics of the illuminating field, and is expressed in terms of a modal amplitude:[58]

$$\text{modal amplitude:} \qquad a_1 = \frac{\int_{A\infty} E_x e_{x1} dA}{\int_{A\infty} |e_{x1}|^2 dA}$$

Thus, $\vec{e}_1 = a_1 e_{x1} \hat{a}_x$,

and the power generated within the waveguide is expressed as:

$$P_1 = \frac{1}{2}(120\pi)n\int_{A\infty} |\vec{e}_1|^2 dA$$

Therefore, the coupling efficiency of this configuration is given by the following equation:

$$\eta = \text{coupling efficiency} = \frac{1}{\pi A^2 w^2}\left\{\frac{\left[\int_{A\infty} E_x e_{x1} dA\right]^2}{\left[\int_{A\infty} |e_{x1}|^2 dA\right]}\right\}$$

Note that $A\infty$ is comprised of the five regions mentioned earlier.

Let: $\eta = \frac{1}{\pi A^2 w^2}\left\{\frac{N^2}{D}\right\}$, where:

$$N = AA'\int_{-b/2}^{b/2} e^{\left(\frac{-x^2}{2w^2}\right)}\cos(k_x x)dx\left[\int_{-c/2}^{c/2} e^{\left(\frac{-y^2}{2w^2}\right)}\cos(k_y y)dy + \int_{c/2}^{\infty} B'e^{\left(\frac{-y^2}{2w^2}\right)}e^{-\gamma_4 y}dy + \int_{-\infty}^{-c/2} B'e^{\left(\frac{-y^2}{2w^2}\right)}e^{\gamma_4 y}dy\right]$$

$$+ AA'\int_{-c/2}^{c/2} C'e^{\left(\frac{-y^2}{2w^2}\right)}\cos(k_y y)dy\left[\int_{-\infty}^{-b/2} e^{\left(\frac{-x^2}{2w^2}\right)}e^{\bar{\gamma}_4 x}dx + \int_{b/2}^{\infty} e^{\left(\frac{-x^2}{2w^2}\right)}e^{-\bar{\gamma}_4 x}dx\right]$$

$$D = (A')^2\int_{-b/2}^{b/2} \cos^2(k_x x)dx\left[\int_{-c/2}^{c/2} \cos^2(k_y y)dy + \int_{c/2}^{\infty} (B')^2 e^{-2\gamma_4 y}dy + \int_{-\infty}^{-c/2} (B')^2 e^{2\gamma_4 y}dy\right]$$

$$+ (A')^2\int_{-c/2}^{c/2} (C')^2\cos^2(k_y y)dy\left[\int_{-\infty}^{-b/2} e^{2\gamma_4 x}dx + \int_{b/2}^{\infty} e^{-2\gamma_4 x}dx\right]$$

These equations are evaluated using Mathcad® software utilities. Numerical values for both the fiber and the waveguide parameters are selected and used in the calculations. The following pages demonstrate the evaluation procedure, and provide results for a number of situations. Note that the fiber parameters remain constant throughout. First, a wavelength (1550 nm) and a typical value of the y-dimension of the waveguide (c = 25 um) are selected. The coupling efficiency of the configuration is then calculated for various values of the x-dimension of the waveguide (b). As shown in Figure A.2, there exists an "optimum" value of b (b ~ 20 um) for maximum coupling efficiency. Next, the wavelength and this optimum value of b are fixed, and the coupling efficiency is calculated for various values of c. The optimum value of c (c ~ 20 um) is demonstrated in Figure A.3. This combination of b = c = 20 um provides a maximum coupling efficiency of 97.6% at a wavelength of 1550 nm. This process is repeated at a new fixed wavelength value (1300 nm). Again, optimum values of c and b are determined (Figures A.4 and A.5). At this wavelength, values of b = c = 17 um provide a maximum coupling efficiency of 97.7%. Finally, Figure A.6 demonstrates the spectral characteristics of these two waveguide structures (b = c = 20 um and b = c = 17 um).

Note that for multimode propagation, the coupling efficiency may be expressed as the following ratio:

$$\eta = \frac{A_{comm}}{A_f} = \frac{A_{comm}}{\pi a^2}$$

where: A_{comm} refers to the area common to both the fiber and the waveguide end faces

fiber parameters:

$a := 4 \cdot 10^{-6}$

$n1 := 1.5$

$n2 := 1.495$

$\lambda := 1550 \cdot 10^{-9}$

$v := \frac{2 \cdot \pi}{\lambda} \cdot a \cdot \sqrt{n1^2 - n2^2}$

$v = 1.984$

$w := a \cdot \left[0.65 + \left(1.619 \cdot v^{-1.5}\right) + \left(2.879 \cdot v^{-6}\right)\right]$

$k := \frac{2 \cdot \pi}{\lambda}$

waveguide parameters:

$n3 := 1.5$

$n4 := 1.4$

$b := 20 \cdot 10^{-6}$

$c := 20 \cdot 10^{-6}$

characteristic equations:

$left1(ky) := \sqrt{k^2 \cdot \left(n3^2 - n4^2\right) - ky^2}$

$right1(ky) := ky \cdot \tan\left(\frac{ky \cdot c}{2}\right)$

$ky := 150193 .. 150194$

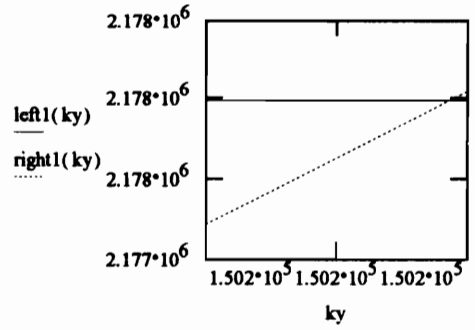

$ky := 150194$

$neff := \sqrt{n3^2 - \left(\frac{ky}{k}\right)^2}$

$$left2(kx) := \sqrt{k^2 \cdot \left(neff^2 - n4^2\right) - kx^2}$$

$$right2(kx) := kx \cdot \tan\left(\frac{kx \cdot b}{2}\right)$$

$kx := 150178 .. 150179$

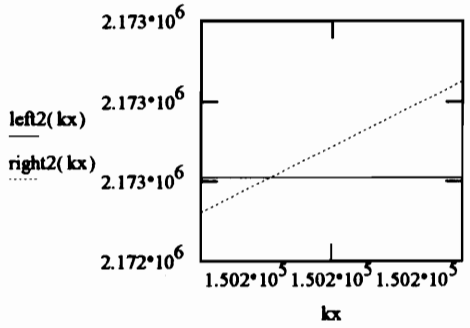

$kx := 150178$

$$Bp := \cos\left(\frac{ky \cdot c}{2}\right) \cdot e^{(left1(ky)) \cdot \frac{c}{2}}$$

$$Cp := \cos\left(\frac{kx \cdot b}{2}\right) \cdot e^{(left2(kx)) \cdot \frac{b}{2}}$$

$$I1 := \int_{-\frac{b}{2}}^{\frac{b}{2}} e^{\left(-\frac{x^2}{2 \cdot w^2}\right)} \cdot \cos(kx \cdot x)\, dx$$

$$I2 := \int_{-\frac{c}{2}}^{\frac{c}{2}} e^{\left(-\frac{y^2}{2 \cdot w^2}\right)} \cdot \cos(ky \cdot y)\, dy$$

$$I3 := Bp \cdot \left[0.5 \cdot \sqrt{\pi} \cdot e^{\left[0.5 \cdot \left[(left1(ky))^2\right] \cdot w^2\right]} \cdot \sqrt{2} \cdot w \cdot erf\left[\left(0.5 \cdot \frac{\sqrt{2}}{w} \cdot \frac{c}{2} \right) - \left[0.5 \cdot (-left1(ky)) \cdot \sqrt{2} \cdot w \right] \right] \right]$$

$$I3p := \left[0.5 \cdot \sqrt{\pi} \cdot e^{\left[0.5 \cdot \left(left1(ky)^2\right) \cdot w^2\right]} \cdot \sqrt{2} \cdot w \right] \cdot Bp$$

$$I3p - I3 = 0$$

$$I4 := Bp \cdot \left[0.5 \cdot \sqrt{\pi} \cdot e^{\left[0.5 \cdot \left(left1(ky)^2\right) \cdot w^2\right]} \cdot \sqrt{2} \cdot w \cdot erf\left[\left[0.5 \cdot \frac{\sqrt{2}}{w} \cdot \left(-\frac{c}{2} \right) \right] - \left[0.5 \cdot (left1(ky)) \cdot \sqrt{2} \cdot w \right] \right] \right]$$

$$I4p := \left[0.5 \cdot \sqrt{\pi} \cdot e^{\left[0.5 \cdot \left(left1(ky)^2\right) \cdot w^2\right]} \cdot \sqrt{2} \cdot w \right] \cdot Bp$$

$$I4 + I4p = 0$$

$$I5 := \left[0.5 \cdot \sqrt{\pi} \cdot e^{\left[0.5 \cdot \left(left2(kx)^2\right) \cdot w^2\right]} \cdot \sqrt{2} \cdot w \cdot erf\left[\left[0.5 \cdot \frac{\sqrt{2}}{w} \cdot \left(-\frac{b}{2}\right)\right] - \left[0.5 \cdot (left2(kx)) \cdot \sqrt{2} \cdot w\right]\right]\right]$$

$$I5p := \left[0.5 \cdot \sqrt{\pi} \cdot e^{\left[0.5 \cdot \left(left2(kx)^2\right) \cdot w^2\right]} \cdot \sqrt{2} \cdot w\right]$$

$$I5 + I5p = 0$$

$$I6 := \left[0.5 \cdot \sqrt{\pi} \cdot e^{\left[0.5 \cdot \left(left2(kx)^2\right) \cdot w^2\right]} \cdot \sqrt{2} \cdot w \cdot erf\left[\left[0.5 \cdot \frac{\sqrt{2}}{w} \cdot \left(\frac{b}{2}\right)\right] - \left[0.5 \cdot (-left2(kx)) \cdot \sqrt{2} \cdot w\right]\right]\right]$$

$$I6p := \left[0.5 \cdot \sqrt{\pi} \cdot e^{\left[0.5 \cdot \left(left2(kx)^2\right) \cdot w^2\right]} \cdot \sqrt{2} \cdot w\right]$$

$$I6p - I6 = 0$$

$$J1 := \left[\frac{b}{2} + \left(\frac{1}{2 \cdot kx} \cdot \sin(kx \cdot b)\right)\right]$$

$$J2 := \left[\frac{c}{2} + \left(\frac{1}{2 \cdot ky} \cdot \sin(ky \cdot c)\right)\right]$$

$$J3 := \left(\frac{Bp^2 \cdot e^{-left1(ky) \cdot c}}{left1(ky)}\right)$$

$$J4 := \left(\frac{e^{-left2(kx) \cdot b}}{left2(kx)}\right)$$

$I1 = 9.672 \cdot 10^{-6}$

$I2 = 9.671 \cdot 10^{-6}$

$J1 = 1.046 \cdot 10^{-5}$ $J3 = 2.174 \cdot 10^{-9}$

$J2 = 1.046 \cdot 10^{-5}$ $J4 = 0$

$NUM := I1 \cdot I2$

$NUM = 9.354 \cdot 10^{-11}$

$DENOM := J1 \cdot (J2 + J3) + \left(Cp^2 \cdot J2 \cdot J4\right)$

$DENOM = 1.094 \cdot 10^{-10}$

$$COUP := \frac{1}{\pi \cdot w^2} \cdot \left(\frac{NUM^2}{DENOM}\right)$$

$COUP = 0.976$

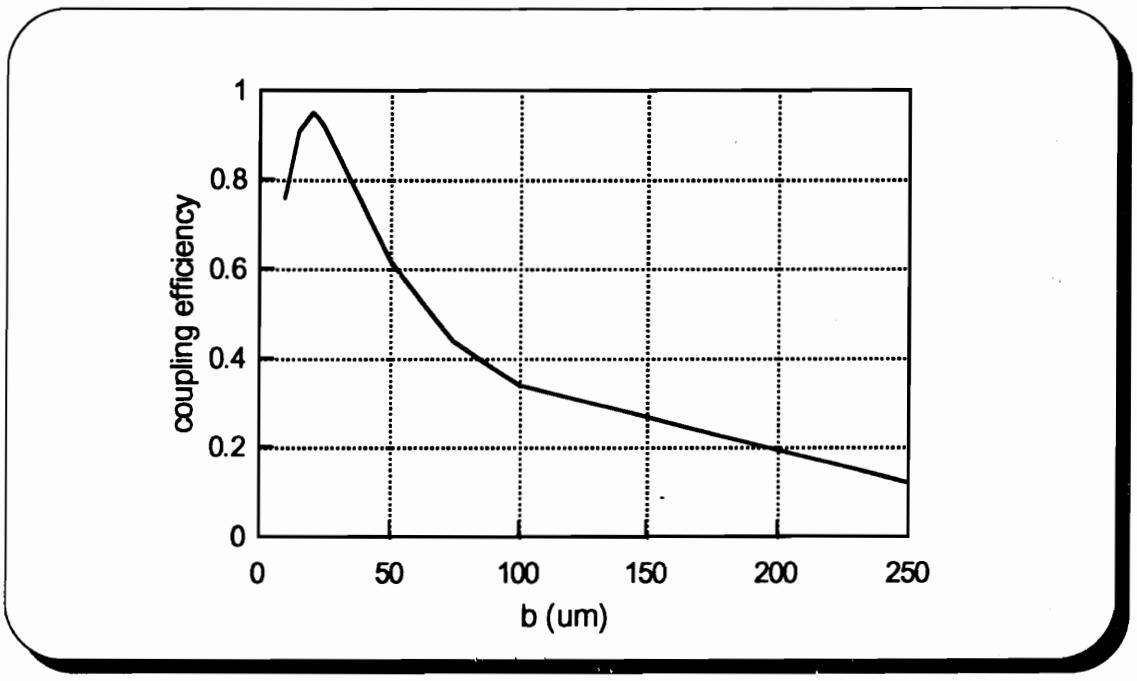

Figure A.2 - Coupling efficiency vs waveguide dimension (b) (1550 nm)

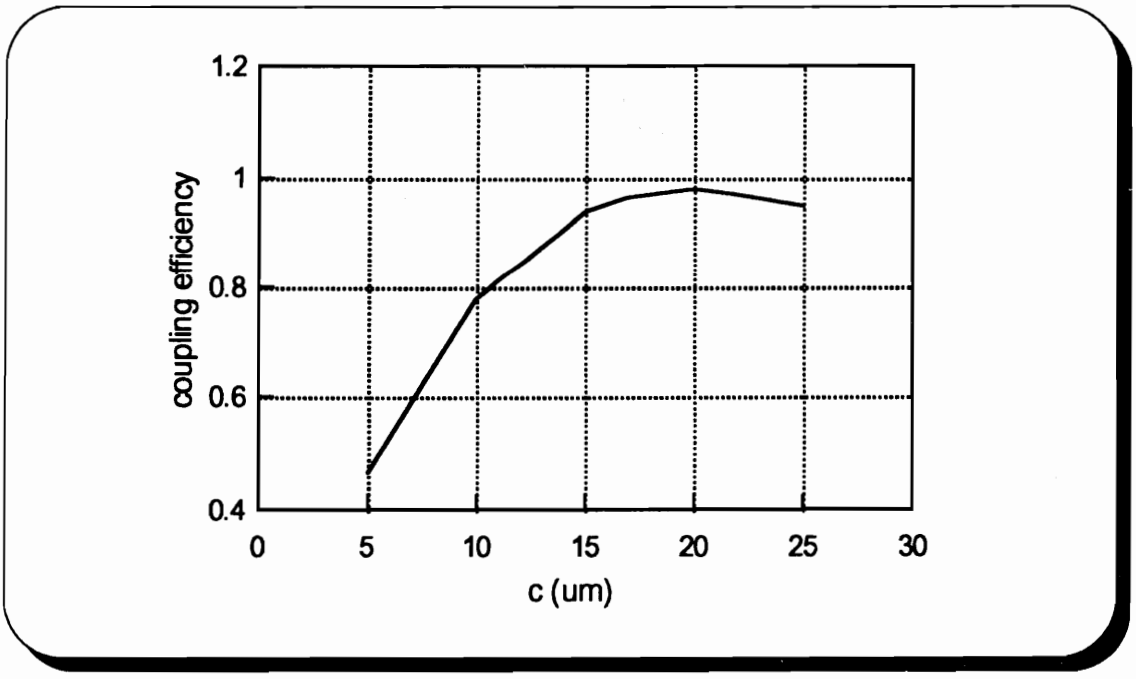

Figure A.3 - Coupling efficiency vs waveguide dimension (c) (1550 nm)

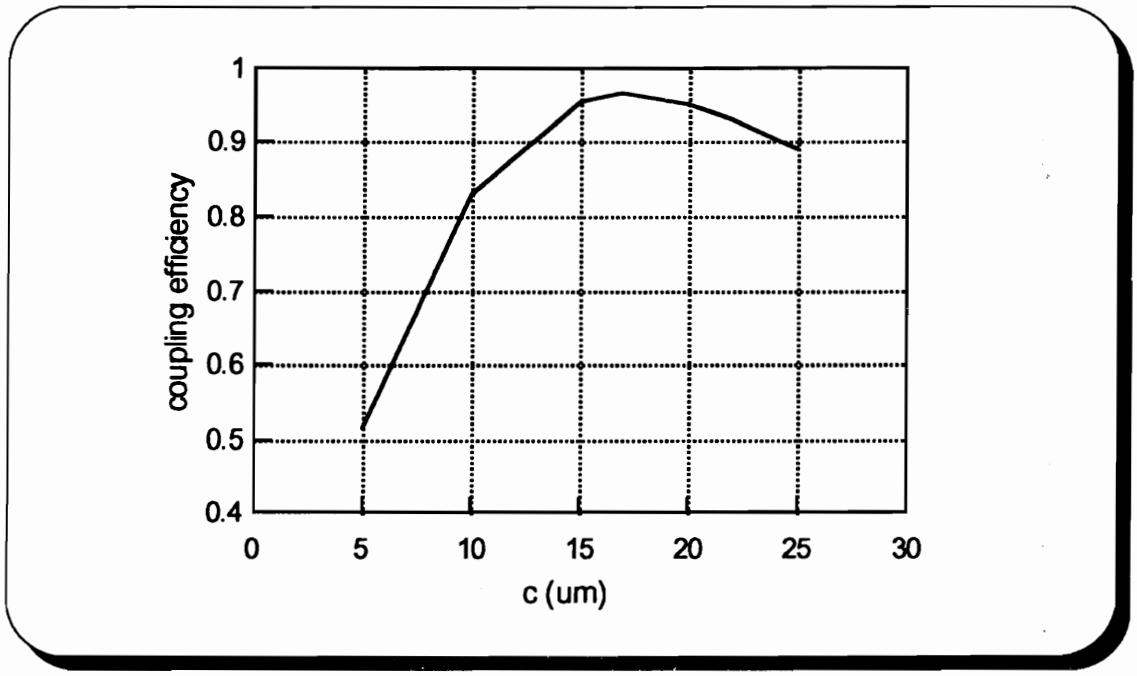

Figure A.4 - Coupling efficiency vs waveguide dimension (c) (1300 nm)

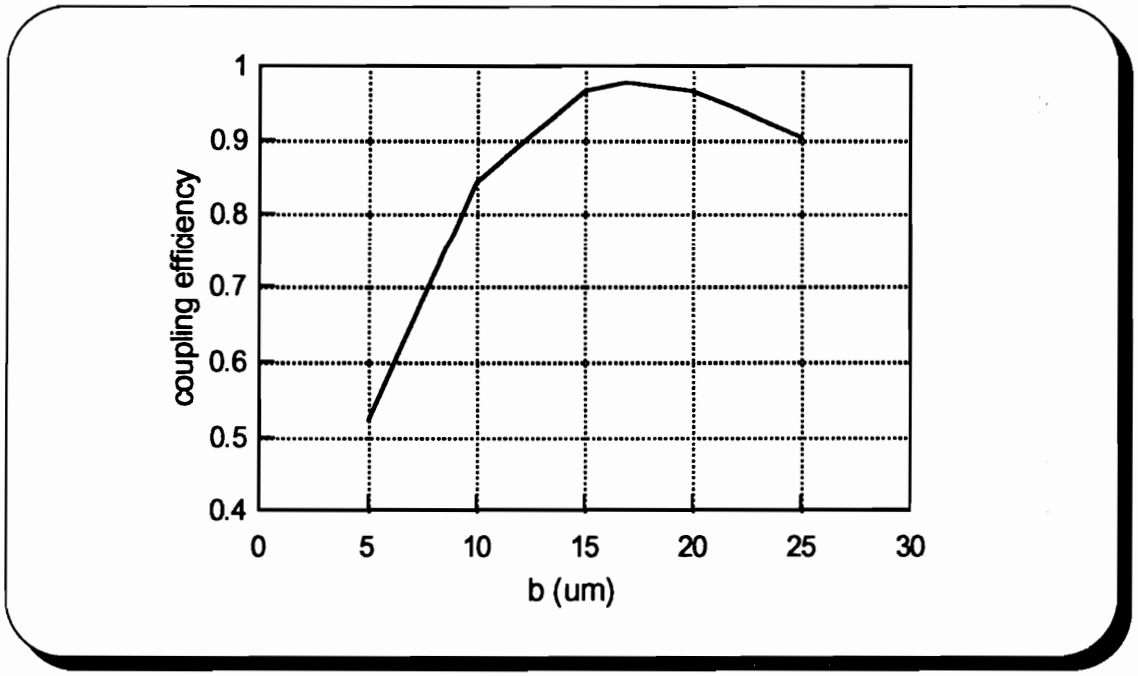

Figure A.5 - Coupling efficiency vs waveguide dimension (b) (1300 nm)

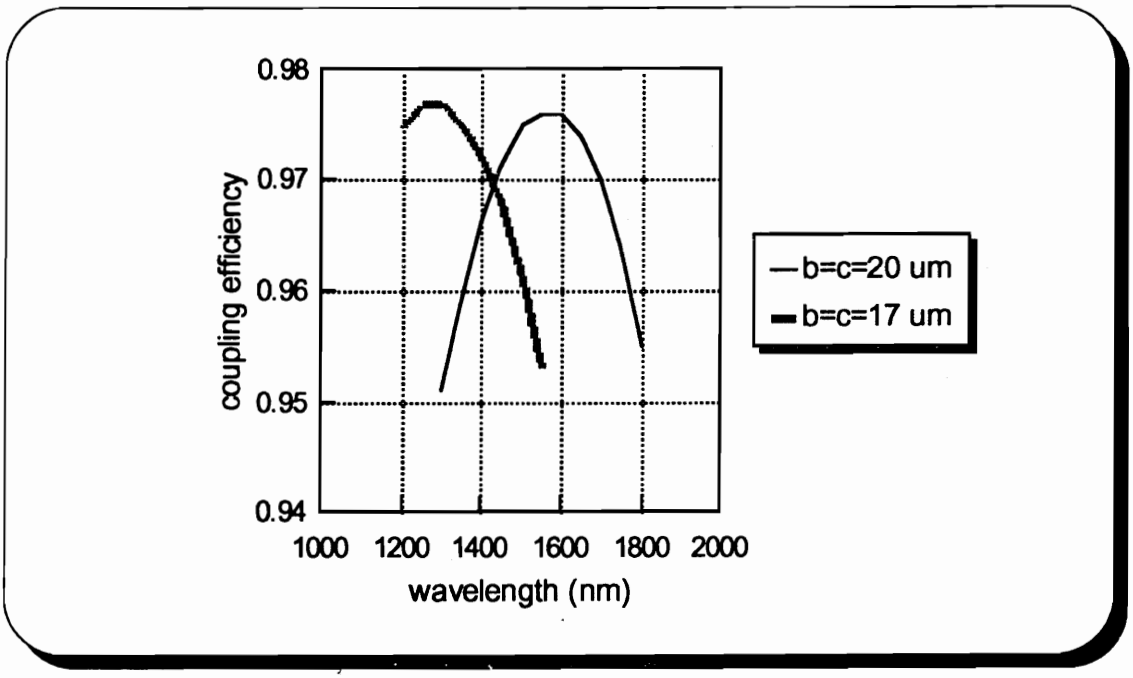

Figure A.6 - Coupling efficiency vs wavelength

References

[1] Keiser, G., *Optical Fiber Communications*, 2nd. ed., 1991.

[2] Brian, M., and Lee, T-P, "Optical Receivers for Lightwave Communication Systems," *Journal of Lightwave Technology*, Vol. LT-3, No. 6, December 1985, pp. 1281-1300.

[3] Shen, D.S., Conde, J.P., Chu, V., Aljishi, S., Liu, J.Z., and Wagner, S., "Amorphous Silicon-germanium Thin-film Photodetector Array," *IEEE Electron Device Letters*, Vol. 13, No. 1, January 1992, pp. 5-7.

[4] Ghioni, M., Lacaita, A., Ripamonti, G., and Cova, S., "All-silicon Avalanche Photodiode Sensitive at 1.3 um with Picosecond Time Resolution," *IEEE Journal of Quantum Electronics*, Vol. 28, No. 12, December 1992, pp. 2678-2681.

[5] Kato, K., Hata, S., Kawano, K., Yoshida, J., and Kozen, A., "A High-efficiency 50 GHz InGaAs Multimode Waveguide Photodetector," *IEEE Journal of Quantum Electronics*, Vol. 28, No. 12, December 1992, pp. 2728-2735.

[6] Milano, R.A., Dapkus, D., and Stillman, G.E., "An Analysis of the Performance of Heterojunction Phototransistors for Fiber Optic Communications," *IEEE Transactions on Electron Devices*, Vol. ED-29, No. 2, February 1982, pp. 266-274.

[7] Carruthers, T.F., Duling III, I.N., Aina, O., Mattingly, M., and Serio, M., "Responses of InP/$Ga_{0.47}In_{0.53}As$/InP Heterojunction Bipolar Transistors to 1530 and 620 nm Ultrafast Optical Pulses," *Applied Physics Letters*, Vol. 59, No. 3, 15 July 1991, pp. 327-329.

[8] Chandrasekhar, S., Lunardi, L.M., Gnauck, A.H., Hamm, R.A., and Qua, G.J., "High-speed Monolithic p-i-n/HBT and HPT/HBT Photoreceivers Implemented with Simple Phototransistor Structure," *IEEE Photonics Technology Letters*, Vol. 5, No. 11, November 1993, pp. 1326-1318.

[9] John, E., and Das, M.B., "Design and Performance Analysis of InP-based High-speed and High-sensitivity Optoelectronic Integrated Receivers," *IEEE Transactions on Electron Devices*, Vol. 41, No. 2, February 1994, pp. 162-171.

[10] Lai, Q., Gu, J.S., Smit, M.K., Schmid, J., and Melchior, H., "Simple Technologies for Fabrication of Low Loss Silica Waveguides," *Electronics Letters*, Vol. 28, No. 11, 21 May 1992, pp. 1000-1001.

[11] Narenda, R., and McMullin, J.N., "Single-mode Phosphorus-doped Silica Waveguides in Silicon V-grooves," *IEEE Photonics Technology Letters*, Vol. 5, No. 1, January 1993, pp. 43-46.

[12] Yin, Z-Y, Jessop, P.E., and Garside, B.K., "Photoinduced Grating Filters in GeO_2 Thin-film Waveguides," *Applied Optics*, Vol. 22, No. 24, 15 December 1983, pp. 4088-4092.

[13] Yin, Z-Y, and Garside, B.K., "Low-loss GeO_2 Optical Waveguide Fabrication using Low Deposition Rate RF Sputtering," *Applied Optics*, Vol. 21, No. 23, 1 December 1982, pp. 4324-4328.

[14] Roman, J.E., and Winick, K.A., "Photowritten Gratings in Ion-exchanged Glass Waveguides," *Optics Letters*, Vol. 18, No. 10, 15 May 1993, pp. 808-810.

[15] Sullivan, C.T., Booth, Bruce L., and Husain, A., "Polymeric Waveguides," *IEEE Circuits and Devices*, Vol. 8, No. 1, January 1992, pp. 27-31.

[16] Keil, N., Strebel, B., Yao, H., Zawadzki, C., and Hwang, W., "Optical Polymer Waveguide Devices and their Applications to Integrated Optics and Optical Signal Processing," *SPIE*, Vol. 1774, 1992, pp. 130-141.

[17] Beeson, K.W., McFarland, M.J., Pender, W.A., Shan, J., Wu, C., and Yardly, J.T., "Laser-written Polymeric Optical Waveguides for Integrated Optical Device Applications," *SPIE*, Vol. 1794, 1992, pp. 397-404.

[18] Becker, R.A., "Comparison of Guided-wave Interferometric Modulators Fabricated on $LiNbO_3$ via Ti Indiffusion and Proton Exchange," *Applied Physics Letters*, Vol. 43, No. 2, 15 July 1983, pp. 131-133.

[19] Kato, K., Hata, S., Kozen, A., Oku, S., Matsumoto, S., and Yoshida, J., "22 GHz Photodiode Monolithically Integrated with Optical Waveguide on Semi-insulating InP using Novel Butt-joint Structure," *Electronics Letters*, Vol. 28, No. 12, 4 June 1992, pp. 1140-1142.

[20] South, R.B., and McDonough, H., "Thick Film Optical Waveguides," *5th European Hybrid Microelectronics Conference 1985, Stresa, Italy*, pp. 433-438.

[21] Keresztes-Nagy, Z., and Harsanyi, G., "Shaping and Coupling of Optical Thick Film Waveguides," *1993 Japan Int'l Electronics Manufacturing Technology Symposium*, pp. 271-274.

[22] Shimada, Y., Shin'e, T., Uda, Y., Nagaoka, R., and Takamizawa, H., "Application of Multilayer Ceramic Components for Fiber-optic Transmitter/Receiver," *ISHM 1989 Proceedings*, pp. 287-294.

[23] Tanaka, H., Nagaoka, R., Makabe, T., Kawatani, A., Kobayashi, Y., Shuke, K., Suzuki, Y., and Suzuki, F., "Multichip Module for 156Mb/s Optical Interface," *International Conference and Exhibition on Multichip Modules Proceedings*, TA1-3, 1993, pp. 247-251.

[24] Pavlath, G.A., "Method for Rugged Attachment of Fibers to Integrated Optics Chips and Product Thereof," United States Patent #5146522, September 8 1992.

[25] Kasaya, K., Mitomi, O., Naganuma, M., Kondo, Y., and Noguchi, Y., "A Simple Laterally Tapered Waveguide for Low-loss Coupling to Single-mode Fibers," *IEEE Photonics Technology Letters*, Vol. 5, No. 3, March 1993, pp. 345-347.

[26] Denshin, N., Kosha, D., and Kawachi, M., "Connecting Method of Optical Fiber and Optical Waveguide," Japanese Patent #59-189308, October 26, 1984.

[27] Agrawal, G.P., *Fiber Optic Communication Systems*, 1992.

[28] Sze, S.M., *Physics of Semiconductor Devices*, 2nd. ed., 1981.

[29] Beneking, H., "Gain and Bandwidth of Fast Near-infrared Photodetectors: A Comparison of Diodes, Phototransistors, and Photoconductive Devices," *IEEE Transactions on Electron Devices*, Vol. ED-29, No. 9, September 1982, pp. 1420-1431.

[30] Smith, R.G., Brackett, C.A., and Reinbold, H.W., "Optical Detector Package," *The Bell System Technical Journal*, Vol. 57, No. 6, July-August 1978, pp. 1809-1821.

[31] Malvino, A.P., *Electronic Principles*, 3rd. ed., 1984, pp. 138-139.

[32] Marcuse, D., *Theory of Dielectric Optical Waveguides*, 2nd. ed., 1991.

[33] Federico, T., ed., *Fiber Optic Communications Handbook*, 2nd. ed., Technical Staff of CSELT, 1990.

[34] Duguay, M.A., Valdmanis, J.A., and Miller, D.A.B., "Electrooptics," in *McGraw-Hill Encyclopedia of Science & Technology*, Parker, S.P., ed., 7th. ed., Vol. 6, 1992, pp. 256-257.

[35] Bloor, D., Brook, R.J., Flemings, M.C., Mahajan, S., and Cahn, R.W., eds., *The Encyclopedia of Advanced Materials*, Vol. 3, 1994, pp. 1993-2000.

[36] Kanzig, W., "Ferroelectrics," in *McGraw-Hill Encyclopedia of Science & Technology*, Parker, S.P., ed., 7th. ed., Vol. 7, 1992, pp. 58-62.

[37] Zuk, W., "Photoelasticity," and Granicher, H., "Piezoelectricity," in *McGraw-Hill Encyclopedia of Science & Technology*, Parker, S.P., ed., 7th. ed., Vol. 13, 1992, pp. 403-405, 533-538.

[38] Tsai, C.S., "Acoustooptics," in *McGraw-Hill Encyclopedia of Science & Technology*, Parker, S.P., ed., 7th. ed., Vol. 1, 1992, pp. 89-91.

[39] Granicher, H., and Hadni, A., "Pyroelectricity," in *McGraw-Hill Encyclopedia of Science & Technology*, Parker, S.P., ed., 7th. ed., Vol. 14, 1992, pp. 541-543.

[40] Nishihara, H., Haruna, M., and Suhara, T., *Optical Integrated Circuits*, 1989.

[41] Gleim, P.S., "Germanium," and McMahon, J.F., and Rockett, F.H., "Glass," in *McGraw-Hill Encyclopedia of Science & Technology*, Parker, S.P., ed., 7th. ed., Vol. 8, 1992, pp. 77-85, 123-127.

[42] Dianov, E.M., "Prospects for the Use of the 1-1.6 u Wavelength Range in Fiber-optic Communications (Review)," *Soviet Journal of Quantum Electronics*, Vol. 10, No. 3, March 1980, pp. 259-265.

[43] Devyatykh, G.G., Dianov, E.M., Karpychev, N.S., Mazavin, S.M., Mashinskii, V.M., Neustruev, V.B., Nikolaichik, A.V., Prokhorov, A.M., Ritus, A.I., Sokolov, N.I., and Yushin, A.S., "Material Dispersion and Rayleigh Scattering in Glassy Germanium Dioxide, a Substance with Promising Applications in Low-loss Optical Fiber Waveguides," *Soviet Journal of Quantum Electronics*, Vol. 10, No. 7, July 1980, pp. 900-902.

[44] Vega, F., Afonso, C.N., Solis, J., Serna, R., and Ortiz, C., "UV-laser-induced Oxidation Kinetics of c-Ge: Transient Reflectivity Study," *Applied Surface Science*, Vol. 54, 1992, pp. 341-344.

[45] Boishin, G., Tyuliev, G., and Surnev, L., "XPS Study of Oxygen Interaction with a Ge-covered Si (100) Surface," *Surface Science*, Vol. 303, 1994, pp. 333-340.

[46] Prabhakaran, K., Nishioka, T., Kobayashi, Y., and Ogino, T., "In Situ Oxidation of Ultrathin Layers of Ge on Si (001): Evidence for Bonding Partner Exchange," *Applied Surface Science*, Vol. 75, 1994, pp. 341-347.

[47] Jain, S.C., and Balk, P., "Preparation and Properties of the GeSi-oxide System," *Thin Solid Films*, Vol. 223, 1993, pp. 348-357.

[48] Zhang, J.P., Hemment, P.L.F., Kubiak, R.A., and Parker, E.H.C., "Formation of Germanium Dioxide During Wet Oxidation of $Si_{0.5}Ge_{0.5}$ Alloy," *Materials Research Society Symposium Proceedings*, Vol. 326, 1994, pp. 73-78.

[49] Seeley, J., "Optical Thin Films," in *Concise Encyclopedia of Semiconducting Materials & Related Technologies*, Mahajan, S., Kimerling, L.C., Cahn, R.W., and Bever, M.B., eds., 1992, pp. 341-342.

[50] De Sande, J.C.G., Escudero, J.L., and Bernabeu, E., "Ellipsometric Study of the Oxidation of Electron-beam-evaporated a-Ge Films," *Thin Solid Films*, Vol. 203, 1991, 327-334.

[51] Macleod, H.A., "Optical Thin Films: Production and Use," in *Concise Encyclopedia of Semiconducting Materials & Related Technologies*, Mahajan, S., Kimerling, L.C., Cahn, R.W., and Bever, M.B., eds., 1992, pp. 342-346.

[52] Longhurst, R.S., *Geometrical and Physical Optics*, 1957, p. 416.

[53] Demkina, L.I., "Coordination State and the Properties of Germanium Oxide in a Glass," *The Soviet Journal of Glass Physics and Chemistry*, Vol. 16, No. 3, May-June 1990, pp. 173-181.

[54] Worrell, C.A., and Skarda, V., "CO_2 Laser Waveguides from Germania-based Glasses," *Journal of Physics D: Applied Physics*, Vol. 22, 1989, pp. 535-541.

[55] Musikant, S., "Glass," in *Encyclopedia of Physical Science and Technology*, Meyers, R.A., ed., 2nd. ed., Vol. 7, 1992, pp. 411-440.

[56] Collins, R.W., and Vedam, K., "Ellipsometers," in *Encyclopedia of Applied Physics*, Trigg, G.L., ed., Vol. 6, 1993, pp. 191-205.

[57] Parker, S.P., ed., *Spectroscopy Source Book*, 1988, p. 248.

[58] Snyder, A.W., and Love, J.D., *Optical Waveguide Theory*, 1983.

Vita

J. Shawn Addington received a Bachelor's Degree in Electrical Engineering from the Bradley Department of Electrical Engineering at Virginia Tech in May 1990. In the summer of 1990, he began working toward a Master's Degree in Electrical Engineering at the same University. As a Master's student, he worked as both a Graduate Research Assistant, as well as a Graduate Teaching Assistant. As a DuPont Fellow, he also had the opportunity to work one summer (1991) at the DuPont Electronics Facility in Research Triangle Park, North Carolina, performing wideband electrical characterizations of dielectric materials. In March 1992, he received the Harry Lynde Bradley Fellowship from the Bradley Department of Electrical Engineering at Virginia Tech. In May 1992, he completed his Master's thesis, entitled "Wideband Electrical Characterization of Multilayer Low-Loss Dielectric Materials." In the summer of 1992, he began working toward his Doctoral Degree in Electrical Engineering at Virginia Tech in the area of Integrated Optoelectronics. During the Summer Sessions of 1993 and 1994, he served as an Instructor for the Bradley Department of Electrical Engineering, teaching sophomore level electronics classes. In September 1995, he completed his Doctoral dissertation, entitled "Integrated Optoelectronics Applications in Fiber Optic Receiver Packaging." Since September 1995, he has served as a Visiting Assistant Professor within the Department of Electrical and Computer Engineering at Old Dominion University.